Variability of Large-scale Ocean Circulation and Meridional Heat Transport in the Atlantic Ocean

Jinting Zhang

A dissertation

submitted in partial fulfillment of the

requirements for the degree of

Doctor of Philosophy

University of Washington

2015

Reading Committee:

LuAnne Thompson, Chair

Kathryn A. Kelly, Chair

Susan L. Hautala

Program Authorized to Offer Degree:

Oceanography

University of Washington

Abstract

Variability of Large-scale Ocean Circulation and Meridional Heat Transport in the Atlantic Ocean

Jinting Zhang

Chair of the Supervisory Committee:
LuAnne Thompson
School of Oceanography
Kathryn A. Kelly
Applied Physics Laboratory

The research described in the dissertation addresses what controls the variability of ocean circulation and meridional heat transport (MHT) in the Atlantic Ocean on different timescales. Chapter 2 focuses on the contribution of surface heating and wind forcing with/without topography to the seasonal and interannual-to-decadal variations of large-scale sea surface height (SSH) using simplified models. On the seasonal timescale thermosteric height explains most of the SSH variance north of 18°N and first mode linear long Rossby wave explains the SSH between 10°N-15°N and east of Greenland. On interannual-to-decadal timescales, a topographic Sverdrup response explains interannual-to-decadal SSH between 53°N and 63°N east of Greenland, suggesting the important role of topography in the subpolar region. Farther south, the linear Rossby wave model explains SSH variations on interannual-to-decadal timescales between 30°N and 50°N from mid-basin to the eastern boundary. In Chapter 3, perturbation experiments and a 1000-year control simulation in the GFDL coupled model CM2.1 are used to investigate the evolution of the Atlantic meridional overturning circulation (AMOC) and its related upper ocean heat content (UOHC) on the decadal timescale. A slow southward propagation of positive AMOC anomaly in northern high latitudes leads to a convergence (divergence) of the Atlantic

MHT anomaly in the subpolar (Gulf Stream) region, thus warming (cooling) in the subpolar (Gulf Stream) region after several years. The study presented in Chapter 4 examines the coherence structure of the interannual MHT variability in the Atlantic tropics and subtropics using seven simulations in the CMIP5 (Coupled Model Intercomparison Project Phase 5) archive as well as a hindcast simulation in the isopycnal ocean model GOLD (Generalized Ocean Layered Dynamics) from 1971 to 2009. The spatial pattern for the leading mode of the interannual MHT anomaly from all the model simulations has the same sign from 20°S-30°N, with a peak near the equator. Ekman heat transport anomalies between 7°S-20°N and the geostrophic transport beneath the Ekman layer from 13°S-27°N (except the equator) contribute to this MHT leading mode, while the contribution of the deep ocean is negligible. The connection between the hemispheres results from diapycnal transport of the northward geostrophic transport beneath the Ekman layer in the southern tropics; after this water reaches the upper ocean, it then moves northward where Ekman transport takes over. The wind is the main external forcing for the MHT coherence structure. The work in this thesis enhances the understanding of the contributions of heating, winds and topography on sea level changes on seasonal and interannual-to-decadal timescales, as well as the decadal and interannual variability of the AMOC and MHT in the Atlantic Ocean. It could be used to understand the effect of topography on the ocean circulation in the high latitude, improve the decadal prediction of the UOHC in the North Atlantic Ocean, and advance the knowledge of the tropical Atlantic heat transport and ocean-atmosphere coupling system.

TABLE OF CONTENTS

LIST OF FIGURES

LIST OF TABLES

ACKNOWLEDGEMENTS

I would like to express my sincere thanks to my advisors Professor LuAnne Thompson and Professor Kathryn A. Kelly for their encouragement, support and instructive guidance throughout my study time in graduate school. Their professional knowledge, creativity and enthusiasm in research have been of great value for me.

I also want to thank Susan Hautala, Paul Quay, J. Nathan Kutz and Dargan M. W. Frierson for serving in my supervisory committee. I am very grateful for the valuable discussions, suggestions and critique. My research has been greatly influenced by my interaction with my committee members. My special thanks goes to Rong Zhang, my intern supervisor in GFDL, for her valuable guidance during my summer intern, support of problem solving and tremendous contribution to our project (Chapter 2 in this thesis).

I want to gratefully acknowledge all the people who have helped me with my research at the University of Washington. Thank Suzanne Dickinson for data source support; Andrew Shao for discussions on ocean model and being my officemate; David Darr for the technique assistance; Megan Gambs, Miguel Jimenez-Urias, Jacob Wenegrat, Kyle Armour, David Trossman, Jimmy Booth for their generous discussions in our group meetings.

This study was supported by the NASA Ocean Surface Topography Science Team (OSTST) on grants NNX08AR30G and NNX13AH19G with the University of Washington. It was also supported by the NOAA Mentoring Physical Oceanography Women to Increase Retention (MPOWIR) for the summer internship of 2013. We thank Michael Winton, Xiaosong Yang and two other anonymous reviewers for their comments on the manuscript.

Last but not the least, I am grateful to my beloved husband, Wenjun. I would not have completed my work without his unconditional support and encouragement during our PhD years. I am also indebted to my parents for their support, assistance and caring of me all of my life.

DEDICATION

to my beloved husband and parents

Chapter 1. INTRODUCTION

The large-scale ocean circulation plays an important role in the overall heat budget of the planet. It transports and stores heat, and exchanges heat, freshwater and momentum with the atmosphere (*Hartmann,* 1994). For instance, the Atlantic Ocean transports up to 1.3 *PW* heat to the north in the northern subtropics, and then releases a large amount of that heat to the atmosphere in the midlatitudes. Understanding variability of ocean circulation and associated impacts on heat transport, heat storage, and heat exchange with the atmosphere is crucial for the study of the Earth's climate system.

Ocean circulation is driven by the surface wind stress and buoyancy forcing, freshwater and heat flux (*Talley et al.,* 2011). The surface ocean circulation is mainly driven by the wind via Ekman transport and geostrophic flows from the convergences/divergences of Ekman transport via the Sverdrup balance. The Sverdrup balance connects the ocean meridional velocity with the wind stress curl (*Sverdrup,* 1947). For instance, the southward transport in the subtropical North Atlantic results from the negative wind stress curl. The deep ocean circulation generally has weaker velocities when compared to the surface ocean circulation; ultimately, it is driven by mixing that drives the deep ocean flow back to the surface. It is also linked to the differences in seawater density that result from buoyancy forcing, and as such is often called the thermohaline circulation (THC) (*Rahmstorf,* 2002). In addition, the effect of the interaction of the ocean flow with bottom topography should also be taken into account where the ocean has a barotropic structure and in the high latitudes (*Marshall*, 1995; *Wunsch and Roemmich*, 1985).

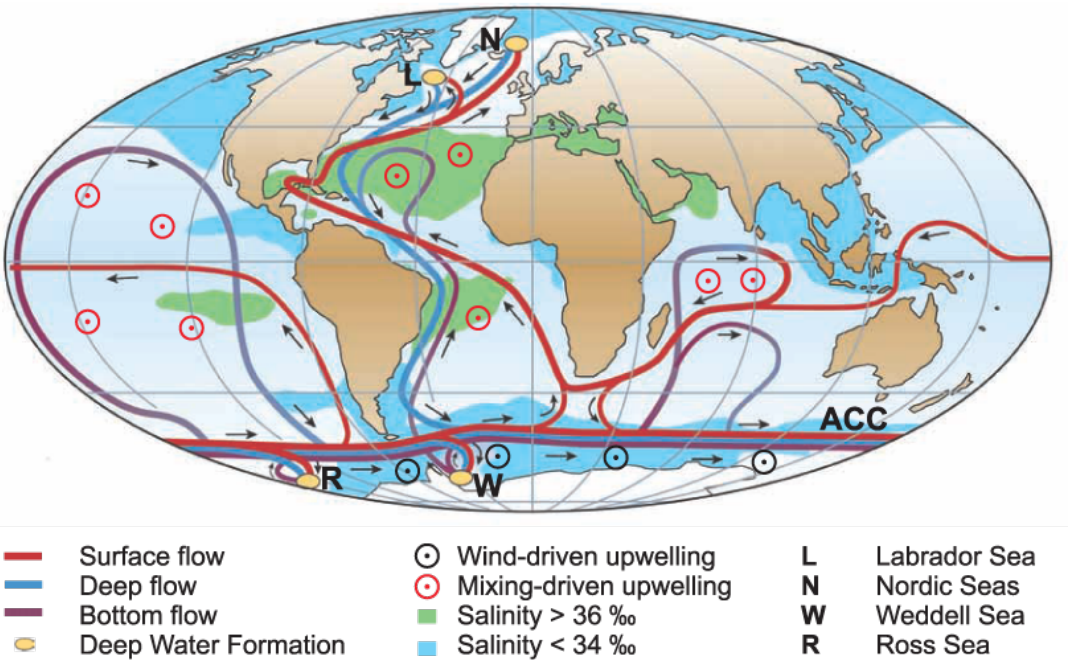

Figure 1.1 Schematic of the ocean circulation (from *Kuhlbrodt et al.,* 2007) associated with the global Meridional Overturning Circulation (MOC), with special focus on the Atlantic section of the flow (AMOC).

The meridional overturning circulation (MOC) defined by a streamfunction from vertically and zonally integrated meridional velocity is composed of both THC and wind-driven circulation. The Atlantic MOC (AMOC) is composed of a northward flow of warm water in upper ocean, sinking water in localized regions in the high latitude North Atlantic, and a southward flow of cold water at depth (Figure 1.1) (e.g. *Broecker* 1991; *Lumpkin and Speer* 2007; *Kuhlbrodt et al.* 2007). AMOC is traditionally defined as the maximum of the meridional transport streamfunction across the whole basin. It represents the total amount of water moving meridionally above that depth with the same amount of water moving below that depth in a reverse direction.

The oceanic meridional heat transport (MHT) that is linked to the AMOC helps to move heat from the tropics to the poles. The global MHT moves heat poleward, symmetric about the

equator, but the MHT in the Atlantic Ocean is consistently northward from the Southern Ocean (SO) to the northern subpolar region owing to the presence of deep circulation (*Trenberth and Solomon,* 1994; *Trenberth and Caron,* 2001). In the tropics and subtropics, the ocean carries a significant fraction of the total heat transport (the sum of the atmospheric and oceanic heat transport). It reaches a maximum near 30°N and then drops rapidly near the latitude of the Gulf Stream (*Trenberth and Caron*, 2001; *Wunsch*, 2005), where the ocean released a large amount of heat to the atmosphere. The atmospheric heat transport dominates further to the north. Oceanic MHT in the Atlantic Ocean is highly associated with the AMOC; *Dong et al.* (2009) and *Msadek et al.* (2013) estimated the MHT corresponding to each Sv volume transport to be $0.05\,PW/Sv$ at 34°S and $0.079\,PW/Sv$ at 26.5°N, respectively.

Previous studies have suggested that changes of AMOC and MHT could impact the extent of Arctic Sea Ice (*Rind and Chandler,* 1991), atmospheric circulation (*Cohen-Solal and Le Treut,* 1997), sea surface temperature (SST) over the North Atlantic and tropical South Atlantic (*Dong and Sutton,* 2002), tropical Atlantic Variability (TAV) (*Wen et al.,* 2011), and the location of the Intertropical Convergence Zone (ITCZ) (*Frierson et al.,* 2013), as well as the Atlantic Multidecadal Oscillation (AMO) (*Knight et al.,* 2005; *Ting et al.,* 2009; *Zhang and Wang,* 2013; *Ba et al.,* 2014). Understanding what controls variability in AMOC and MHT remains an important issue in climate sciences.

In recent years, continuous satellite and in-situ observations along with readily available modeling results have allowed progress in understanding variability in Atlantic ocean circulation. Satellite altimetric sea surface height (SSH) began to be available October 1992 and has allowed a continuous representation of the surface geostrophic flow anomalies (*Ducet et al.,* 2000). The subpolar gyre (SPG) shows an increase in SSH during the 1990s, and this has been interpreted as

a decline of SPG strength (*Häkkinen and Rhines,* 2004, 2009; *Lohmann et al.,* 2009; *Böning et al.,* 2006). The collaborative RAPID-MOCHA (Rapid Climate Change - Meridional Overturning Circulation and Heatflux Array) mooring array has been continuously measuring the AMOC and MHT at 26.5°N in the North Atlantic Ocean since 2004 (*Cunningham et al.,* 2007) and shows variations in AMOC and MHT including a large drop of AMOC in 2009. The CMIP5 (Coupled Model Intercomparison Project Phase 5) provides a framework for coordinated climate change experiments and make it possible to compare model results across divergent coupled models (*Taylor et al.,* 2012), and the results of these modeling experiments are available to the community.

The overall objective of this thesis is to examine the variability of large-scale ocean circulation and the MHT in the Atlantic, especially in the North Atlantic Ocean using observations and models. We aim to investigate the following questions: (1) What are the characteristics of the variability of the ocean circulation and MHT on different timescales? (2) What external forcing controls these characteristics? We address these questions from different perspectives in each chapter of this thesis.

In Chapter 2, we take advantage of the twenty-year altimetric SSH records and examine what portion of the observed SSH changes are from the surface heat flux and winds with/without bottom topography in the North Atlantic on seasonal and interannual-to-decadal timescales. On the seasonal timescale, we concentrate on the contributions of thermosteric height and Rossby wave to SSH in different locations. On interannual-to-decadal timescale, the focus is on the role of the Rossby wave and topography that influences the response of the SSH to changes in the wind. This study helps understanding the effect of topography on the ocean circulation in the

high latitude. Chapter 2 is identical to *Zhang et al.*, written with co-authors K. A. Kelly and L. Thompson.

In Chapter 3, on decadal timescale perturbed experiments and 1000-year control simulation in GFDL coupled model CM2.1 are used to investigate the evolution of AMOC and its related upper ocean heat content (UOHC), when external buoyancy forcing is added to the high latitude of the North Atlantic. The mechanism responsible for the leading mode of UOHC in the extra-tropical North Atlantic is explored. This analysis suggests that the slow southward advection of the AMOC anomaly and related convergence of the MHT anomaly is crucial for the evolution of UOHC. This study provides the physical mechanism for potential decadal prediction of temperature in the extra-topical North Atlantic. Chapter 3 is identical to *Zhang and Zhang* (resubmitted to *GRL*).

In Chapter 4 the interannual MHT anomaly in the Atlantic tropic and subtropics is studied. Seven historical simulations from climate models in the CMIP5 and one hindcast simulation from the isopycnal ocean model GOLD (Generalized Ocean Layer Dynamics) from 1971 to 2009 are used. All of them show that the leading mode of the interannual MHT anomaly has same sign from the southern subtropics to northern subtropics with a maximum in the tropics. We investigate the contributions of Ekman and geostrophic heat transport to this MHT coherence structure, the key for interhemispheric transport and the relationship between wind forcing and MHT variability. This work explores what controls the interannual MHT coherence structure based on the current knowledge of characteristics of the interannual MHT. By comparing the results in an ocean-only simulation along with analysis of CMIP5 coupled models, we can strengthen our conclusions about the linkages between wind driven circulation changes and MHT variability. Chapter 4 is written with co-authors L. Thompson and K. A. Kelly.

Chapter 2. THE ROLE OF HEATING, WINDS AND TOPOGRAPHY ON SEA LEVEL CHANGES IN THE NORTH ATLANTIC

2.1 Introduction

Sea surface height (SSH) variations in the open ocean are owing to both a dynamic response to changes in winds and a thermodynamic response to buoyancy forcing. Using a simplified framework on seasonal-to-interannual timescales *Vivier et al.* (1999) showed that the contributions from local heating, local heave from Ekman pumping, Rossby waves, and topographic Sverdrup response are all important in the North Pacific, although their relative contributions vary with latitude.

In the North Atlantic changes in subpolar gyre circulation have been inferred from changes in satellite observation of SSH. During the 1990s, SSH in the subpolar gyre (SPG) increased during the 1990s. This has been interpreted as a decline of SPG strength (*Häkkinen and Rhines,* 2004, 2009; *Lohmann et al*., 2009; *Böning et al.,* 2006). *Häkkinen and Rhines* (2004) suggest that the weakening SPG in 1990s might be due to the lack of deep convection from local buoyancy forcing that then drives changes in the SPG strength. However, using an ocean general circulation model, *Böning et al.* (2006) show that the decline in the SPG could be caused by decadal variability of both heat flux and wind stress linked to the North Atlantic Oscillation (NAO) (*Hurrell,* 1995). *Esselborn* and *Eden* (2001) interpret the SSH changes from 1992 to 1998 using an ocean model, and argued that the NAO related wind-stress driven changes dominate those driven by changes in buoyancy forcing. *Lohmann et al.* (2009) also demonstrate that the SPG weakening in mid-1990s is a joint effect of a sudden NAO drop in 1995-96 and the ocean response to the strong persistent positive NAO from 1989 to 1995. *Li et al*. (2012) show

that low frequency variations of the SSH anomaly in the subpolar North Atlantic are negatively correlated with the time-integrated NAO, while *Cromwell* (2006) shows that there is no significant correlation between the instantaneous low frequency NAO and leading principal components of SSH. These divergent results suggest that more study of the causes of the observed changes in SSH is needed.

The Sverdrup relation (*Sverdrup,* 1947) describes the large-scale ocean circulation response to the wind, connecting the wind stress curl and meridional transport in the ocean interior. Over half of the 30 Sv ($1\ Sv = 10^6 m^3 s^{-1}$) of meridional transport in the Florida Current at 24°N in the North Atlantic can be explained by the return flow of the Sverdrup transport (*Schmitz et al.,* 1992), with the remainder coming from the thermohaline circulation. This suggests that the response of SSH to winds via the Sverdrup balance could explain some of the low frequency changes in large-scale sea level. However, the simplest Sverdrup balance does not hold where there is significant vertical velocity at the base of the thermocline that results from either large-scale upwelling or from the interaction of the barotropic flow with bottom topography (*Marshall*, 1995; *Wunsch and Roemmich*, 1985). When topography is important, the barotropic flow is controlled by the background potential vorticity f/H (where f is the Coriolis parameter and $H(x,y)$ is the topography). Topography becomes important for regions outside the tropics where stratification is weak and f is large (*Koblinsky*, 1990). Using absolute geostrophic velocity from Argo (*Gray and Riser*, 2014) showed that the Sverdrup balance agrees with observations primarily in the tropics and subtropics of the Pacific and Atlantic. *Vivier et al.* (1999) used a barotropic topographic Sverdrup model to explain SSH variability in the North Pacific and found that the topographic Sverdrup balance dominates the SSH variability north of 40°N in the Pacific Ocean on seasonal-to-interannual timescales. Both of these studies are

consistent with the results of *Koblinsky* (1990). Basin-scale Rossby wave adjustment also plays a significant role in ocean circulation and SSH variations. *Zhang and Wu* (2010) showed that a linear first-mode baroclinic Rossby wave model explained up to 64% of the SSH variance in the tropical and eastern subtropical North Atlantic. *Cabanes et al.* (2006) also noted that Rossby waves explain 70% of the interannual sea level variations between 18°N and 20°N.

The goal of the present study is to use simplified models to provide a quantitative description of the roles of surface heating and winds in controlling seasonal and interannual-to-decadal SSH variability in the North Atlantic and to examine the role of topography in controlling the ocean response. This paper is organized as follows. The data processing and model configurations are presented in sections 2 and 3. Section 4 gives the comparison between modeled and observed sea level changes on seasonal and interannual-to-decadal timescales and the role of the NAO in controlling the SSH variability. We present our conclusions in section 5.

2.2 Data

SSH from satellite altimetry (from TOPEX/Poseidon and Jason-1, 2 altimeters) was mapped by the Archiving, Validation and Interpretation of Satellite Oceanographic data (AVISO) onto a 1/3 degree, weekly grid from 1993 to 2012 (*Ducet et al.,* 2000). For the comparison to the models described in Section 3, which do not produce mesoscale eddies, we applied a Gaussian spatial filter (400 km full-width at half maximum) to the gridded SSH. We used 12-hourly ERA-Interim net surface heat flux with 1.5° grids from 1993 to 2012 (*Berrisford et al.*, 2011) to evaluate the contribution of heating/cooling to sea level changes. In Section 5, we compared the thermosteric results from ERA-Interim product with those from another net surface heat flux, which is a combination of 0.5° daily turbulent flux in the OAFlux (Objectively Analyzed Air-sea

Fluxes) project (*Yu et al.,* 2008) and 1° monthly radiative fluxes from the NASA GEWEX SRB (Surface Radiation Budget) project (*Zhang et al.,* 2015) and from the CERES/EBAF product (*Kato et al.,* 2013). The SRB radiative flux goes until 2007, so we merged it with the CERES/EBAF radiative flux to get a longer period until 2012. High-resolution surface wind stress from 1993 to 2012 was obtained from the European Centre for Medium-Range Weather Forecasts (ECMWF) operational model with a grid of about 1.125° and 6 hours. Wind stress curl maps were computed using Stokes' theorem as in *Vivier et al.* (1999). For ocean depth we used the one-minute Smith and Sandwell Global Topography Dataset v17.1 from satellite altimetry and ship depth soundings (*Smith and Sandwell,* 1997). The topography was smoothed by a running average box of 4° × 4°, consistent with *Cummins* (1991).

The domain in all the models in this study is the North Atlantic (10°N-65°N, 0-80°W). All the data sets were interpolated onto a 1°×1° model grid and monthly time intervals from 1993 to 2012 unless otherwise noted. We forced the Rossby wave model with daily wind stress curl at a daily time step to satisfy the model Courant–Friedrichs–Lewy condition, and then the model results were monthly averaged.

2.3 Model configurations

Four separate models were constructed to examine the SSH response to local heat flux and wind forcing in the presence of topography.

2.3.1 Thermosteric height model

Surface buoyancy flux has a role in controlling SSH variability through steric height changes, the expansion or contraction of the water from density changes. In this model we only considered local thermal effects, that is, the thermosteric height changes forced by net surface heat fluxes.

We neglect the local steric height changes from salinity variability due to its small regional contribution throughout the tropics and subtropics (*Chambers et al,* 1997; *Gill and Niller*, 1973; *Willis et al.,* 2004) and non-local steric height changes from advection and the mixing of water from other regions.

The thermosteric response η_{steric} to surface heating (*Vivier et al.,* 1999; *Kelly and Thompson*, 2002) is given by

$$\frac{\partial \eta_{steric}}{\partial t} = \frac{\alpha Q_{net}}{\rho c_p} \tag{2.1}$$

where α is the coefficient of thermal expansion, calculated from monthly temperature and salinity fields from *Levitus et al.* (1994) (details in *Vivier et al.* (1999)), Q_{net} is the net surface heat flux, ρ is the density of seawater and c_p is the specific heat of seawater. We assume that ρ and c_p are constant.

Estimates of thermosteric height in (2.1) are obtained by integrating monthly net surface heat flux in time from 1993 to 2012 at every point. We remove a linear trend in η_{steric} at each point after integration to account for mean biases in the fluxes as well as compensation by mean advection. We refer to the altimetric SSH after removing the thermosteric component as nonsteric SSH.

2.3.2 Sverdrup models

In the quasi-geostrophic limit and when the timescale is long relative to the time it takes for Rossby waves to propagate across the basin, the steady state linear barotropic vorticity equation can be used to find the sea level distribution. Following *Vivier et al.* (1999) the change in sea level following the path s is governed by

$$\frac{\partial \eta}{\partial s} = \frac{f}{\rho g J(s,q) H} curl(\frac{\vec{\tau}}{H}) \tag{2.2}$$

where η represents the sea level, $\vec{\tau}$ is the wind stress, g is gravity and H is the ocean depth. Here s represents the curvilinear coordinate along constant contours $q = f / H$ from east to west and $J(s,q) = \pm \| q \|$ is the Jacobian matrix determinant.

Cabanes et al. (2006) argued that the contribution of Rossby waves driven by the eastern boundary condition is limited to the vicinity of the eastern boundary. The currents and associated SSH near the coast might be controlled by shallow topography, coastally trapped waves, mixing and alongshore winds, whose character and dynamics are different from the large-scale ocean dynamics. Therefore, we used the altimetric SSH a few degrees away from the coast as the eastern boundary condition for (2.2). The eastern boundary is along 21°W for 10°N-24°N and along 12°W for 30°N-65°N (Figure 2.1, brown line in the eastern basin).

We outline two Sverdrup models with different versions of H in (2.2), representing different dynamics.

a) Constant-depth Sverdrup (CS) model. Using a constant depth H in (2.2) this model becomes the classic Sverdrup balance (*Sverdrup,* 1947). With a depth H of 1000m, consistent with the choice of H in *Wunsch and Roemmich* (1985), it represents the ocean layer above the thermocline, assuming a motionless lower layer. We will also discuss the effective thermocline depths of best fit to the SSH observations later. The integration of wind stress curl from the eastern boundary is along fixed latitudes. With $\beta = \partial f / \partial y$ (2.2) becomes

$$\frac{\partial \eta}{\partial x} = \frac{f}{\rho g H \beta} curl(\vec{\tau}) \tag{2.3}$$

b) Topographic Sverdrup (TS) model. With a spatially varying depth H in (2.2) the model includes the influence of topography on the barotropic flow and (2.2) is integrated along $q = f / H$ contours. Topography causes a large-scale deviation of the contours from zonal uniformity, particularly over the Mid-Atlantic Ridge and near the Labrador Sea (Figure 2.1). Over the shallowest part of the Mid-Atlantic Ridge near 40°N and 30°W, the f / H contours close, making the integral in (2.2) undefined. We interpolate the model results from contours that do not close into this small region; the interpolation does not qualitatively change the final result. We also ignored and masked regions that have depths less than 2000 m, such as the shallow area near the east coast of North America and near the Mid-Atlantic Ridge.

2.3.3 Rossby wave model

The Rossby wave model used here is the 1.5-layer reduced gravity model with a motionless lower layer (*Meyers,* 1979), which allows for time dependence of the solution, in contrast to the steady state Sverdrup models. The linear vorticity equation under the long wave assumption can be derived in terms of the sea level changes η as

$$\frac{\partial \eta}{\partial t} - C_R \frac{\partial \eta}{\partial x} = -\frac{g'}{\rho g f} curl(\vec{\tau}) \tag{2.4}$$

as used in *Kelly and Thompson* (2002). The theoretical westward phase speed of long Rossby wave is $C_R = \beta R_d^2$, where R_d is the Rossby radius of deformation and g' is the reduced gravity. The Rossby wave equation (2.4) and the CS equation (2.3) are similar except that the Rossby wave equation includes wave propagation.

Qiu (2002) pointed out that a damping term helps to improve the prediction of the SSH in the North Pacific. Here we also added a damping term in (2.4) to give

$$\frac{\partial \eta}{\partial t} - C_R \frac{\partial \eta}{\partial x} = -\frac{g'}{\rho g f} curl(\vec{\tau}) - \varepsilon \eta \tag{2.5}$$

where ε is the damping coefficient with units of s^{-1}. *Schneider et al.* (2002) used a value of ¼ yr^{-1} for this coefficient in the North Pacific Ocean. We tried several values for ε in our Rossby wave model and found that the results are not particularly sensitive to the damping coefficient, consistent with *Zhang and Wu* (2010). We find that ε equal to 1/20 of $C_R / \Delta x$ gives a solution that best matches the observed propagating SSH signal.

Chelton and Schlax (1996) showed that there are large discrepancies between observed and theoretical Rossby wave phase speeds. They derived an empirical Rossby wave speed by fitting the slope of propagating SSH anomalies on a Hovmöller diagram. Following their method we derived an initial guess of the phase speed at C_R each latitude. In addition to the phase speed and the damping coefficient, the reduced gravity g' is a parameter that can be optimized. Using our first guess of the phase speed we allow g' to vary between 0.02 and 0.06 ms^{-2} and C_R to vary within $0.05\, m/s$ around the first guess. We run the Rossby wave model with different combinations of g' and C_R to find values that give the best match with altimetric SSH anomalies at each latitude. The best match (Figure 2.2) gives the smallest error (distance) on a Taylor diagram (*Taylor,* 2001), which takes into account both correlations and relative magnitudes of model and observations. For simplicity, we only considered g' (not shown) and C_R as functions of latitudes.

Table 2.1 summarizes the characteristics of all the wind-driven models used in this study. Optimizing g' and C_R in the Rossby wave model is analogous to tuning the only adjustable parameter H in the CS model.

Table 2.1 Summary of models

Model	Parameter	Integration	$\partial\eta / \partial t$
Constant-depth Sverdrup (CS)	H (1000m)	Along latitudes	NO
Topographic Sverdrup (TS)	None	Along f / H	NO
Rossby Wave	g' and C_R	Along latitudes	YES

2.4 Results

We examined the predicted sea level response to heating and winds using the models described in Section 3 and then compared these modeled sea level changes with observations of altimetric SSH on seasonal and interannual-to-decadal timescales, respectively.

2.4.1 Seasonal SSH variations

We first investigated the seasonal SSH variability in the North Atlantic and only consider the thermosteric height (2.1) and Rossby wave propagation (2.5), as we do not expect the Sverdrup models to hold at these times scales (Table 2.1)

The spatially smoothed altimetric SSH anomalies (Figure 2.3a, 2.4a, 2.5a) have strong seasonal variability, which overwhelms low-frequency signals and is nearly zonally uniform at all latitudes. At 61.5°N, both the Rossby wave model (Figure 2.3b) and thermosteric height model (Figure 2.3d) explain part of the seasonal SSH signals. At 36.5°N the Rossby wave model has weak seasonal variability (Figure 2.4b) and a large fraction of seasonal SSH signals can be explained by the thermosteric height (Figure 2.4d). Nonsteric height anomalies are relatively large (Figure 2.4e), but are primarily interannual. The smoothed SSH at 12.5°N (Figure 2.5a) has both a zonally uniform component as well as a strong westward propagating component. However, the zonally uniform thermosteric height (Figure 2.5d) is out of phase with the observed

SSH, which results in nonsteric seasonal SSH variability that is stronger than the observed SSH (compare Figure 2.5a and e). We find that the Rossby wave model (Figure 2.5b) does well in representing the seasonal SSH variability at this latitude. After the Rossby waves are removed from observed SSH, the residuals (Figure 2.5c) have a fairly weak seasonal cycle and little westward propagation, indicating that the wind-driven Rossby waves make an important contribution to the seasonal cycle of altimetric SSH at 12.5°N.

To further quantitatively investigate the contributions of the models to the variance of altimetric SSH, we used the skill defined as

$$S = (1 - \frac{< (\eta_o - \eta_p)^2 >}{< \eta_o^2 >}) \times 100\% \tag{2.6}$$

where η_o and η_p are observed altimetric SSH anomalies and predicted (modeled) sea level changes, respectively. Angle brackets represent time averaging. Skill is close to 100% for a good match between observations and model outputs in both phase and magnitude, but is low or even negative for a poor match. On this seasonal timescale we applied a 0.5-1.5 year bandpass filter to both SSH and model results. The skill for bandpassed thermosteric height directly compared with bandpassed SSH shows that the seasonal SSH in most of the North Atlantic can be explained by the seasonal thermosteric height changes north of 18°N, especially for the basin north of 40°N and between 18°N-22°N (Figure 2.6a). This is consistent with *Ferry et al.* (2000) who use a general ocean circulation model and show a balance between heat flux induced changes in steric height and seasonal SSH north of 20°N. The contribution of bandpassed Rossby waves to bandpassed SSH is high between 10°N and 15°N, which may be owing to seasonal wind stress patterns associated with the migration of the Intertropical Convergence Zone (ITCZ) (*Kelly and Thompson*, 2002). East of Greenland the high skill of the Rossby wave model is owing to a local

Ekman pumping response with a balance between the time-dependent term on the left-hand side and the wind forcing term on the right-hand side in (2.5). The influence of the eastern boundary is limited to a few degrees away from the boundary on the seasonal timescale.

The relative contributions to the seasonal cycle of SSH depend on location. At 61.5°N, 35.5°W the seasonal thermosteric height (Figure 2.7a, dashed red, for location see Figure 2.6) and seasonal Rossby wave (Figure 2.7a, dotted magenta) are both in phase with the variations in observed seasonal SSH (Figure 2.7a, solid black). At 36.5°N, 39.5°W the SSH has a larger seasonal cycle than that at 61.5°N and 12.5°N; the seasonal thermosteric signal is partially in phase with SSH and has a skill of about 55%, while the Rossby wave has a small contribution (Figure 2.7b). At 12.5°N, 39.5°W the Rossby wave skill is about 85%; in contrast the seasonal cycle of thermosteric height is completely out of phase (negative skill) with SSH (Figure 2.7c).

2.4.2 Interannual-to-decadal SSH variations

To evaluate the sources of interannual-to-decadal variability of SSH anomalies we applied a 1.5 year lowpass filter to model results and removed the long-term linear trend. Using Empirical Orthogonal Function analysis (EOF), we compare the dominant patterns of variability that each model predicts with that of the observed SSH (Figure 2.8), which has not been done previously. The spatial pattern of the leading mode (EOF1) of observed interannual-to-decadal SSH (Figure 2.8a) displays a tripole structure with opposite signs between the Gulf Stream (GS)/North Atlantic Current (NAC) regions and the subpolar/subtropical gyres, with 27% fraction of variance explained. This pattern has also been found by previous studies (*Häkkinen and Rhines*, 2001; *Esselborn and Eden,* 2001; *Lorbacher et al*, 2010). The first principal component (PC1) of the EOF analysis for SSH (Figure 2.8f, black) together with its EOF1 (Figure 2.8a) shows minima in subpolar SSH in 1995, 2000 and 2009, while maxima occur in 1998, 2003 and 2010.

The first EOF for the interannual-to-decadal thermosteric height model (2.1) (Figure 2.8b), the Rossby wave model (2.5) (Figure 2.8c) and the CS model (2.3) (Figure 2.8d) have similar large-scale spatial structures as that of the observed SSH with the fraction of variance explained at 42%, 29% and 41%, respectively. However, PC1 of thermosteric height (Figure 2.8f, red dashed line) is not significantly correlated with PC1 of the observed SSH. The EOF1 of the CS model (Figure 2.8d) has a similar pattern to that of the observed SSH (Figure 2.8a), but with a larger magnitude, especially in the subpolar region; the correlation for PC1s of SSH and CS is 0.49 (95% significance level is 0.32). The TS model (Figure 2.8e) does not reproduce the dominant spatial pattern and amplitude of the observed SSH. Despite this the correlation between PC1s of TS and SSH is 0.48 (95% significance level is 0.42). The relatively strong correlations for both the CS and TS PC1 with the observed SSH PC1 occur because both depend on the large-scale low frequency wind-stress curl changes. Differences in amplitude result from differences in the dependence of the solution on the thickness of the layer over which the wind-driven circulation occurs. In TS the circulation is distributed throughout the water column resulting in a smaller SSH anomaly; in the CS model the layer depth was set at 1000m. Finally the Rossby wave model EOF1 is similar to that of SSH with a PC1 correlation of 0.79 (95% significance level is 0.39), reproducing the interannual-to-decadal basin-scale SSH variability best among the models from both the spatial and temporal perspectives. The wave propagation takes longer to cross the North Atlantic basin at middle and high latitudes, which makes the steady assumption in the Sverdrup models less appropriate and which explains why the Rossby wave model performs better at higher latitudes.

To further quantitatively evaluate the models against the observations we also calculated the skill for each model (Figure 2.9) as a function of location. The thermosteric height does well in

reproducing the interannual-to-decadal altimetric SSH variations east of Greenland, in mid-basin between 40°N and 50°N and in the eastern basin between 25°N and 35°N (Figure 2.9a). The skills for the Rossby wave, CS and TS models (Figure 2.9b, c and d) are all high in the eastern half of the basin south of 30°N. In this region the eastern boundary condition dominates the modeled sea level variability and models are less sensitive to either local wind anomalies or topography. However the Rossby wave model is the only wind-driven model that reproduces the interannual-to-decadal SSH between 30°N and 50°N (Figure 2.9b). Furthermore, the Rossby wave also works in the subpolar region between 20°W-40°W, which may be related to the interannual Ekman pumping (*Cabanes et al.,* 2006). The TS model performs well in the SPG with skill up to 90% east of Greenland (Figure 2.9d), where the f/H contours are closely spaced and the water column is less stratified. The magnitudes from the CS model are too large in the SPG (not shown), owing to its assumption of flow being confined to the upper ocean.

A comparison of the interannual-to-decadal model results with SSH in 2005 (Figure 2.10) is consistent with the EOF and skill analysis. Note that the TS model in 2005 (Figure 2.10e) reproduces the spatial SSH pattern well, including the deviation from zonal symmetry near 40°N due to the Mid-Atlantic Ridge, a feature that is not explained by any other models. It is likely due to the distortion of potential vorticity (PV) contours in the TS model. However, this topographically induced deviation does not occur every year.

We can obtain an effective thermocline depth for the CS model as a function of latitude (Figure 2.11, solid dot) by tuning H to match the model and observed variance. Here we only show the effective thermocline depths north of 30°N because the eastern boundary condition dominates the solution south of 30°N. This depth is compared with zonally averaged actual ocean depth (Figure 2.11 dashed line). The effective thermocline depth increases from 1200m at

30°N to several thousand meters at higher latitudes, consistent with the more barotropic flows there; however, the ocean depth actually decreases from 4000-5000m in the subtropics to less than 3200m north of 53°N, so that effective thermocline depth is greater than the actual ocean depth north of 53°N. The inability to tune the CS model sensibly to improve its skill shows that the increased skill of the TS model is not from the larger value of H, but is instead from the deviation of the background PV contours from zonal lines, consistent with previous results from *Koblinsky* (1990) and *Vivier et al.* (1999). It also agrees well with *Koblinsky* (1990) and *Marshall* (1995) that stronger stratification and stronger β isolates the wind-driven circulation from the topographic distortion of PV at lower latitudes.

2.4.3 Model results from NAO-regressed heat flux and winds

To further understand the low frequency SSH variability we investigated the role of the NAO-related forcing. We modeled the thermosteric height using heat flux regressed onto the NAO index and forced the wind-driven models with winds also regressed onto the NAO index. Monthly heat fluxes or winds are used for all but the Rossby wave model, for which we used daily winds and then smoothed the results to monthly to satisfy the Courant-Friedrichs-Lewy condition.

On the seasonal timescale the skill for the thermosteric height derived from NAO-regressed surface heat flux (not shown) is dramatically decreased (from above 60% to below 30% for most of the basin) compared with that from the full surface heat flux (Figure 2.6a). The skill for the Rossby wave model from NAO-regressed winds (not shown) also declines, from about 55% to below 30% east of Greenland and from about 70% to below 50% between 10°N and 15°N compared with the full winds (Figure 2.6b). These results imply that the NAO plays a minor role on seasonal SSH signals.

On interannual-to-decadal timescales both the thermosteric height and the Rossby wave models using NAO-regressed forcing have substantially reduced skills in most of the basin (not shown), implying a minor influence of NAO on SSH. However, the skill for NAO-regressed winds increases in the subpolar region (e.g. 55°N-59°N, 25°W-40°W, Table 2.2, box shown in Figure 2.9c) from negative values to 38% for the CS model and from 63% to 68% for the TS model. This result indicates that the NAO likely plays a role in controlling SSH in high latitudes through winds on longer timescales (*Zhai and Wunsch*, 2013; *Eden and Willebrand*, 2001; *Esselborn and Eden*, 2001).

Table 2.2 Model Skills (%) in Subpolar Box (55°N-59°N, 25°W-40°W)

Model	Full heat flux/winds	NAO heat flux/winds
Thermosteric Height	23.4	7.3
Constant-depth Sverdrup (CS)	negative	38.2
Topographic Sverdrup (TS)	63.3	68.2
Rossby Wave	23.7	13.9

2.5 Discussion and Conclusion

Using simplified models, the contributions of heating and winds to SSH were examined in the North Atlantic for 1993-2012. On seasonal timescales surface heating contributes most to altimetric SSH changes north of 18°N, while Rossby waves play an important role between 10°N-15°N and east of Greenland. On interannual-to-decadal timescales an EOF analysis shows that the Rossby wave model reproduces the basin-scale SSH signals best among the models with a significant correlation of 0.79 between the PC1s of the Rossby wave model and SSH. The thermosteric height reproduces interannual-to-decadal altimetric SSH variations at several regions outside the tropics. The eastern boundary condition dominates the modeled sea level

forced by winds south of 30°N, where the model results are not sensitive to wind or topography. The Rossby wave model reproduces interannual-to-decadal SSH well in the mid-latitudes (30°N-50°N). The TS model performs well in the subpolar gyre with skill up to 90% east of Greenland, demonstrating the importance of topography in controlling the SSH response to winds there. Furthermore, the TS model suggests some influence of Mid-Atlantic Ridge on interannual-to-decadal SSH. The depth H of the CS model cannot sensibly be tuned to match the TS model, which shows that the spatially varying topography (not the model layer depth) is critical to the ocean response to winds in the subpolar region.

The impact of NAO variability on SSH has been investigated before, but mostly over a shorter time period, 1992 to 1998 in *Esselborn* and *Eden* (2001) and October 1992 to January 2004 for *Cromwell* (2006). *Cromwell* (2006) showed no significant correlation between the low frequency NAO and basin-scale SSH. Spectral analysis of the NAO index showed strong interannual-to-decadal variability throughout the 20th century (*Hurrell and van Loon*, 1997; *Higuchi et al.,* 1999). *Li et al*. (2012) show that low frequency variations of the SSH anomaly in the subpolar North Atlantic are negatively correlated with the time-integrated NAO. Here our models reveal that on interannual-to-decadal timescales both the CS and TS models show increased skill in high latitudes with NAO-regressed winds.

The leading EOF mode of the spatially smoothed SSH explains 27% of the variance; in contrast, the EOF1 of unsmoothed SSH explains only 8% of the variance (not shown). SSH variability has a large contribution from mesoscale processes (*Chelton et. al.,* 2011). Furthermore, except the mesoscale eddies, many other physical processes cannot be explained by the simple models described above. Comprehensive ocean models can include other factors such as more complex vertical structure and changes in stratification and advection (*Wang et. al.,*

2013 and *Ferry et al.,* 2000), halosteric response (*Ivchenko et. al.,* 2008) and SSH changes driven by changes in the meridional overturning circulation (*Ivchenko et. al.,* 2011).

Ferry et al. (200) shows that the relationship between heat flux and sea level changes is sensitive to different heat flux products. Here we compared the thermosteric response to two different flux products, one is ERA-Interim net surface heat flux, the other one is the net surface flux combined from OAFlux turbulent flux and radiative flux by merging SRB and CERES products during 1993-2012. From the comparison of thermosteric height skill patterns for ERA-Interim and OAFlux/SRB/CERES products, we found that those skills are quite similar between products on both seasonal and interannual-to-decadal timescales (not shown). The ERA-Interim data is a reanalysis product from ECMWF, while OAFlux includes ECMWF, but is more heavily weighted toward satellite observations, thus relatively independent. The comparison shows that our analysis of thermosteric height on both seasonal and interannual-to-decadal timescales is robust among heat flux products.

The assumptions and limitations of these simplified models add extra uncertainties to the results. One of the uncertainties is the choice of thermocline depth, which determines the amplitude of the CS model SSH. *Leetmaa et al.* (1977) and *Wunsch and Roemmich* (1985) used 1000m in their calculations of meridional transport in the Atlantic; *Rhines and Young* (1982) suggested that the wind-driven circulation reaches a depth determined by the regions of potential vorticity homogenization; a depth based on an isopycnal could also be used, as in *Hautala et al.* (1994) to examine Sverdrup balance in the subtropical Pacific. Moreover, the Sverdrup balance only holds in the interior ocean where the Rossby number is small. We do not expect it to work near the Gulf Stream or in the western basin.

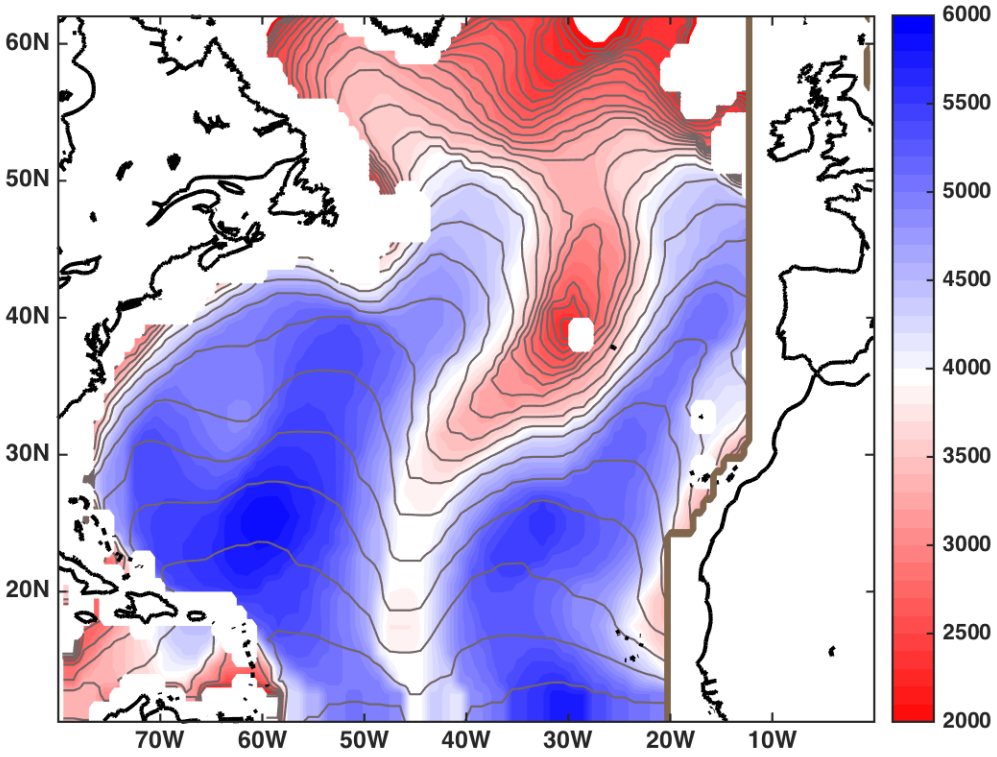

Figure 2.1 Smoothed topography in North Atlantic. The topography shallower than 2000m is not shown. The gray lines are f/H contours. Units are meters. The brown line in the eastern basin is the eastern boundary for the Sverdrup models.

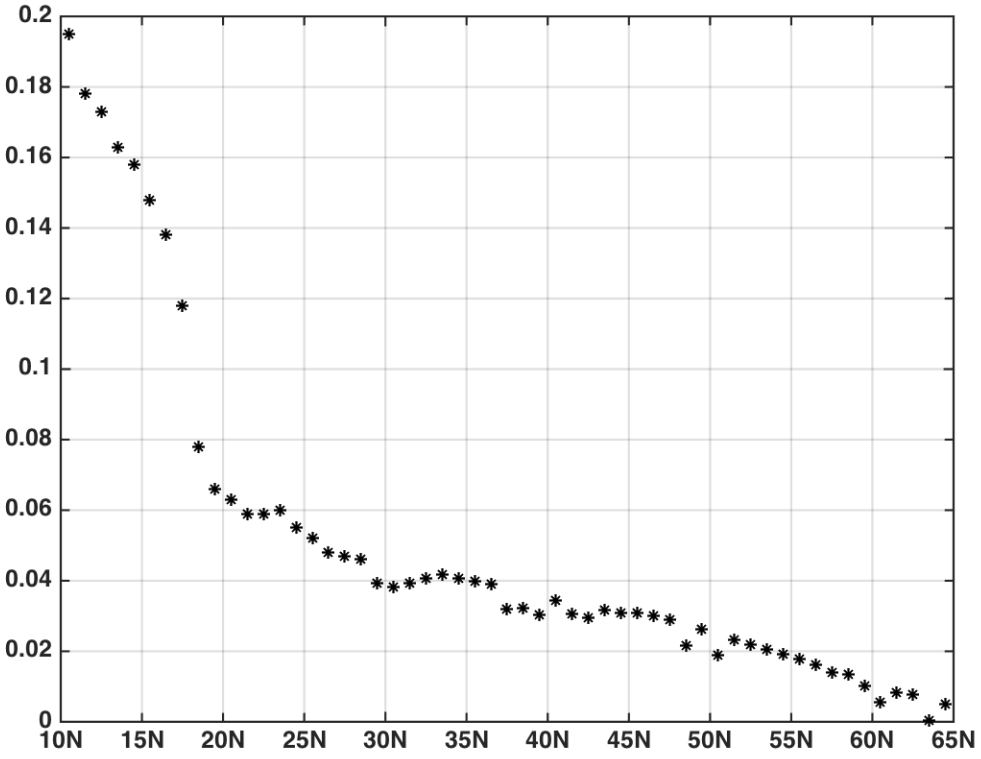

Figure 2.2 Phase speeds for the Rossby wave model at different latitudes. Units are ms^{-1}.

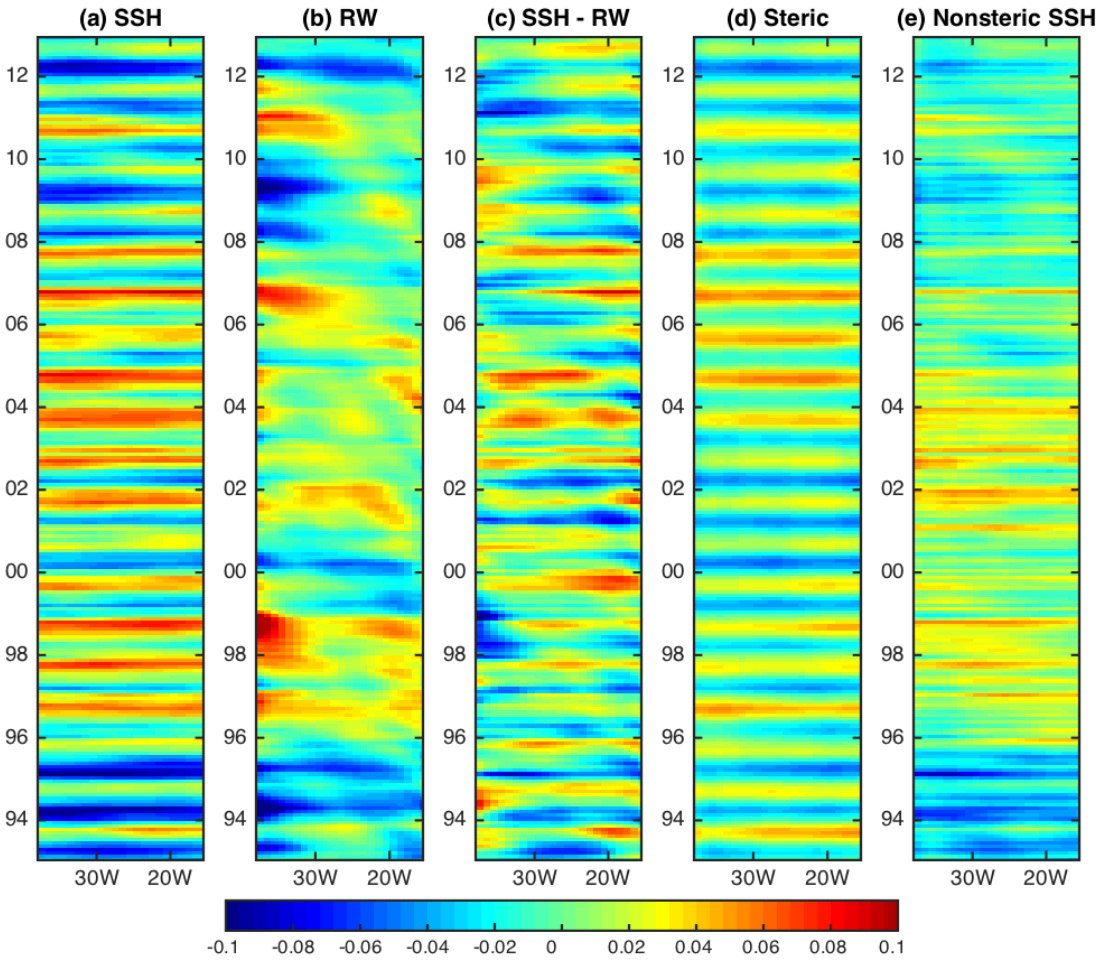

Figure 2.3 (a) altimetric smoothed SSH, (b) Rossby wave, (c) SSH minus Rossby wave, (d) thermosteric height and (e) nonsteric SSH at 61.5°N. Units: m.

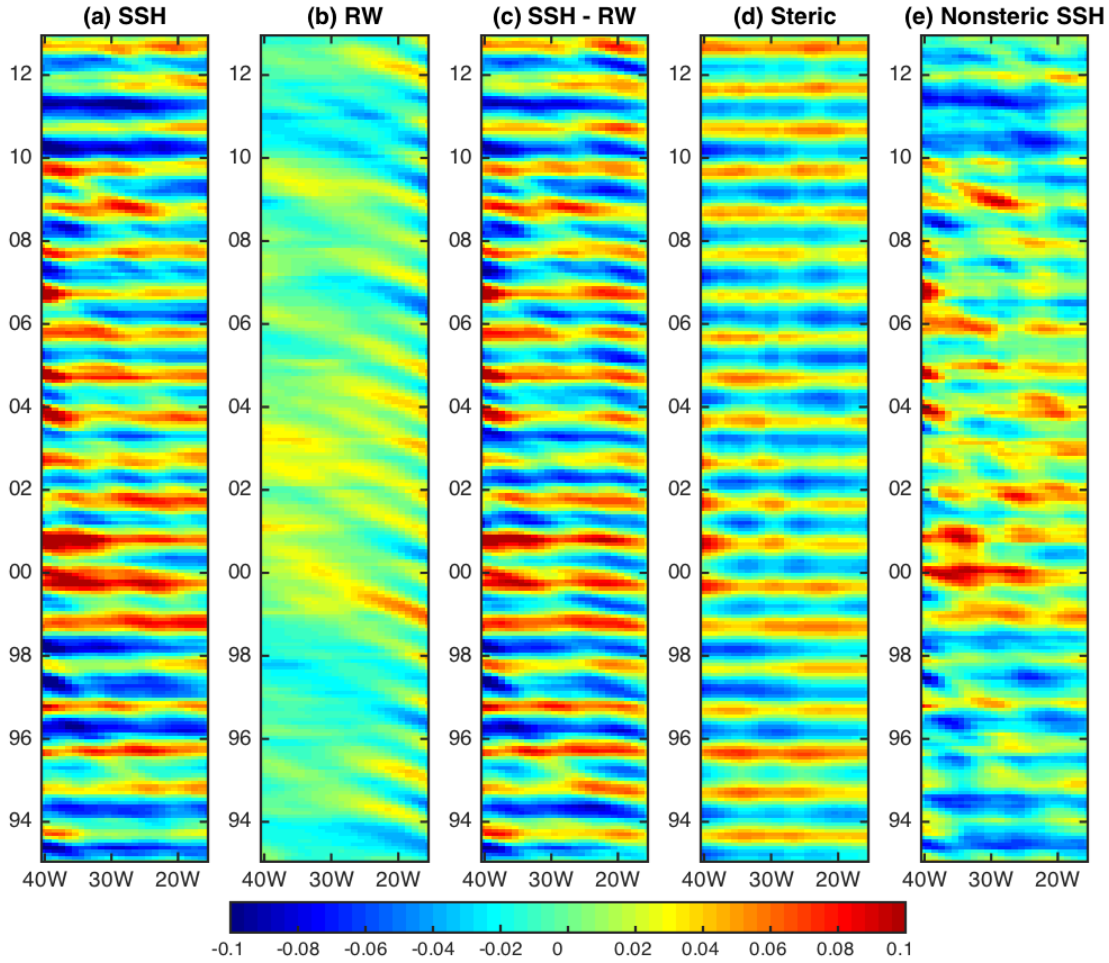

Figure 2.4 Same as Figure 2.3, but for 36.5°N.

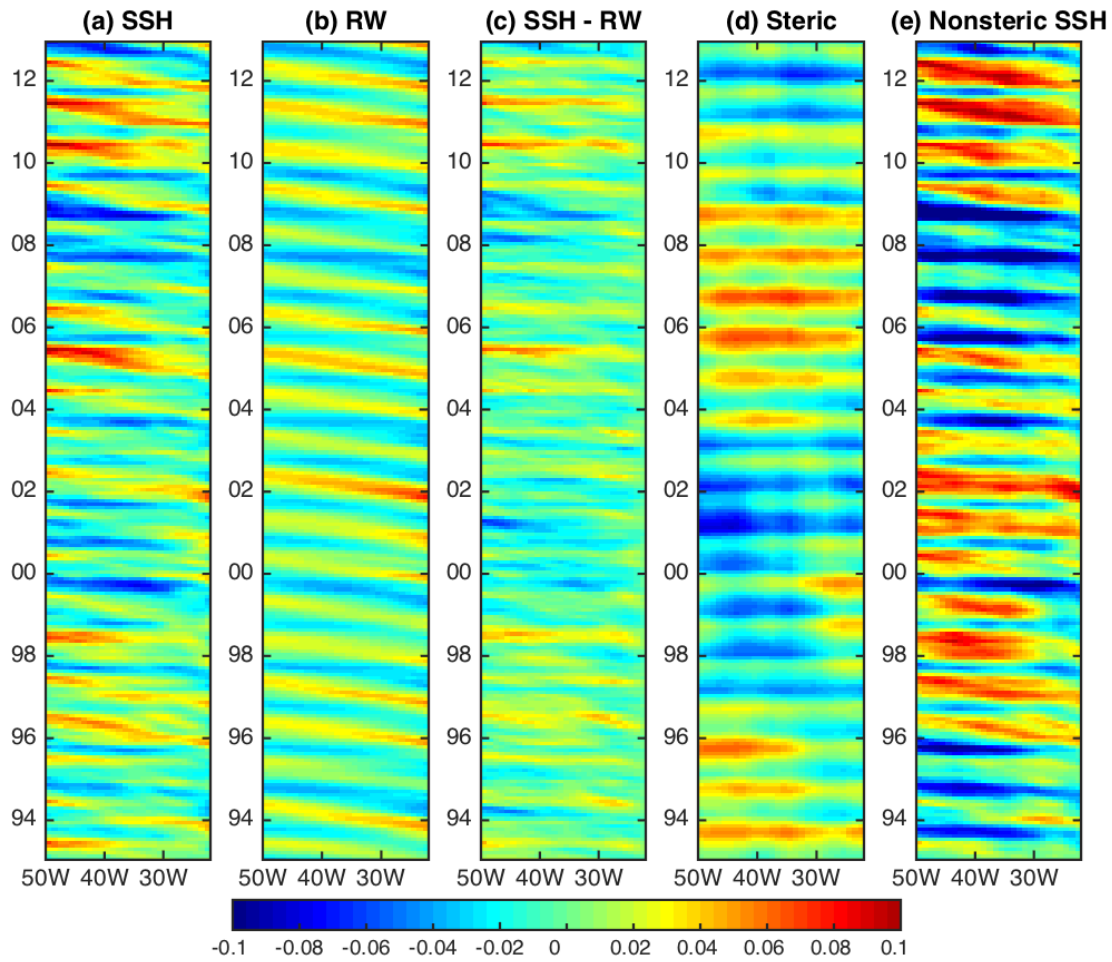

Figure 2.5 Same as Figure 2.3 and 2.4, but for 12.5°N.

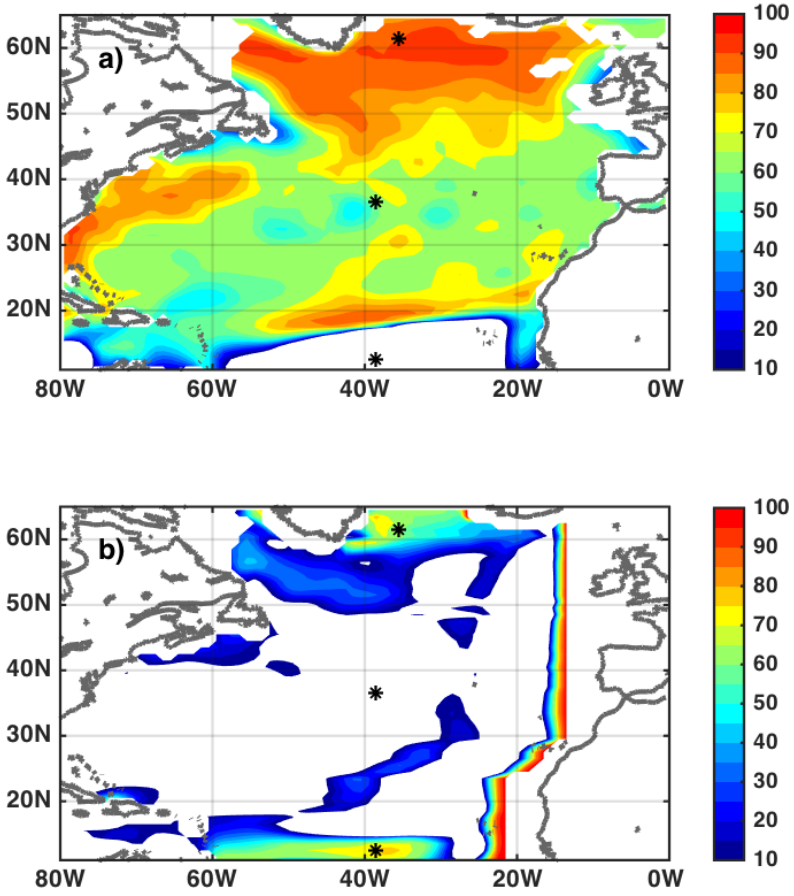

Figure 2.6 Skills (higher than 10%) for (a) thermosteric model and (b) Rossby wave model compared with seasonal SSH. All the signals are band passed for 0.5-1.5 years. Asterisks at (12.5°N, 39.5°W), (36.5°N, 39.5°W) and (61.5°N, 35.5°W) denote locations of time series in Figure 2.7.

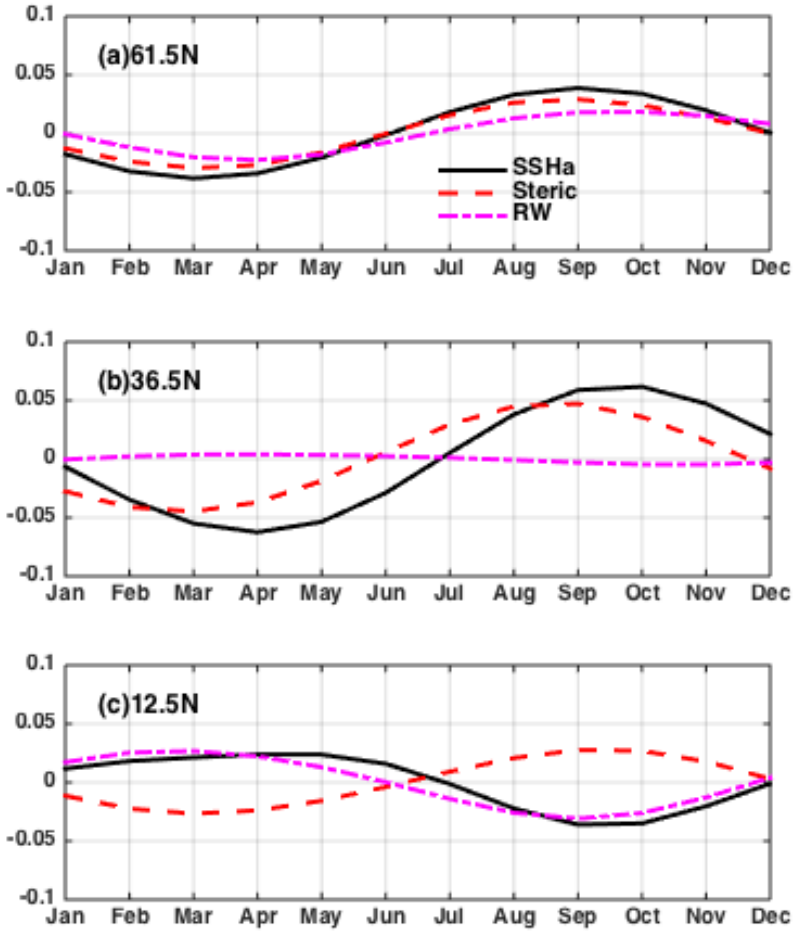

Figure 2.7 Seasonal cycles for SSH (solid black), thermosteric height (dashed red) and Rossby wave propagation (dotted magenta) at different latitudes. (a) for (61.5°N, 35.5°W), (b) for (36.5°N, 39.5°W), and (c) for (12.5°N, 39.5°W).

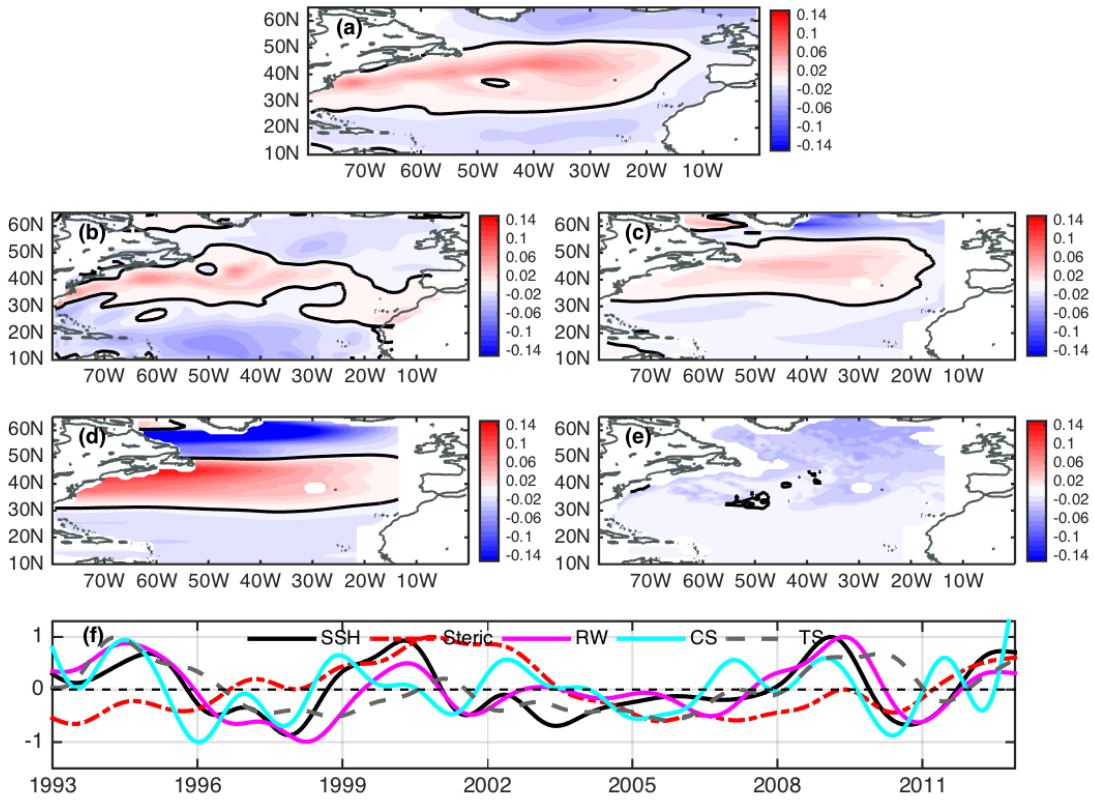

Figure 2.8 EOF1 and PC1 for interannual-to-decadal SSH and model results. EOF1 for (a) smoothed SSH, (b) thermosteric height, (c) Rossby wave, (d) CS model and (e) TS model. Bold black lines in (a)-(e) are the zero contours. The variances explained by these dominant EOFs are 27%, 42%, 29%, 41% and 39%, respectively. Normalized PC1 for SSH (solid black), thermosteric height (dotted red), Rossby wave (magenta), CS (cyan) and TS (dotted grey) are shown in (f). All the fields are 1.5-year lowpass filtered and a linear trend is removed before performing EOF analysis.

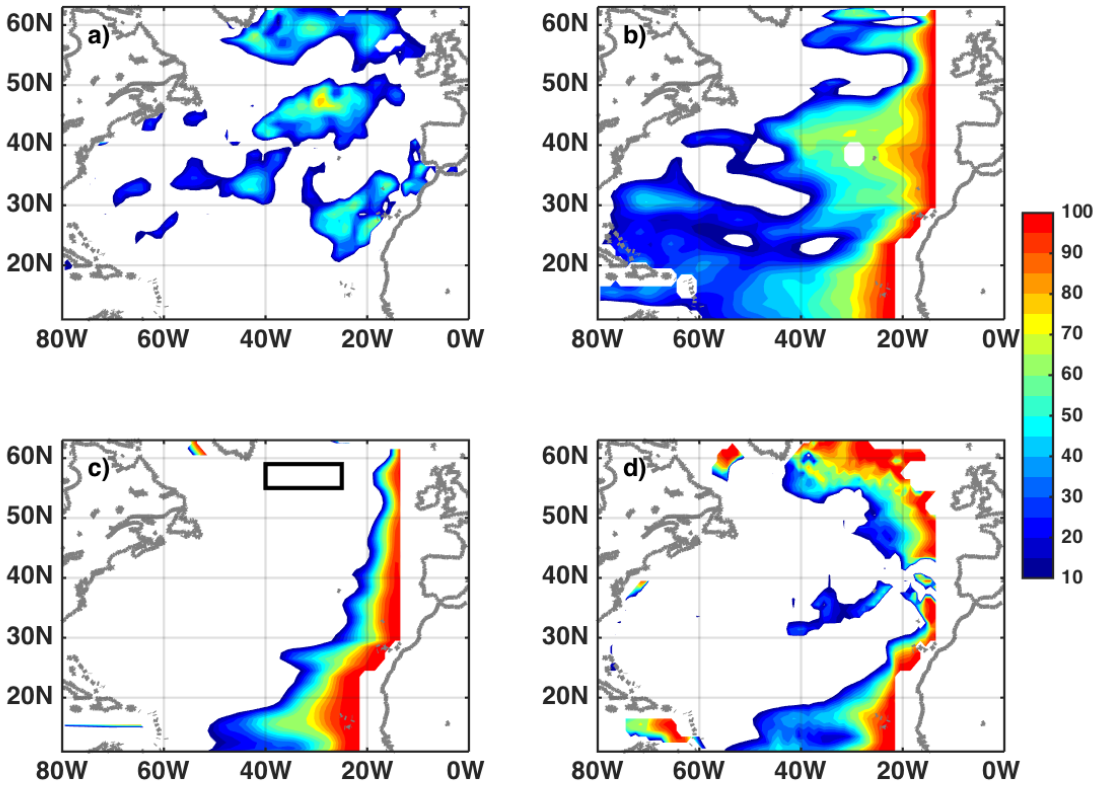

Figure 2.9 Skill (higher than 10%) for models compared with interannual-to-decadal SSH anomalies. Skill for (a) thermosteric height, (b) Rossby wave, (c) CS and (d) TS models. The subpolar box is (55°N-59°N, 25°W-40°W).

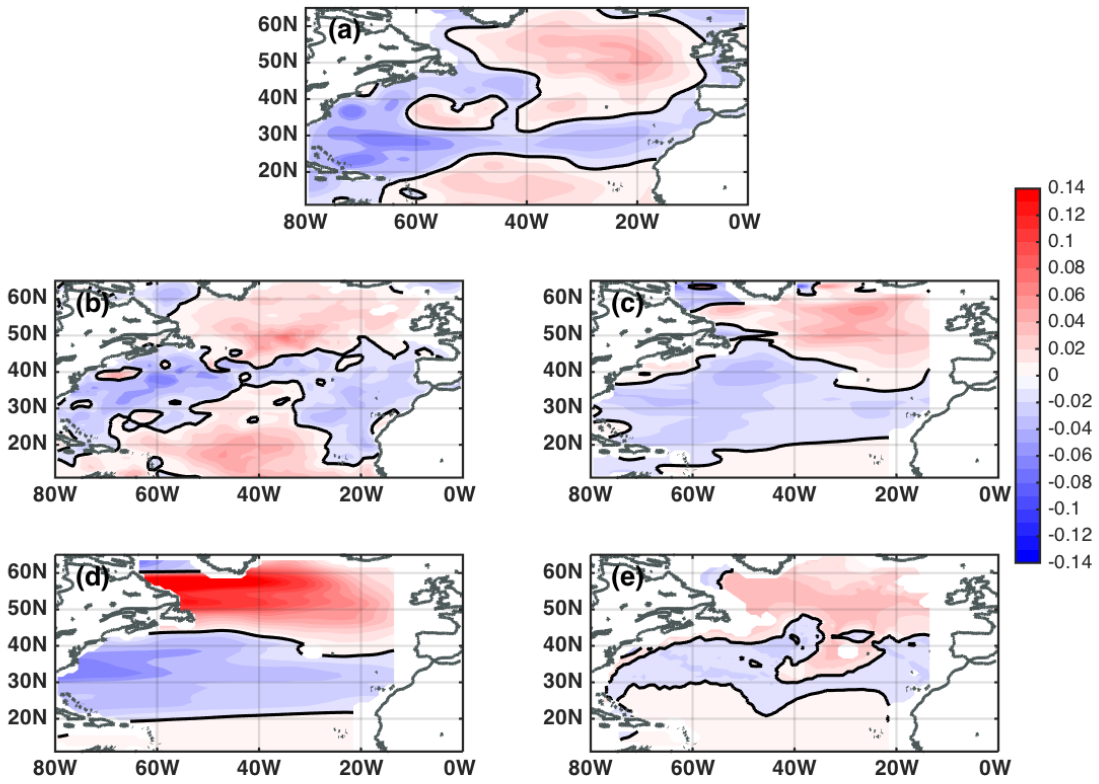

Figure 2.10 Interannual-to-decadal SSH and models in 2005. (a) altimetric SSH, (b) thermosteric height, (c) Rossby wave, (d) CS and (e) TS models. Units are meters.

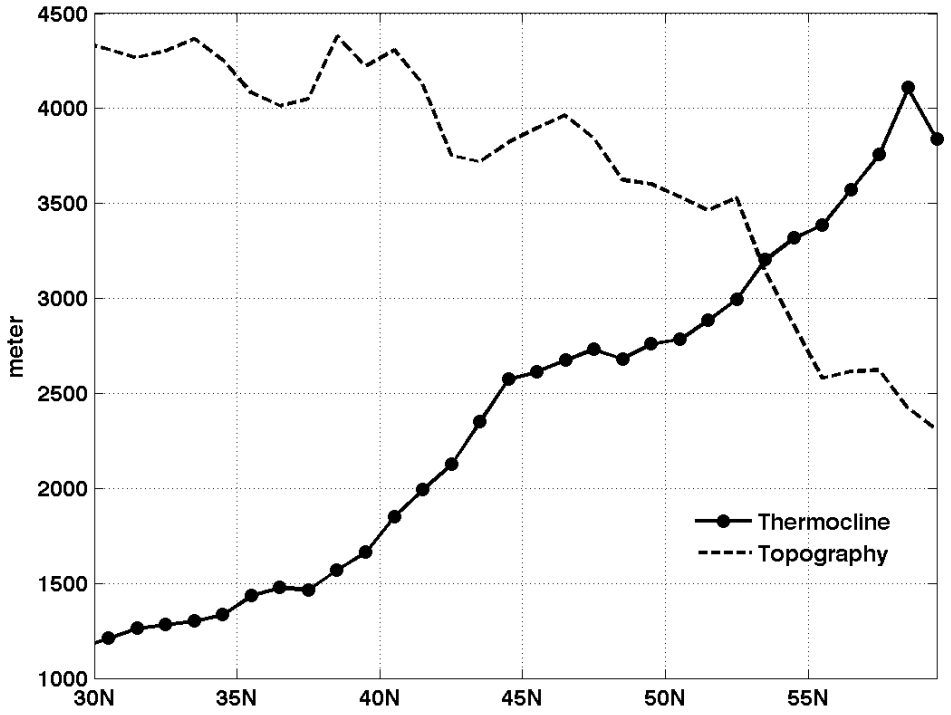

Figure 2.11 Effective thermocline depths (solid dot) and zonally averaged ocean full depths (dashed) at different latitudes. Unites are meters.

Chapter 3. ON THE EVOLUTION OF ATLANTIC MERIDIONAL OVERTURNING CIRCULATION (AMOC) FINGERPRINT AND IMPLICATIONS FOR DECADAL PREDICTABILITY IN THE NORTH ATLANTIC

3.1 Introduction

It has been suggested that AMOC variability is associated with the multidecadal variability in the North Atlantic basin averaged sea surface temperature (SST), the so-called Atlantic Multidecadal Oscillation (AMO) (*Knight et al.,* 2005; *Ting et al.,* 2009; *Zhang and Wang,* 2013; *Ba et al.,* 2014). The AMO has been found to be associated with many regional and global scale climate phenomena at multidecadal timescales, such as the Atlantic Hurricane activity (*Goldenberg et al., 2001; Zhang and Delworth, 2006; Knight et al., 2006*), summer climate over both North America and western Europe (*Sutton and Hodson,* 2005), and Arctic sea ice (*Mahajan et al*., 2011). AMOC variability is also found to be important for the variability of the upper ocean heat content (UOHC) in the extra-tropical North Atlantic, i.e. a positive AMOC anomaly can induce a warming in the subpolar gyre (SPG) and a cooling in the Gulf Stream (GS) region, and this dipole UOHC anomaly is referred to as the AMOC fingerprint (*Zhang,* 2008). Recent decadal prediction studies using different climate models successfully predicted the rapid rise in the UOHC in the North Atlantic SPG during the mid 1990s with initialized ocean state, and suggested that initializing a stronger AMOC at northern high latitudes is the key for such successful predictions of the warm shift in the SPG; meanwhile hindcasts that only consider changes in external radiative forcing and no initialization in the ocean state are not able to predict

the rapid warming (*Robson et al*., 2012; *Yeager et al.,* 2012; *Yang et al.,* 2013; *Msadek et al.,* 2014).

The physical mechanism behind the enhanced decadal prediction skill in the UOHC in the North Atlantic SPG, as well as the linkage between AMOC variability and North Atlantic Ocean temperature, deserve further investigations. In this study, we aim to address the following specific questions:

- Why does a positive AMOC anomaly at northern high latitudes induce a warming in the SPG and a cooling in the GS region after several years, and vice versa?
- Why is the dipole UOHC anomaly (AMOC fingerprint) confined to north of 34°N in the North Atlantic?
- What is the role of the meridional coherence of AMOC variability in the evolution of the AMOC fingerprint?
- Why is there an enhanced decadal predictability in the North Atlantic UOHC (especially in the SPG)?

In a previous study, *Zhang* (2010) found that the AMOC anomaly associated with changes in the North Atlantic Deep Water (NADW) formation exhibits meridional coherence in density space and propagates southward with a slow tracer advection speed between 34°N-55°N due to the existence of interior pathways of NADW in this region (*Bower et al.,* 2009; *Gary et al.,* 2011; *van Sebille et al.,* 2011). Because a substantial portion of the anomalous NADW is advected by the climatological mean North Atlantic deep flow along the interior pathways north of 34°N with the tracer advection speed, the deep branch of the anomalous AMOC propagates with this speed (*Zhang,* 2010), resulting in a several-year time lag in which the subtropical AMOC lags the subpolar AMOC variation. The time lag is consistent with the observed tracer

advection time scale in this region (*Smethie,* 1993), and may provide a more useful predictability. In this study, we found that the southward propagation of the AMOC anomaly with the slow tracer advection speed north of 34°N is crucial for the evolution and the enhanced decadal predictability of the AMOC fingerprint - the dipole UOHC anomaly in the extra-tropical North Atlantic.

3.2 Descriptions of Model and Experiments

To investigate the evolution of the AMOC fingerprint, we conducted two sets of experiments using a fully coupled ocean-atmosphere model GFDL CM2.1 (*Delworth et al.*, 2006). The first set of experiments includes an ensemble of 10-member "Control" experiments and an ensemble of 10-member "Perturbed" experiments; both are integrated for 15 years. Each ensemble member of the "control" experiments employs a constant radiative forcing corresponding to the level of year 1860 and has a different initial condition 50 years apart from each other in CM2.1 control simulation. Each ensemble member of the "perturbed" experiments has the same constant radiative forcing and the same initial condition as the corresponding member of the control experiments, except that a positive salinity anomaly (0.5 PSU) is added to the upper 500m of the northern North Atlantic and the Nordic Sea in its initial ocean condition.

The second set of experiments is exactly the same as the first set, except that the temperature and salinity below 2200m in a subdomain of the subpolar North Atlantic (50°N – 60°N, 50°W – 30°W, blue box in Figure 3.1) are fixed as the initial values in all experiments. This prevents the AMOC anomaly from propagating southward in the deep ocean. In this set, the control and perturbed experiments are referred to as "Control_F" and "Perturbed_F", respectively. The anomaly for each of the two sets of experiments is defined as the ensemble mean difference

between the perturbed and the control experiments, i.e. “Perturbed - Control” and “Perturbed_F - Control_F”, respectively. Here the AMOC index at each latitude is defined as the maximum of the zonally integrated Atlantic meridional overturning streamfunction in density space. The AMOC fingerprint in this paper refers to the leading Empirical Orthogonal Function (EOF) of the extra-tropical North Atlantic UOHC (0-700m), similar to that shown in *Zhang* (2008). To compare with the results obtained from the above two sets of experiments, we also performed similar analyses from a 1000-year segment of GFDL CM2.1 control simulation that employs a constant radiative forcing at the level of year 1860 (*Delworth et al.,* 2006).

3.3 Evolution of the AMOC Fingerprint

For the first set of experiments, the initial positive salinity anomaly triggers an abrupt increase in the mixed layer depth (MLD) in the Labrador Sea and the Nordic Sea, and a positive AMOC anomaly at northern high latitudes which propagates southward (Figure 3.2a). It takes about 4 years for the AMOC anomaly to propagate from 55°N to 34°N with the slow advection speed along interior pathway of NADW, as shown in *Zhang* (2010). South of 34°N, the AMOC anomaly propagates southward confined to the coast with a rapid coastal Kelvin wave speed. Figure 3.3 shows the anomalous deep transport propagates from 34^{o}N to the equator along the western boundary within 1 year, a typical signature of the fast coastal Kelvin wave response (*Kawase,* 1987; *Johnson and Marshall*, 2002; *Zhang,* 2010).

The positive AMOC anomaly induces a positive anomaly in the zonally integrated Atlantic meridional heat transport (MHT) (Figure 3.2c) which propagates southward in a similar way as the AMOC anomaly. The tilt of the positive MHT anomaly with respect to time due to the slow advection speed north of 34°N implies the time lag of the MHT between different latitudes,

which leads to a meridional convergence of the MHT anomaly ($-\nabla \cdot MHT' > 0$) in the subpolar region and a meridional divergence of the MHT anomaly ($-\nabla \cdot MHT' < 0$) in the lower latitudes around 40°N, which reach their maxima at around year 5 (Figure 3.2e). The convergence of the MHT anomaly in the subpolar region propagates southward, gradually replacing the divergence of the MHT anomaly in the lower latitudes around 40°N (Figure 3.2e). Such convergence and divergence of the MHT induce a positive anomaly in the UOHC (warming) in the subpolar region and a negative anomaly in the UOHC (cooling) in the lower latitudes around 40°N (Figure 3.2g), so that the UOHC anomalies peak at about year 7 - 8. The meridional convergence/divergence of the MHT anomaly and the associated UOHC anomaly are much weaker south of 34°N due to the rapid coastal wave speed of the AMOC and MHT (Figure 3.2e, g).

For the second set of experiments, the initial positive salinity anomaly triggers a similar abrupt increase in the MLD in the Labrador Sea and the Nordic Sea and a positive AMOC anomaly at northern high latitudes initially. However, the positive AMOC anomaly at northern high latitudes cannot propagate southward due to the fixed deep ocean temperature and salinity in the subdomain (Figure 3.2b). Consequently, there is no southward propagation of the MHT anomaly from 55°N to 34°N, no obvious convergence (divergence) of the MHT anomaly and no associated warming (cooling) anomaly in the subpolar region (lower latitudes) (Figure 3.2d, f, h).

The anomaly in the Atlantic UOHC found in the first set of experiments (Figure 3.2g) corresponds to a distinctive spatial dipole pattern in the leading mode (EOF1) of the extra-tropical North Atlantic UOHC anomaly (perturbed - control), with warming in the SPG and cooling in the GS region around 40°N (Figure 3.4a). Previous studies (*Zhang*, 2007; *Wang and Zhang,* 2013) showed that a positive AMOC anomaly can induce surface warming and anti-

correlated subsurface cooling, especially in the subtropical/tropical North Atlantic. The negative UOHC anomaly in the GS region is associated with a southward shift of the GS path and is subducted southward along the isopycnals contributing to the subsurface cooling in the subtropical/tropical North Atlantic. Figure 3.4c shows the time evolution of this AMOC fingerprint, i.e. the principle component of this leading mode (PC1) in the UOHC anomaly starts to increase around year 2 until it reaches a maximum around year 8, and then decreases afterwards. There is no such dipole pattern in the EOF1 of the extra-tropical North Atlantic UOHC anomaly (Figure 3.4b, d) in the second set of experiments (perturbed_F - control_F), since the AMOC anomaly southward propagation is blocked by the fixed deep ocean temperature and salinity in the subpolar region.

3.4 Decadal Predictability of the Dipole UOHC Anomaly in the SPG/GS region

To study the decadal predictability of the dipole UOHC anomaly in the SPG and in the GS region, we look into the ensemble mean UOHC anomalies averaged over the SPG and over the GS region (black boxes in Figure 3.4a, b) respectively in the two sets of experiments. The ensemble mean UOHC anomalies averaged over the SPG and over the GS region (thick red/blue lines) are predictable if they are distinguishable from the 95% *t*-test range (i.e. outside of the gray shading areas) in Figure 3.4 e, f, g, h, following the method used in previous studies (*Hermanson and Sutton,* 2009; *Haines* et al., 2009).

For the first set of experiments, the ensemble mean UOHC anomaly averaged over the SPG exhibits a predictable warming signal from year 4 to year 13, for about 9 years with a peak around year 8 (Figure 3.4e); meanwhile the ensemble mean UOHC anomaly averaged over the GS region shows a predictable cooling from year 4 to year 12, for about 8 years with a peak

around year 7 (Figure 3.4g). The period of predictability is slightly shorter for the GS region, because the MHT divergence there is replaced by the convergence anomaly that propagates southward from the SPG (Figure 3.2e).

For the second set of experiments, the ensemble mean UOHC anomalies averaged over the SPG and over the GS region are not predictable for nearly the entire period (Figure 3.4f, h), because the initial AMOC anomaly at northern high latitudes cannot propagate southward. This experiment confirms that the decadal predictability of the UOHC anomalies in the SPG and in the GS region is owing to the slow southward propagation of the AMOC anomaly from 55°N to 34°N.

3.5 Mechanism for the Evolution of the AMOC Fingerprint

Figure 3.5 illustrates the physical mechanism for the evolution of the AMOC fingerprint. The positive MHT anomaly (solid red line) induced by a positive AMOC anomaly slowly propagates southward along with interior pathways from 55°N to 34°N and then continues with a fast coastal wave speed south of 34°N. The zero contours of the MHT anomaly are indicated by the dotted grey lines. From 55°N to 34°N, the slow propagation of the positive MHT anomaly leads to an anomalous heat convergence ($-\nabla \cdot MHT' > 0$) north of the MHT anomaly and an anomalous heat divergence ($-\nabla \cdot MHT' < 0$) south of it. The time integral of the heat convergence/divergence pattern gives rise to the dipole UOHC anomaly, warming in the SPG and cooling in the GS region several years later. The divergence of the MHT anomaly is confined within a narrower latitude range from around 43°N to 34°N than that of the convergence from 55°N to 43°N. For a weakening AMOC, we would expect an anomalous heat divergence in the north and an anomalous heat convergence in the south, cooling in the SPG and

warming in the GS region. South of 34°N, the more rapid propagation speed inhibits the convergence and divergence patterns and therefore the UOHC anomalies.

To confirm that the AMOC travels from the SPG to the GS region along an interior pathway, we examined oxygen concentration as a sensitive tracer for deep circulation changes (*Brennan et al.,* 2008) since the oxygen concentration in the deep ocean is barely affected by biological processes. The ocean component in the GFDL ESM2M earth system model has similar dynamics to the GFDL CM 2.1 model. In a 500-year control simulation from GFDL ESM2M we calculated the correlation of the AMOC anomaly at 50°N with the AMOC anomaly at different latitudes (Figure 3.6a), as well as with the zonally integrated oxygen concentration anomaly (2000m-3000m) (Figure 3.6b). The correlation of the AMOC anomaly in this 500-year control simulation shows a similar propagation pattern to that in the first set of experiments (perturbed – control) in GFDL CM2.1 (Figure 3.2a). The oxygen propagation (Figure 3.6b) suggests that the southward advection of deep water from the SPG to the GS region takes 4-5 years. This is consistent with the travel time for the AMOC from SPG to the GS.

The correlation analyses from the 1000-year segment of GFDL CM2.1 control simulation (Figure 3.7) also show similar propagation patterns to those in the first set of experiments (perturbed - control) in Figure 3.2. Linkages are enhanced in 10-year low-pass filtered anomalies (Figure 3.8), suggesting that the mechanism occurs primarily at the decadal time scale and beyond. The spatial dipole anomaly in the SPG/GS region in EOF1 of the extra-tropical North Atlantic UOHC anomaly in GFDL CM2.1 control simulation (Figure 3.9a) is similar to that in Figure 3.4a. Figure 3.10b and c show the averaged UOHC anomalies in the SPG/GS box explained by EOF1 of UOHC anomaly, which are exactly in-phase/anti-phase with PC1 of UOHC anomaly (Figure 3.10a) and have standard deviations as twice as those of the noise

(signals other than the EOF1), implying that the EOF1 for the box-averaged UOHC anomalies is dominant in the total box-averaged UOHC anomalies.

The AMOC amplitude in the 1000-year control simulation is smaller than that in our perturbed-control experiments, therefore it is necessary to demonstrate that the PC1 and box averaged UOHC in this 1000-year control simulation stand out of the noise. We sampled two ensembles ("positive AMOC" ensemble and "negative AMOC" ensemble) from the 1000-year segment of the control simulation. The AMOC anomaly at 50°N in the control simulation has a standard deviation (σ) of 2.4Sv. Whenever a peak (trough) AMOC anomaly at 50°N falls within plus (minus) 1.7~2.2σ (for the extreme events), we labeled the corresponding year as year 0 and sampled 4 years before and 10 years after year 0 as one member for the "positive AMOC" ("negative AMOC") ensemble. Over the 1000-year segment, we were able to sample a maximum of 18 members for both ensembles and defined the "anomaly" as the differences between the two ensembles. Time evolution of AMOC anomaly, MHT anomaly, convergence of MHT anomaly, and zonally integrated UOHC anomaly in the North Atlantic sampled from the control simulation (Figure 3.11) have similar patterns to those in the first set of experiments (perturbed – control) (Figure 3.2, left), but with weaker amplitudes. Moreover, the EOF1 and PC1 of the ensemble mean UOHC anomaly sampled from the control simulation (Figure 3.12a,b) also shows a similar dipole pattern and time evolution of the AMOC fingerprint as the first set of experiments (Figure 3.4a,c). The ensemble mean UOHC anomaly averaged over the SPG/GS box exhibits a predictable (i.e. outside the 95% *t*-test range) warming/cooling signal from year 0 to year 6 (Figure12c,d), similar to the first set of experiments (Figure 3.4e,g) except that the amplitudes of anomalies in the control simulation are smaller. This agreement indicates the robustness of the physical mechanism for the evolution of the AMOC fingerprint.

In GFDL CM2.1 control simulation, the low-frequency AMOC variability is strongly affected by the variability in the MLD in the Labrador Sea, as deeper mixed layer in the Labrador Sea is associated with stronger NADW formation (*Zhang,* 2010). The MLD anomaly in the Labrador Sea leads the AMOC anomaly at 50°N by about 2 years and leads the AMOC anomalies south of 34°N by about 6-7 years (Figure 3.9b). The AMOC anomaly at 50°N leads the PC1 of the UOHC anomaly by about 2-3 years, while the MLD anomaly in the Labrador Sea leads the UOHC PC1 by 5 years (Figure 3.9c).

3.6 Conclusion and Discussion

The modeling results here suggest that the southward propagation of the AMOC/MHT anomaly is the key mechanism that gives rise to the distinctive dipole UOHC anomaly in the North Atlantic (i.e. the AMOC fingerprint) and is responsible for the predictability of this dipole UOHC anomaly at decadal timescale. The southward propagation of a positive AMOC/MHT anomaly from 55°N to 34°N with the slow tracer advection speed leads to a convergence of the MHT anomaly in the SPG region and a divergence of the MHT anomaly in the GS region respectively, thus causing higher UOHC in the SPG and lower UOHC in the GS region several years later. This process is mainly confined to north of 34°N, because south of 34°N the AMOC/MHT anomaly moves more rapidly inhibiting the UOHC convergences associated with the MHT anomaly.

The AMOC anomaly at northern high latitudes in both sets of experiments is triggered in the models by a salinity anomaly. However, without the southward propagation of the AMOC anomaly, such as in the second set of experiments, there is no southward propagation of MHT anomaly, thus no convergence/divergence of the MHT anomaly. Two sets of experiments

suggested that predictable temperature signals in the SPG and the GS region depend on the southward propagation of the AMOC/MHT anomaly. The AMOC anomaly at northern high latitudes can also be triggered by factors other than salinity, such as changes in surface buoyancy forcing and NADW formation.

Similar meridional coherence and southward propagation of the AMOC anomalies also appear in other climate models, such as in GFDL CM2M (z-coordinate) and CM2G (isopycnal-coordinate) (*Wang et al.,* 2015), as well as in high resolution global coupled models GFDL CM2.5 (*Zhang et al.,* 2011) and UK HiGEM (*Matthew Thomas*, personal communication). These different climate models show similar critical latitudes around 34°N where the two propagation regimes differ, probably because the latitude where the interior pathways converge back to the western boundary is controlled by the ocean bathymetry. This latitude coincides with the latitude of the GS separation near Cape Hatteras, and their linkages deserve more future investigations.

Our results provide a physical mechanism for the decadal prediction skill in the UOHC in the SPG shown in recent studies (*Robson et al*., 2012; *Yeager et al.,* 2012; *Yang et al.,* 2013; *Msadek et al.,* 2014), i.e. initializing a stronger AMOC at northern high latitudes leads to successful predictions of the warming of the SPG in the mid 1990s. However, the cooling in the GS region is less visible in these prediction experiments, as the warming induced by anthropogenic radiative forcing is also included in these experiments and because the UOHC anomaly in the GS region has a shorter predictable time scale. The physical mechanism discussed in this paper is also consistent with the recent work by *Robson et al.* (2014) showing that initializing a weaker AMOC at northern high latitudes leads to a successful prediction of the cooling in the SPG in the 1960's; they also predicted the warming in the GS region.

Previous studies show that low frequency AMOC variability is associated with the AMO, an SST anomaly spanning the SPG and the subtropical/tropical North Atlantic (*Knight et al.,* 2005; *Ting et al.,* 2009; *Zhang and Wang*, 2013; *Ba et al.,* 2014). Our results suggest that the direct effect of the AMOC induced anomalous ocean heat transport convergence/divergence on the UOHC anomaly is mainly confined to north of 34°N. Some other mechanisms, other than direct changes in the ocean heat transport convergence, must link the AMOC anomaly at northern high latitudes with the SST anomaly in the subtropical/tropical North Atlantic. The subtropical/tropical SST anomaly is more likely part of a coupled ocean-atmosphere processes, such as the AMOC induced intertropical convergence zone (ITCZ) shifts, changes in the Hadley circulation and trade wind (*Zhang and Delworth*, 2005; *Kang et al.*, 2008; *Frierson et al*., 2013; *Robson et al.,* 2014), the wind-evaporation-SST (WES) feedback (*Xie and Philander*, 1994; *Mahajan et al.,* 2011), or changes in the NAO linked large-scale atmospheric response (*Hodson et al.,* 2014; *Omrani et al.,* 2014; *Robson et al.,* 2014). In addition, the AMOC induced SST anomaly at lower latitudes can be amplified by the cloud feedback (*Zhang et al.,* 2010) and the coupled feedback between SST, African dust, and Sahel rainfall (*Wang et al.,* 2012). The detailed mechanisms linking the AMOC anomaly at northern high latitudes with the SST anomaly in the subtropical/tropical North Atlantic deserve more investigations in future studies.

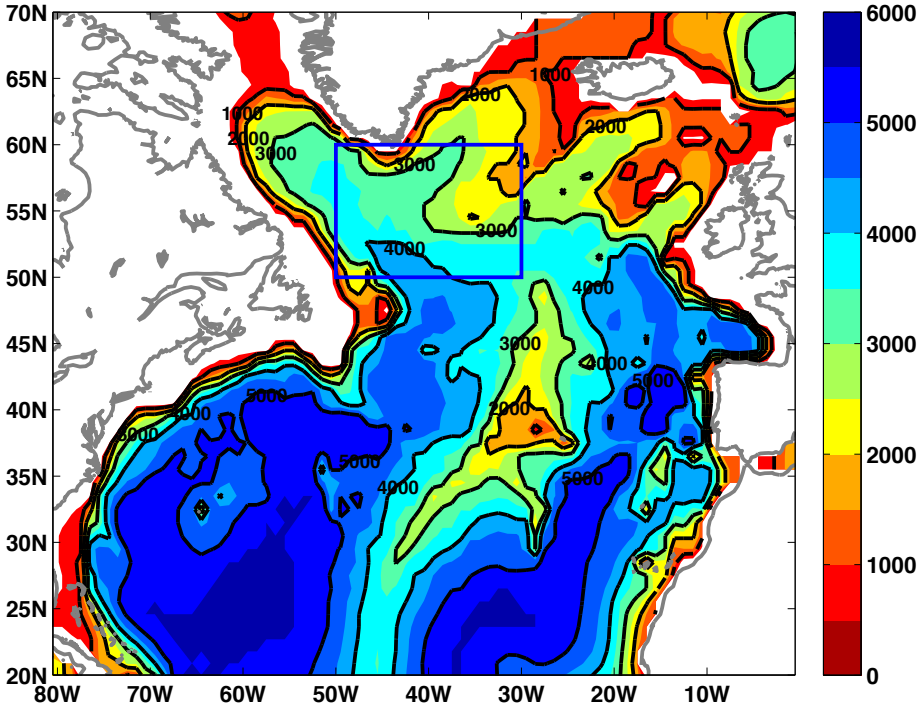

Figure 3.1 North Atlantic Ocean Bathymetry in GFDL CM2.1. The blue box represents the subpolar region with temperature and salinity below 2200m fixed as initial values in the second set of experiments.

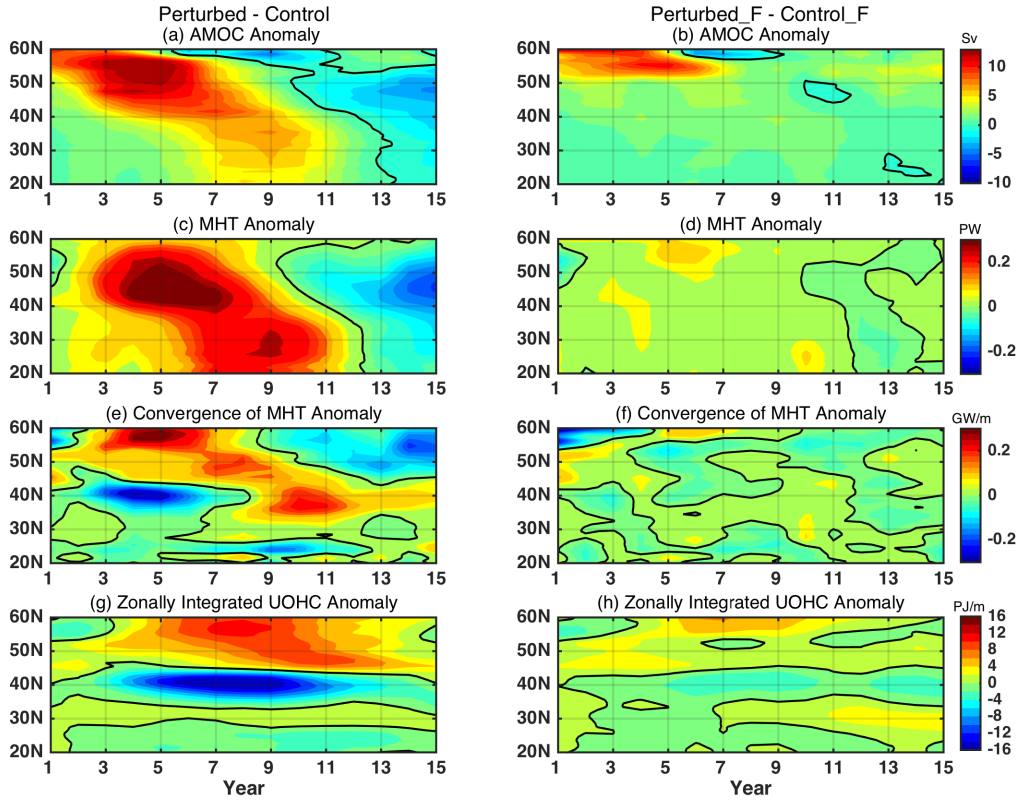

Figure 3.2 Time evolution of anomalies as a function of latitude (perturbed - control, left panels; perturbed_F - control_F, right panels). (a,b) AMOC anomaly (Sv), (c,d) MHT anomaly (PW), (e,f) Convergence of MHT anomaly ($-\nabla \cdot MHT'$, GW/m), (g,h) Zonally integrated UOHC anomaly in the North Atlantic (PJ/m). The black solid lines are zero contour lines.

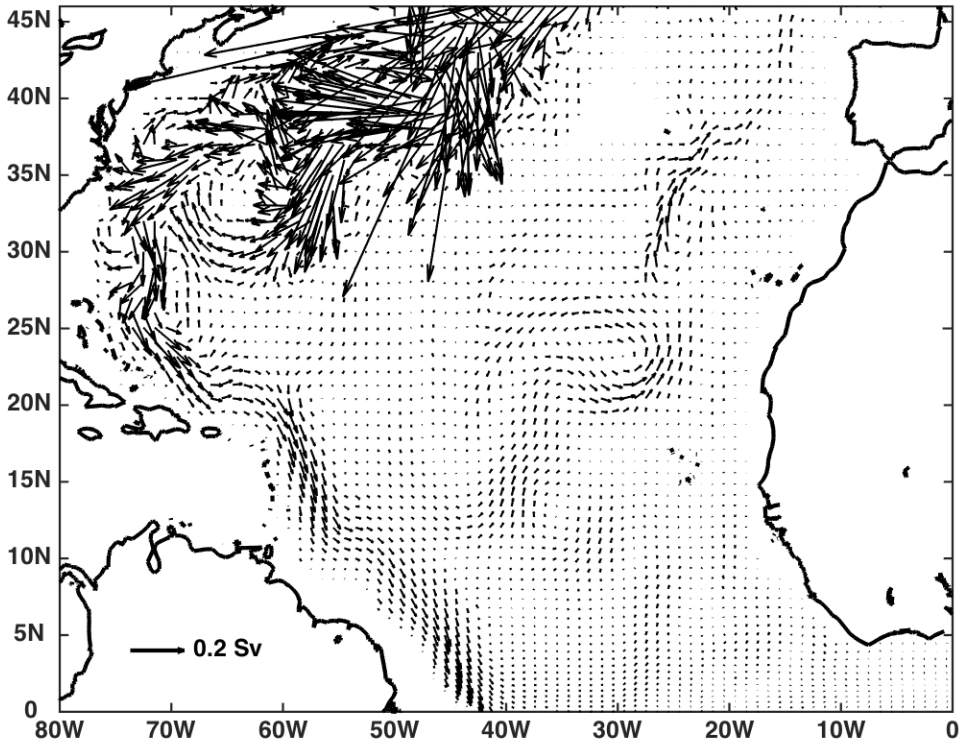

Figure 3.3 Deep transport anomaly at potential density level of 1036.9 kg/m^3 at year 1 in the first set of "perturbed - control" experiments.

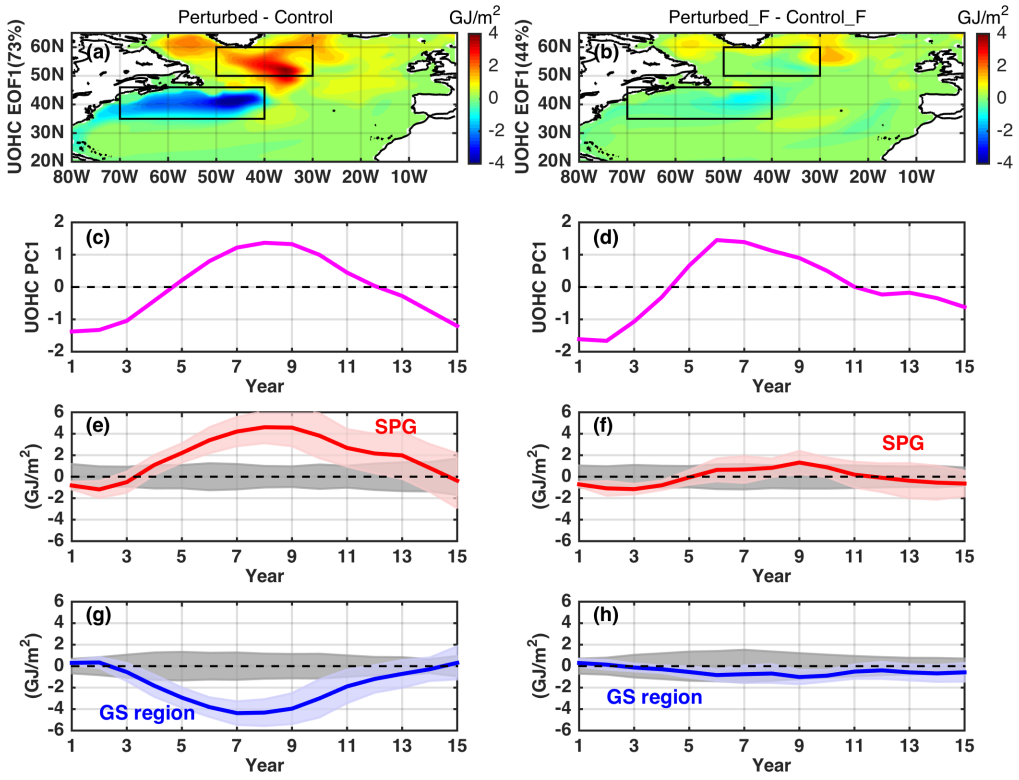

Figure 3.4 Spatial pattern and time evolution of the AMOC fingerprint (perturbed - control, left panels; perturbed_F - control_F, right panels). (a,b) EOF1 of ensemble mean UOHC anomaly, (c,d) PC1 of ensemble mean UOHC anomaly, (e,f,g,h) Averaged UOHC anomaly in the SPG box (50°N – 60°N, 50°W – 30°W) and the GS box (35°N – 46°N, 70°W – 40°W) respectively (solid red/blue lines). Light red/blue shading areas: spread (one standard deviation) among the 10 ensemble members. Grey shading area: 95% significance range.

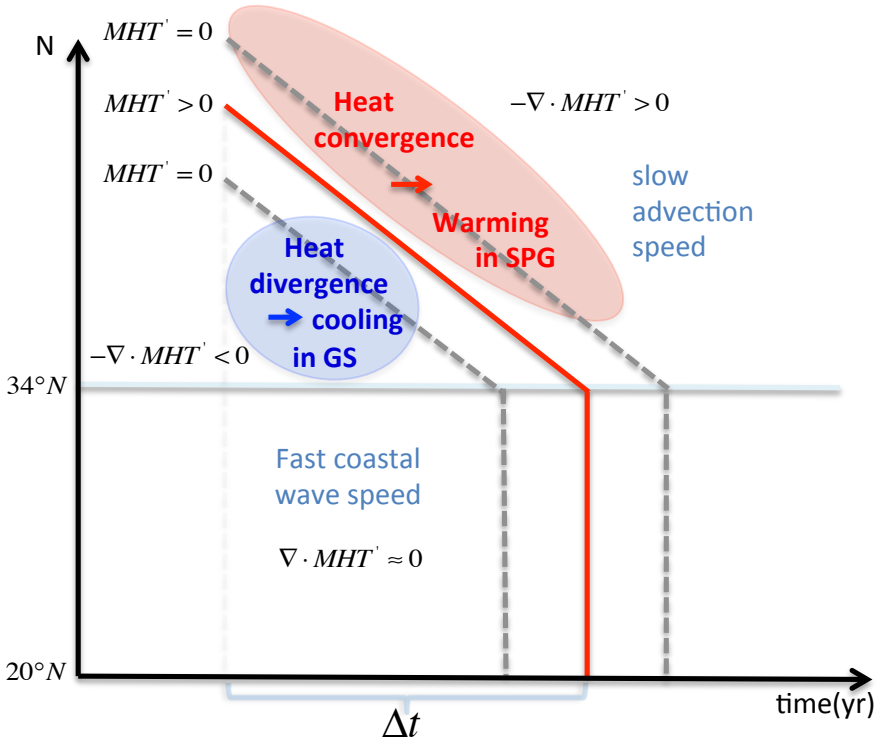

Figure 3.5 Schematic diagram for the physical mechanism of the evolution of the AMOC fingerprint.

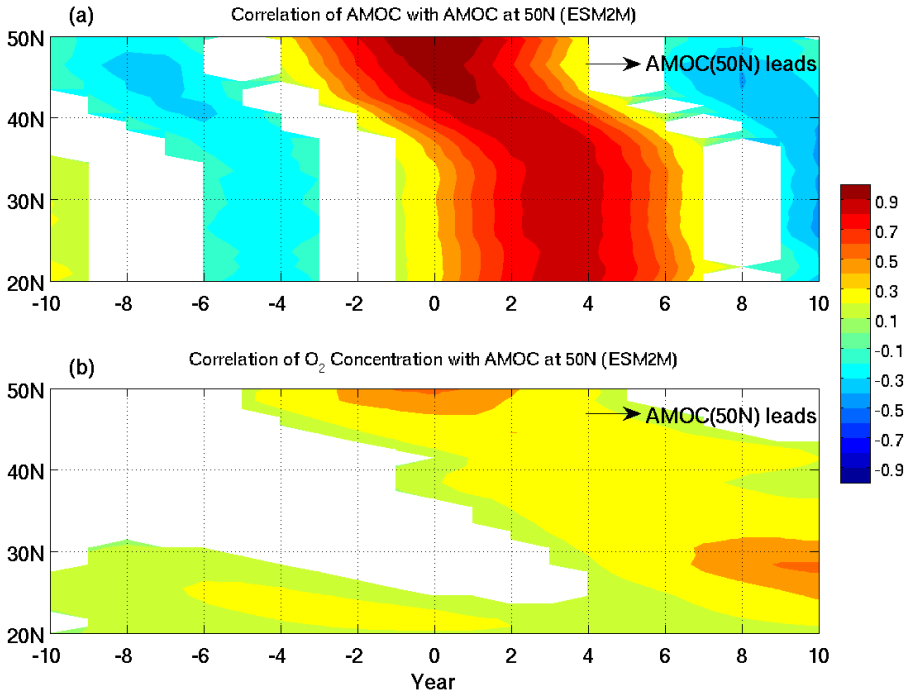

Figure 3.6 Correlations of (a) AMOC anomaly and (b) zonally integrated O_2 concentration anomaly between 2000m and 3000m with AMOC anomaly at 50°N in GFDL ESM2M 500-year control simulation. The shaded area is above 95% significance level.

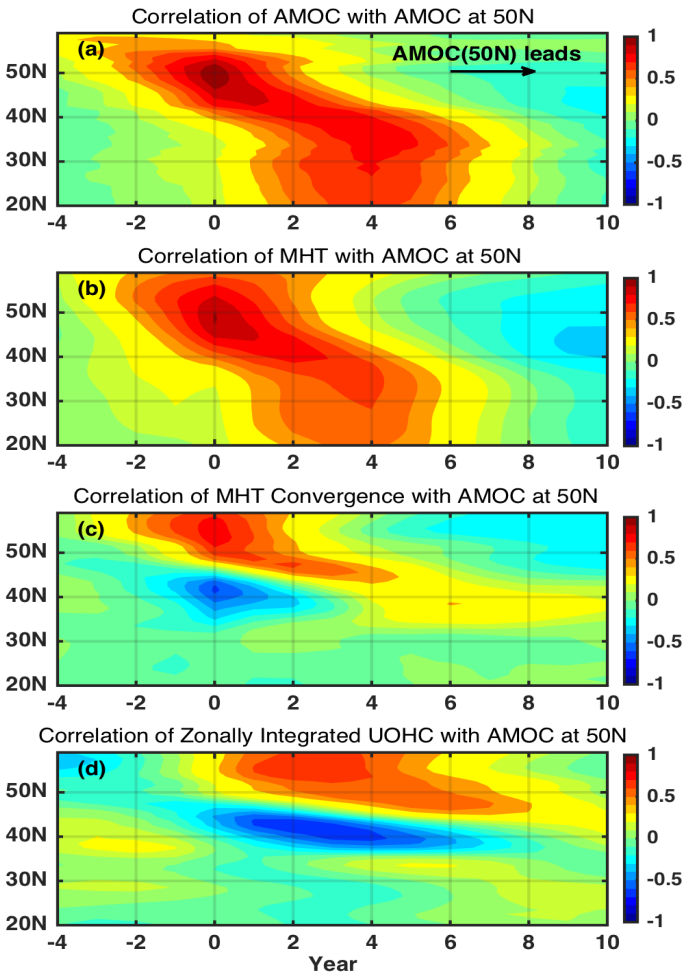

Figure 3.7 Cross correlations of AMOC anomaly at 50°N with AMOC anomaly (a), MHT anomaly (b), convergence of MHT anomaly ($-\nabla \cdot MHT'$) (c), and zonally integrated UOHC anomaly (d), respectively.

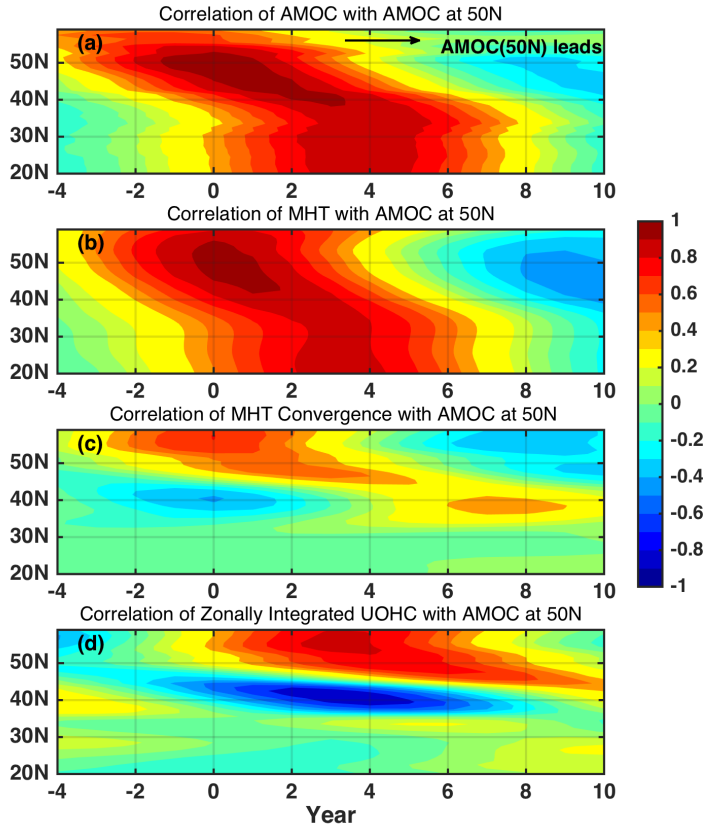

Figure 3.8 Low-pass filtered results from a 1000-year segment of the GFDL CM2.1 control simulation. Cross correlations of 10-year low-pass filtered AMOC anomaly at 50°N with 10-year low-pass filtered AMOC anomaly (a), MHT anomaly (b), convergence of MHT anomaly ($-\nabla \cdot MHT'$) (c), and zonally integrated UOHC anomaly (d) at different latitudes.

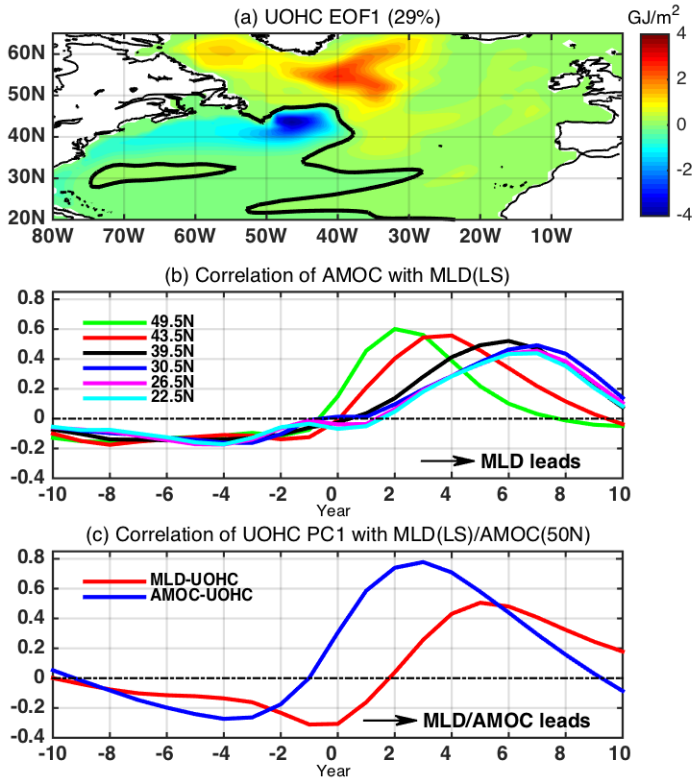

Figure 3.9 The AMOC fingerprint and its linkage with the Labrador Sea (LS) and Mixed Layer Depth (MLD) anomaly in the 1000-year segment of GFDL CM2.1 control simulation. (a) EOF1 of extra-tropical North Atlantic UOHC anomaly (explaining 29% of total variance), (b) Cross correlations of AMOC anomaly at different latitudes with the MLD anomaly in the LS, (c) Cross correlations of UOHC PC1 with the MLD anomaly in the LS (red) and with the AMOC anomaly at 50°N (blue), respectively. The solid black lines in (a) are zero contour lines.

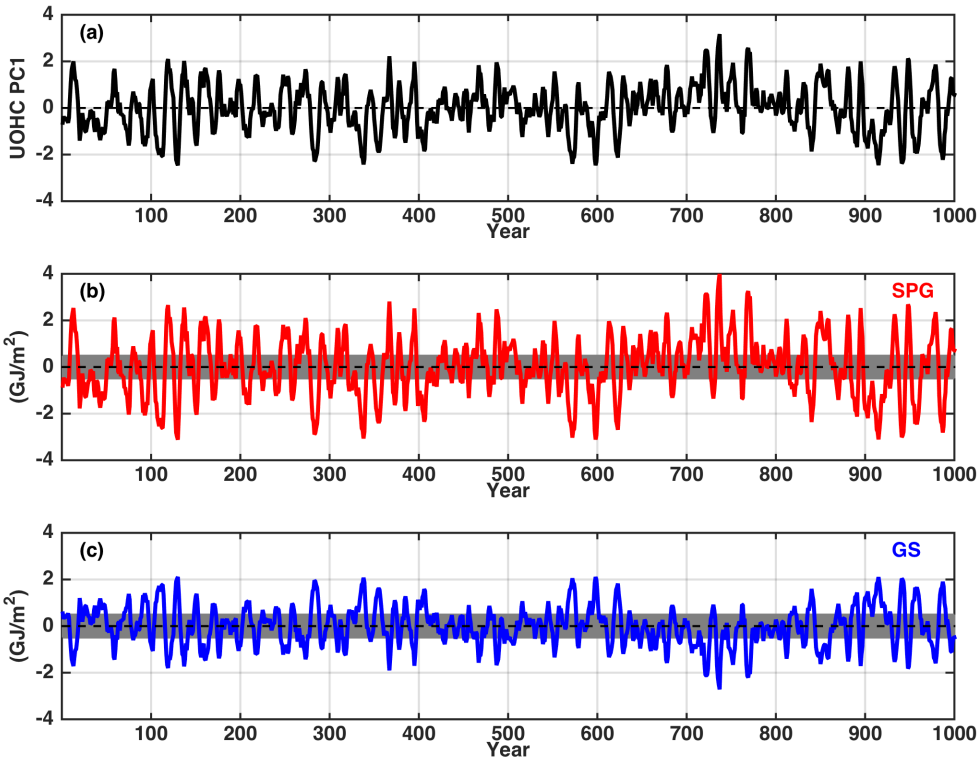

Figure 3.10 Box-averaged SPG/GS UOHC anomalies explained by EOF1 of UOHC anomaly in the GFDL CM2.1 1000-year control simulation. (a) Time series of the leading mode (PC1) of UOHC anomaly. (b) Box-averaged SPG UOHC anomaly explained by EOF1. (c) Box-averaged GS UOHC anomaly explained by EOF1. The gray shading areas in (b,c) represent the amplitudes (+/- 1 standard deviation) of the noise (i.e. the box-averaged SPG/GS UOHC anomalies not explained by EOF1).

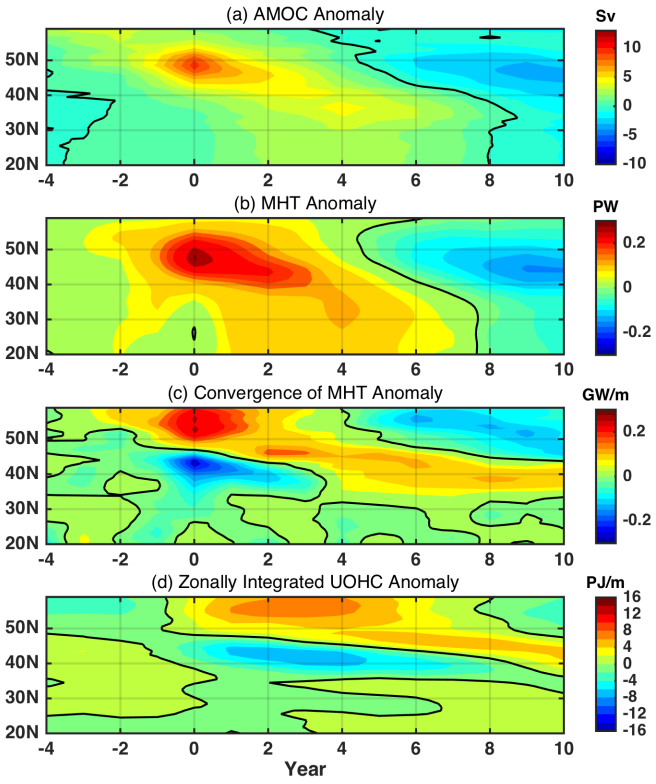

Figure 3.11 Time evolution of ensemble mean anomalies from eighteen 15-year ensemble members sampled from 1000-year control simulation as a function of latitude. (a) AMOC anomaly (Sv), (b) MHT anomaly (PW), (c) Convergence of MHT anomaly ($-\nabla \cdot MHT'$, GW/m), (d) Zonally integrated UOHC anomaly in the North Atlantic (PJ/m). The black solid lines are zero contour lines.

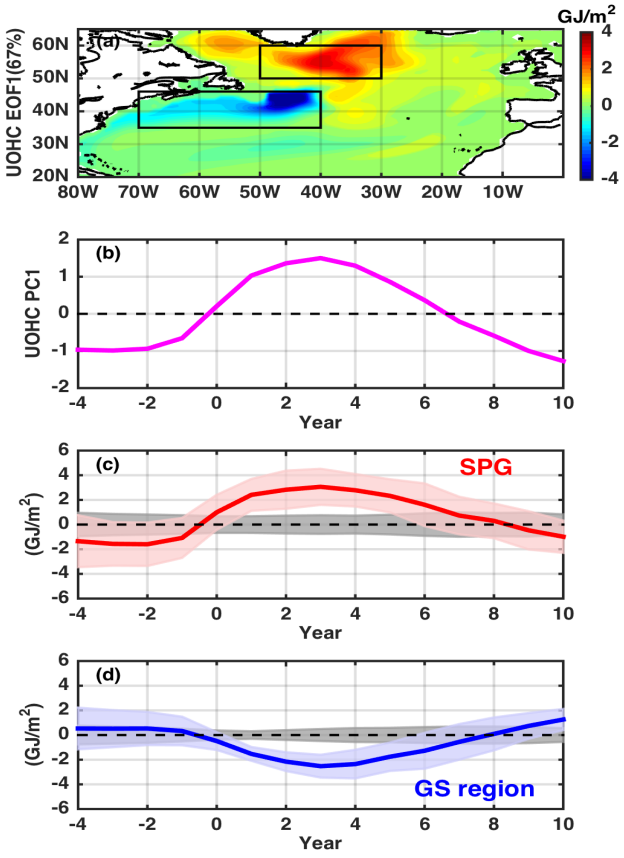

Figure 3.12 (a,b) EOF1 and PC1 of ensemble mean UOHC anomaly from eighteen 15-year ensemble members sampled from 1000-year control simulation. Averaged UOHC anomaly from the ensemble members in the SPG box (c) and the GS box (d) respectively (solid red/blue lines). Light red/blue shading areas: spread (one standard deviation) among the ten sampled ensemble members. Grey shading area: 95% significance range.

Chapter 4. THE COHERENCE OF ATLANTIC MERIDIONAL HEAT TRANSPORT IN CLIMATE MODELS

4.1 Introduction

The oceanic meridional overturning circulation and associated meridional heat transport (MHT) play an important role in the planetary heat budget. The Atlantic Meridional Overturning Circulation (AMOC) is composed of a northward flow of warm water in the upper ocean and a southward flow of cold water at depth (e.g. *Broecker* 1991; *Lumpkin and Speer* 2007; *Kuhlbrodt et al.* 2007). The Atlantic Ocean transports up to 1.3 PW heat to the north, and the heat transport is northward throughout the basin (*Hastenrath,* 1982; *Hsiung,* 1985; *Trenberth and Solomon* 1994; *Trenberth and Caron* 2001; *Wunsch,* 2005). In the tropics and subtropics, the ocean carries a significant fraction of the total heat transport of the atmosphere and ocean combined. It reaches a maximum near 30°N and then drops rapidly near the latitude of the Gulf Stream (*Trenberth and Caron*, 2001; *Wunsch*, 2005), where the ocean releases a large amount of heat to the atmosphere. The atmospheric heat transport dominates further to the North. Previous studies have suggested that changes in AMOC and MHT could impact the extent of Arctic Sea Ice (*Rind and Chandler*, 1991), atmospheric circulation (*Cohen-Solal and Le Treut*, 1997), sea surface temperature (SST) over the North Atlantic and tropical South Atlantic (*Dong and Sutton*, 2002), tropical Atlantic Variability (TAV) (*Wen et al.,* 2011), as well as the location of the Atlantic Intertropical Convergence Zone (ITCZ) (*Frierson et al.,* 2013).

Changes in MHT in the Atlantic have been shown to be closely linked to AMOC. *Dong et al.* (2009) use observations to show that a MHT anomaly of 0.05 PW ($1\ PW = 10^{15} Watts$) is found for each Sv ($1\ Sv = 10^{6} m^{3}/s$) of AMOC change at 34°S. Likewise, *Msadek et al.* (2013)

found a linear relationship between observationally derived mass and heat transport at 26.5°N with $0.079\,PW/Sv$. *Zheng and Giese* (2009) showed that the increases of northward heat transport (up to 25% in the midlatitudes) in the Atlantic is coincident with the simultaneous increase of the AMOC using the results of the Simple Ocean Data Assimilation (SODA) analysis. In a sensitivity study using a coupled climate model in the Chapter 4 of this thesis, a strengthening of AMOC in the subpolar gyre leads to a convergence/divergence of the MHT anomaly in the subpolar/Gulf Stream region several years later.

However, the connection between AMOC and MHT may be more nuanced than the studies reviewed in the previous paragraph suggested. *Boccaletti et al.* (2005) derived a heat transport stream function to show that the maximum of this streamfunction is 700m or above, with the maximum located at less than 200m between the equator and 35°N. In contrast, the maximum of the mass transport streamfunction is at about 1000m between 40°N and 60°N. This suggests that MHT in the tropics and subtropics is more sensitive to variations in the upper ocean circulation than AMOC, while the AMOC is likely more sensitive to changes in deep and intermediate water transport, which is controlled by processes in the high latitude upper ocean and is impacted by changes in the atmosphere there. Modeling studies suggest that AMOC in the subpolar region varies on decadal time scales and responds to low frequency changes in wind or buoyancy forcing (e.g. *Bingham et al.*, 2007; *Zhang,* 2010); the state of the AMOC at high latitudes could be used to improve decadal prediction of climate (*Persechino et al.*, 2013; *Msadek et al.*, 2010; *Tulloch and Marshall*, 2012; *Latif et al.*, 2004; *Knight et al.*, 2005; *Zhang*, 2007, 2008, 2010).

Interannual variability of MHT and AMOC prevails equatorward of 40°N (*Zheng and Giese,* 2009; *Kelly et al.,* 2014; *Jayne and Marotzke,* 2001; *Bingham et al.,* 2007; *Zhang*, 2010). *Kelly et al.* (2014) explored the interannual-to-decadal MHT anomalies inferred from hydrographic data,

equivalent water thickness and altimetric sea surface height and showed that the MHT anomalies are highly coherent from 35°S to 40°N. *Jayne and Marotzke* (2001) also showed the strong seasonal and interannual MHT coherence within 20° of the equator in a 1/4° ocean model. Similar coherence structure has also been seen in AMOC in the North Atlantic from about 20°S to 30°N using modeling studies (*Bingham et al.*, 2007; *Zhang*, 2010). These studies suggest that the meridional coherence of both AMOC and MHT at the interannual timescale is a robust feature.

In the present study we use a global ocean-only model (the isopycnal ocean model GOLD, Generalized Ocean Layer Dynamics) run with hindcast forcing from 1971 to 2009 and seven CMIP5 (Coupled Model Intercomparison Project Phase 5) coupled models from 1971 to 2005 to examine the meridional structure of the interannual MHT variability. In addition, we perform detailed analysis of the linkage between MHT variability and atmospheric forcing using GOLD. This paper is organized as follows. The data and model descriptions are presented in section 2. We then discuss the meridional structure of the interannual MHT variability in the tropics/subtropics in section 3 and then examine the linkages between the MHT variability, atmospheric forcing, circulation, and density fields in section 4.

4.2 Data and Models

To diagnose the structure of the interannual MHT, we analyze both an ocean-only simulation (GOLD) and the MHT from a suite of coupled model simulations taken from the CMIP5 archive. In order to determine the validity of GOLD, two observationally derived estimates of MHT are also used for comparison.

4.2.1 Data: Estimates of MHT in the North Atlantic

Observational estimates of MHT are available at 26.5°N and 41°N in the Atlantic from two different methods.

4.2.1.1 RAPID-MOCHA at 26.5°N

The RAPID-MOCHA (Rapid Climate Change - Meridional Overturning Circulation and Heatflux Array) mooring array is a collaborative project between the United Kingdom and the United States, to measure the AMOC and MHT in the North Atlantic Ocean (*Cunningham et al.,* 2007; *Kanzow et al.,* 2007; *Kanzow et al.,* 2008). Twenty-four moorings have been deployed at 26.5°N since April 2004, where the mean ocean heat transport reaches its maximum at about 1.3 PW (*Johns et al.,* 2011). Three groups of moorings are concentrated at the western Atlantic basin for Western Boundary Current, the eastern side of the Atlantic basin, and the Mid-Atlantic Ridge, respectively. These are combined with underwater cable estimates of the Florida Current transport. The MHT is derived by combining temperature transports from the Florida Current, the western boundary region offshore of the Bahamas, the Ekman transport from wind stresses and the interior ocean portion from the geostrophic transport calculated by the difference of dynamic heights between moorings (*Johns et al.,* 2011). We compare the MHT from RAPID-MOCHA during 2004-2009 with the hindcast run in GOLD in the same period.

4.2.1.2 Sea Surface Height (SSH) and Argo derived AMOC at 41°N

An alternate estimate of the AMOC at 41°N was calculated from a combination of altimetric and Argo data (*Willis*, 2010; *Willis and Fu*, 2008; *Hobbs and Willis*, 2012). To do this, a monthly time series of density from the surface to 2000m is derived from Argo data to produce geostrophic velocity in the upper 2000 m. The geostrophic velocity estimate combined with high-resolution SSH data from altimeters are used to reduce error induced by mesoscale eddies.

The AMOC is then calculated by integrating from the surface to 1130m together with the Ekman transport computed from wind stress. The SSH data and its relationship to AMOC during the Argo time period is used to extend the time series back to 1993. All points in the time series represent 3-month running averages. We download both SSH derived AMOC and SSH/Argo derived AMOC, but just compare the AMOC from GOLD with the SSH derived AMOC at 41°N from 1993 to 2009.

4.2.2 Methods and Models

4.2.2.1 GOLD

GOLD is a generalized Lagrangian-coordinate isopycnal ocean model (*Adcroft and Hallberg*, 2006), following in the lineage of the Hallberg Isopycnal Model. It was released in September 2012. The two mixed layers, two buffer layers, and fifty-nine isopycnal layers with constant potential densities referenced to 2000m, are chosen to provide the highest resolution of thermocline. It has $1° \times 1°$ horizontal resolution but with 0.5° in latitudes at tropics. Surface winds and buoyancy fluxes are from CORE-II (Coordinated Ocean-ice Reference Experiments Version 2) between 1971-2009 (*Large and Yeager,* 2009). We use a monthly averaged hindcast run of GOLD from 1971 to 2009 in this study, started after thousand years of spin-up.

We calculate the MHT through vertical cross-sections in GOLD. We assume the volume is conserved through each cross section at each latitude so that the MHT is given by

$$H = \iint \rho c_p \theta v dA \tag{4.1}$$

Where ρ , c_p , θ and v are potential density, specific heat capacity of seawater, potential temperature and meridional velocity. $dA = dxdz$ represents the integration over a vertical east-west section. For the Atlantic Ocean, the net transport from Atlantic Ocean to Southern Ocean is

less than 1 *Sv* (*Dong et al.,* 2011). Since GOLD is not a Boussinesq model, the ocean volume changes with additions/loss of fresh water. The maximum mass transport to the South is about 1 *Sv* in the subpolar region, decreasing to a fraction of a Sverdrup at the equator, consistent with the loss of fresh water via evaporation in the subtropics. We also calculate temperature transport, which is equal to the quantity in (4.1) when mass is not conserved (*Talley,* 2003).

4.2.2.2 A suite of coupled model simulations via CMIP5

CMIP5 provides a framework for coordinated climate change experiments (*Taylor et al.,* 2012). We use the ensemble-mean of northward heat transport in historical simulations from seven models in different modeling centers (Table 4.1) during 1971-2005 to examine the robustness of the variability of the interannual MHT anomaly. For example, MRI-CGCM3 is a coupled atmosphere-ocean global climate model (*Yukimoto et al.,* 2012) with horizontal resolutions of 1° × 0.5° with 50 vertical levels plus a bottom boundary layer, comparable to the resolution of GOLD. The surface layer is 4 m thick, and the upper layers above 1000 m are resolved by 30 layers. Other models in this set have similar resolution.

Table 4.1 Summary for CMIP5 models used in this study

Model	Institute	# Members*
ACCESS1-0	CSIRO	2
MRI-CGCM3	MRI	5
NorESM1-M	NCC	3
INMCM4	INM	1
GFDL-CM3	NOAA-GFDL	5
GFDL-ESM2G	NOAA-GFDL	1
GISS-ES-R-CC	NASA-GISS	1

* # Members is the number of ensemble members in the historical run for each model

4.3 Coherence structure of interannual MHT

In this section, we examine the characteristics of meridional structure of the interannual MHT in GOLD and in the CMIP5 models. The variability in Atlantic MHT is controlled by a variety of processes, including both changes in wind forcing throughout the basin as well as changes in buoyancy forcing in the subpolar North Atlantic. Using the monthly averaged fields we first remove the annual cycle, then lowpass the remaining variability in the MHT anomaly using a 1-year Butterworth lowpass filter, and remove the long-term linear trend. A comparison of interannual MHT from GOLD and two climate models, one with strong MHT variability, and another with weak variability shows that the MHT has a significant amount of coherence from about 20°S to about 30°N (Figure 4.1). Generally at low latitudes south of 40°N, interannual variability dominates and is much stronger than the decadal variability; whereas at high latitudes north of 40°N the decadal variability is more important, but much weaker than the interannual variability at low latitudes, consistent with the results from other studies derived from ocean models and observations (*Zheng and Giese,* 2009; *Kelly et al.,* 2014; *Jayne and Marotzke,* 2001). However, the magnitude of interannual MHT variability varies between models. For example, the interannual MHT in GISS-E2-R-CC ranges from -0.4 PW to 0.38 PW with a maximum standard deviation of 0.13PW, whereas the MHT in MRI-CGCM3 is in a range between -0.25 PW and 0.16 PW with a maximum standard deviation of 0.05PW, much smaller than that form GISS-E2-R-CC.

To better quantitatively define the interannual meridional coherence structure of the MHT anomaly, we apply empirical orthogonal function (EOF) analysis to all the lowpassed MHT anomalies from 30°S to 60°N in the CMIP5 coupled models and GOLD, but we just show the EOF results from 30°S-40°N due to near zero spatial pattern of EOF leading mode (EOF1) north

of 40°N. We find that the normalized EOF1 for the interannual MHT anomaly are remarkably consistent between CMIP5 coupled climate models and the ocean model GOLD; generally the MHT EOF1 has the same sign between 20°S - 35°N and with a maximum in the tropics, decaying towards the poles (Figure 4.2a). In this study, we use the leading mode of the interannual MHT variability as the meridional coherence structure for further investigation; EOF1 gives the spatial pattern and the first principal component (PC1) reveals the temporal variability. The CMIP5 models are from different institutions, thus they are relatively independent. Moreover, the fraction of variance explained by this EOF leading mode in all models is larger than 42%, which confirms the robustness of MHT coherence structure among the models. However, the meridional extent of the EOF1s depends on the different model simulations. For instance, the extent of the EOF1 in GOLD ranges from 20°S to 35°N (Figure 4.2a, red), while the EOF1 of MRI-CGCM3 (Figure 4.2a, Magenta) extends from 30°S to 35°N. The correlations between MHT anomaly on the equator with MHT at others latitudes also show that the interannual MHT between 20°S and 20°N is correlated with equatorial MHT for all the models (Figure 4.2b).

4.4 MHT and AMOC in GOLD

In this study we use GOLD simulation as our main tool to investigate the mechanism of the interannual MHT coherence structure. GOLD provides three dimensional spatial and temporal details of the ocean in density coordinates.

4.4.1 MHT and AMOC: comparison to observations

The total MHT from GOLD at 26.5°N (Figure 4.3a, black) is only 0.5-0.8 PW, about half size of that from the RAPID-MOCHA mooring (Figure 4.3a, red). The 1-year lowpassed

variability has a correlation of 0.71 with a 95% significant level of 0.45 (Figure 4.3b). The AMOC at 41°N derived from SSH alone (Figure 4.4a, red) is similar to that from both SSH and Argo floats from 2002 to 2009 at 41°N (Figure 4.4a, cyan), so we extend our comparison to 1993 using the AMOC derived from SSH alone. The mean AMOC (Figure 4.4a, black) at 41°N in GOLD is about 10-18.5 Sv, comparable with the SSH derived AMOC (Figure 4.4a, red). The correlation between the 1-year lowpassed AMOC anomalies in GOLD and from SSH at 41°N is 0.46 (95% significance level: 0.35). The mass and heat transports at 41°N are more difficult to accurately represent in a low-resolution model since it depends on the representation of the Gulf Stream and North Atlantic Current. Overall, GOLD adequately reproduces observed interannual MHT variability, allowing us to use it to understand what controls the interannual MHT in the tropics and subtropics.

4.4.2 Mean ocean circulation from GOLD

To understand interannual variability of the MHT in the Atlantic Ocean, we first consider zonally averaged time-mean potential density and temperature, MHT and AMOC between 30°S and 50°N for reference. The mixed layer depth ranges from 50 to 70m, while the thermocline depth ranges from below 300 m at 30°S and 30°N to 60 m at the equator (Figure 4.5).

We calculate the AMOC in density coordinates, the native coordinate of GOLD (Figure 4.6a). It is defined as the maximum of the vertical cumulative integral (starting at the surface) of zonally integrated meridional flow. *Zhang* (2010) argued that the maximum of AMOC in density space is shifted poleward to that calculated in depth space; She also argued that since water parcels move on density horizontals in the ocean, AMOC in density space more closely resembles the pathways of fluid parcels. The cumulative volume transport in the upper ocean above the isopycnal $1034.2 kg/m^3$ (mean depth 90m) is northward in the northern

tropics/subtropics, but southward in the upper South Atlantic Ocean. The opposing volume transport of the North Atlantic and South Atlantic are primarily caused by the opposing Ekman transport in the surface layer. Some of this Ekman transport is returned by geostrophic flow at depth (*Roemmich,* 1983; *Zhang et al.,* 2003). The volume transport is northward at depth, reflecting the northward flow of Antarctic Intermediate Water (AAIW), and southward North Atlantic Deep Water (NADW) near potential density 1037 kg/m^3 (*Roemmich,* 1983). The AMOC ranges between 10.7-13.6 Sv with the maximum occurring between 35°N and 40°N (Figure 4.6b).

The time-mean vertically cumulative (from the surface) heat transport (Figure 4.7a) has some similar features to the cumulative volume transport (Figure 4.6a). In density space, there are two maxima with values larger than 1 PW , one in the northern upper ocean near 15°N-20°N above 1034 kg/m^3 , the other one between 1036.5-1037 kg/m^3 near 20°N; the latter one cannot be seen significantly when calculated in depth space, as shown by *Boccaletti et al.* (2005). The latitude-dependent northward MHT from top to bottom in the Atlantic Ocean (Figure 4.7b) varies from 0.2 PW to 0.74 PW with a maximum near 20°N-30°N, smaller than the 1.3 PW found by the RAPID-MOCHA array at 26.5°N. The maximum of MHT occurs significantly south of the maximum of AMOC near 40°N. There is a dramatic increase near the equator and a large decrease north of 35°N. This is consistent with the large heat gain in the tropics and large heat release near the Gulf Stream, consistent with previous studies (*Zheng and Giese,* 2009; *Talley,* 2003; *Hall and Bryden,* 1982).

The interannual MHT anomaly is almost symmetric about the equator (Figure 4.2a), while the mean MHT is not (Figure 4.7b). This suggests that the dynamics that control the interannual

MHT variability are likely linked to the processes that control the shallow overturning circulation in the tropics.

4.4.3 Mechanism of MHT coherence in GOLD

4.4.3.1 Ekman and Geostrophic heat transport

We first examine the contributions of Ekman and geostrophic heat transports to the MHT leading mode in GOLD. The Ekman heat transport responds directly to changes in surface winds; it is defined as the zonal integral across a section from coast to coast (*Ghirardelli e al.,* 1995; *Levitus,* 1987):

$$H_{Ek} = -\int \frac{c_p \tau_x}{f}(\theta_{Ek} - \bar{\theta})dx \tag{4.2}$$

where H_{Ek} represents Ekman heat transport, f is the Coriolis parameter, τ_x is the zonal wind stress from CORE-II, θ_{Ek} is the potential temperature in the Ekman layer, $\bar{\theta}$ is the mean potential temperature of the water column in GOLD. The assumption of (4.2) is that the wind-driven Ekman mass transport is compensated by a barotropic return flow (*Ghirardelli e al.,* 1995; *Levitus,* 1987; *Jayne and Marotzke,* 2001; *Willebrand et al.,* 1980). Here, we estimate the Ekman layer temperature in (4.2) to be that of the upper 50 meters, similar to *Dong et al.* (2011). The Ekman heat transport is strong in the tropics due to strong trade winds, small values of Coriolis parameter and large difference between surface and deep ocean temperature, however, (4.2) cannot be applied within a few degrees of the equator (i.e. 3° north and south of the equator in this study) since f vanishes at the equator. We define the geostrophic heat transport as the difference between the total MHT and the Ekman heat transport (*Reommich,* 1983; *Dong et al.,* 2011; *Zhang et al.,* 2003). Similar to the interannual MHT anomaly, we also remove the annual cycle, lowpass the subannual variability and remove the long-term linear trend for both Ekman

and geostrophic heat transport. We ignore the bottom Ekman layer due to its small contribution to the MHT (*Perez el al.,* 2011).

The interannual MHT in GOLD is well represented with the EOF leading mode between 15°S and 30°N (compare Figure 4.8 a and b), accounting for 50% of the interannual MHT variance. South of 15°S and north of 30°N the coherence structure exists, but is weak. The magnitude of the Ekman heat transport dramatically decreases poleward within 10° of the equator; because of the vanishing Coriolis parameter toward the equator, both Ekman and geostrophic heat transport (Figure 4.8, c and d) are not available within 3° of the equator. For much of the times series, Ekman heat transport north of the equator looks similar to the EOF leading mode of the MHT (for instance, in 1988-1989, 1995 and 2005), but there are significant differences between the two fields south of the equator. The interannual geostrophic heat transport has opposite signs to the Ekman heat transport between 3°-10° on both sides of the equator. The EOF1s for Ekman and geostrophic heat transport also exhibit opposite signs in the tropics, with the first EOF explaining 42%-43% of the variance of each quantity and a correlation of 0.89 between their PC1s (Figure 4.9).

Ekman heat transport (Figure 4.10, blue) is significantly correlated with the MHT PC1 between 3°N-26°N and between 4°S-10°S with a maximum at around 10°N. The geostrophic heat transport (Figure 4.10, red) is highly correlated with MHT PC1 at 4°N-34°N (especially between 5°N-23°N) and at 6°S-13°S.

4.4.3.2 Contributions of heat transports in layers to the coherence structure

To understand how the Ekman and geostrophic heat transport contribute to the MHT variability it is helpful to examine the mean temperature transport in isopycnal layers for a reference (Figure 4.11). Layer temperature transport per unit depth (PW / m) is calculated by the

temperature transport referenced to 0°C for each isopycnal layer divided the mean depth of the layer to account for unequal spacing of the density coordinates (Figure 4.11). The top two layers represent the mixed-layers, while the next two layers are the buffer layers, where each of these layers have variable density. We only show the layers with mean thickness larger than 1m. Ekman temperature transport in the upper ocean is northward/southward in the northern/southern hemisphere, compensated by the return geostrophic flow beneath (*Reommich,* 1983; *Zhang et al.*, 2003). The geostrophic temperature transport under the Ekman layer north of 18°N is likely owing to the western boundary currents (i.e. Florida Current at 26.5°N, see *Johns et al.* (2011)). The layer temperature transport per unit depth in the deep ocean is small.

The large interannual layer temperature transport (Figure 4.12) is concentrated in the surface ocean and at around the equator above $1033.5 kg/m^3$. We apply EOF analysis to the interannual temperature transports at different layers of the ocean (Figure 4.13), including the total ocean from top to bottom (which is the MHT) (red), the upper ocean above $1030 kg/m^3$ (grey), the middle ocean between $1031-1035 kg/m^3$ (blue) and the deep ocean between 1035-1036.5 kg/m^3 (green) (see Figure 4.11 for the location of the three layers). The PC1s of lowpassed temperature transports in the upper and middle ocean are significantly correlated with the PC1 of the interannual MHT, but PC1 of temperature transport in the deep ocean is not (Figure 4.13b). The EOF1 of interannual temperature transport for the upper ocean (grey) has the same sign between 10°S to 23°N, especially in the northern hemisphere, similar to the pattern of the MHT EOF1 (red); however, it has a peak at around 2°N and then dramatically decreases toward the poles, much sharper than that for the MHT EOF1. The EOF1 of interannual temperature transport in the middle ocean (blue) has a maximum near the equator at 2°S and has larger values in the southern hemisphere than in the northern hemisphere away from the equator. The EOF1 of

interannual temperature transport at deep ocean (green) is much smaller than those in upper and middle oceans.

To further quantitatively investigate the contributions of different layers to the leading mode of the MHT, we calculate the correlations of interannual MHT with itself at each latitude (Figure 4.14a), as well as with the interannual temperature transports in upper/middle/deep ocean at each latitude (Figure 4.14b,c,d). The narrowing of the correlation at around 40°N in Figure 4.14a reveals that the MHT has a coherence structure south and north of 40°N, but not at 40°N. The MHT at the equator is significantly correlated with the upper ocean temperature transport from 7°S to 20°N (Figure 4.14b), and is highly correlated to the mid-ocean temperature transport between 13°S-1°S and between 2°N-27°N (Figure 4.14c). The deep ocean temperature transport plays a minor role on the leading mode of the interannual MHT (Figure 4.14d). These results are consistent with the contributions of the Ekman and geostrophic heat transport in Figure 4.10.

We conclude that the interannual temperature transport at the upper ocean dominated by Ekman process contributes most to the leading mode of interannual MHT, the interannual temperature transport dominated by geostrophic processes in the middle ocean takes a secondary role; whereas the temperature transport in the deep ocean is unimportant in the MHT coherence structure.

4.4.3.3 Interhemispheric transport: diapycnal transport

Both *Reommich* (1983) and *Zhang et al.* (2003) point out that $6\,Sv$ of northward geostrophic flow beneath the Ekman layer in the southern hemisphere is transported to the surface and then swept northward. Given that the coherence structure of interannual heat transport mainly depends on the interannual temperature transport in upper ocean with additional contribution

from the mid-ocean in the southern hemisphere, we next examine how diapycnal transport in the tropics connects the interhemispheric interannual heat transport.

Both the diapycnal velocity at the base of the mixed layer as well as the zonally averaged diapycnal velocity are highly correlated to MHT PC1, with significant positive correlation between 7°S and 2°S, as well as significant negative correlation between 4°N-13°N (Figure 4.15). These results imply that on interannual timescale the northward middle ocean water is transported to the upper ocean in the tropical South Atlantic Ocean, then is carried northward by the Ekman flow and joins the westward Northern Equatorial Current (NEC). This diapycnal transport occurs where there is large variation of the layer temperature transport above the isopycnal $1033 kg/m^3$ between 10°S and the equator (Figure 4.12), and is linked to the same latitudes in the upper ocean. This could also be confirmed by the temperature transport at 2°S in Figure 4.14c. The temperature transport in the middle ocean at 2°S is positively correlated with the interannual MHT anomaly from almost 20°S to 20°N, implying the contribution of the temperature transport in the middle ocean of the South Atlantic tropics to the interannual MHT coherence structure. Previous studies show that the temporal variations of this diapycnal transport may be associated with TAV (*Nobre and Shukla,* 1996) and the asymmetric SST about the equator where the mean SST in the North Atlantic tropics is about 1°C cooler than that in the South Atlantic tropics (*Roemmich,* 1983). However, whether this diapycnal transport in the southern tropics is from upwelling or from the obduction to the upper ocean is still uncertain and needs further investigation.

4.4.3.4 Wind forcing

In both upper and middle oceans, velocity variation is linked to the wind stress or wind stress curl via Sverdrup dynamics (*Sverdrup,* 1947). Given that the meridional velocity variability in

the subtropical gyre is more important than the temperature variability for the interannual MHT in the Atlantic (*Robson et al.,* 2012; *Zheng and Giese*, 2009; *Jayne and Marotzke, 2001*; *Seager et al.*, 2001; *Schott et al.,* 2004), we focus on the correlation between wind stress curl and MHT PC1 (Figure 4.16). We find significant correlation that originates from 5°S-10°S at 0-10°W, extends northwest through the interior ocean, and then gradually merges from the interior ocean into North Brazil Current (NBC) and Guiana Current between the equator and 12°N. The correlation is not significant between 13°N-17°N. North of 17°N, there is a significant negative correlation between 17°N-30°N at 30°W-67°W.

To determine the link between the oceanic meridional velocity, the wind-stress curl and the leading mode of MHT variability, we examine correlations at each grid point between MHT PC1 and meridional velocity and between MHT PC1 and wind stress curl. The results are shown at 8.5°S, 5.8°S, and 7.3°N (Figure 4.17-19). At 8.5°S (Figure 4.17), the correlation between wind stress curl and MHT PC1 is positive, indicating that a positive wind stress curl increases the MHT PC1. We expect that a positive wind stress curl anomaly would give northward anomalous flow as determined from the Sverdrup balance, and that the resulting flow would result in northward anomalous heat transport. This is also born out in the correlations of meridional velocity and MHT PC1 with a positive value in the middle ocean between 0-10°W. At 5.8°S, the region of high correlation between meridional velocity and MHT PC1 is westward of that seen at 8.5°S and occurs between 3°W and 18°W (Figure 4.18). Diapycnal transport into the mixed-layer is also associated with an increase in MHT PC1 (Figure 4.15). At 7.3°N, both positive geostrophic velocity near the western boundary and the Ekman heat transport in the interior of the basin are to the north when interannual MHT is to the north (Figure 4.19). The regression map of wind velocity on MHT PC1 (Figure 4.20) shows northeast winds in the northern

hemisphere between the equator and 30°N and northwest winds between the equator and 10°S correspond to the MHT coherence.

4.5 Conclusion

Based on the seven historical simulations in CMIP5 coupled models and one hindcast simulation from the ocean model GOLD from 1971 to 2009, the characteristics of the interannual MHT variability are investigated. Generally at low latitudes south of 40°N, interannual variability dominates and is much stronger than the decadal variability; whereas at high latitudes north of 40°N the decadal variability prevails, consistent with the results from other studies derived from ocean models and observations (*Zheng and Giese,* 2009; *Kelly et al.,* 2014; *Jayne and Marotzke,* 2001). The first EOFs of the interannual MHT anomaly from all the models show the same sign from about 20°S to about 30°N with a maximum in the tropics, decaying toward the poles, although the meridional extent of the EOF1s depends on models.

We use the ocean model GOLD to perform detailed analysis of what components of the flow control the interannual MHT variability. The EOF leading mode of the interannual MHT in GOLD can capture the interannual MHT variability between 15°S and 30°N, with the EOF leading mode accounting for 50% of the interannual MHT variance. This EOF leading mode of interannual MHT is controlled by Ekman heat transport anomalies between 7°S and 20°N and the geostrophic heat transport beneath the Ekman layer from 13°S to 27°N, excluding the equator. The Ekman transport contributes most to the coherence structure of interannual MHT, whereas the geostrophic transport takes a secondary role. The deep ocean makes a negligible contribution to the MHT coherence structure.

The schematic diagram (Figure 4.21) exhibits the key components contributing to the MHT coherence structure. The positive wind stress curl in the tropics, northeast winds in the northern tropics and northwest winds in the southern tropics are the wind forcing corresponding to MHT coherence. The water in northward geostrophic transport is transported to the upper ocean in the South Atlantic tropics and then carried to the north by Ekman transport driven by the northwest and northeast winds. The positive wind stress curl assures that the transport is northward as a combination of Ekman and geostrophic transport in the tropics. The geostrophic heat transport is significant for the MHT coherence structure in both hemispheres, while the Ekman heat transport plays an more important role in the northern hemisphere than in the southern hemisphere.

The Atlantic Meridional Mode (AMM) is the dominant physical process of coupled ocean-atmosphere variability in the Atlantic tropics on interannual to decadal timescales. During a positive phase of the AMM, there are warmer SST and weaker winds (Figure 4.22a). After we correlate the SST anomaly with minus MHT PC1 and regress the wind velocity on minus MHT PC1, we find that the MHT PC1 related SST and wind anomaly pattern (Figure 4.22b) are similar to the positive AMM, suggesting that ocean-atmosphere coupling is important for explaining the MHT coherence. *Richter et al.* (2014) reveal that the CMIP5 models can reproduce reasonable interannual SST anomalies, despite their mean state biases. All of these imply that the AMM on interannual timescale is robust among models and is likely to related to MHT coherence. The detailed linkage between AMM and MHT coherence needs further investigation.

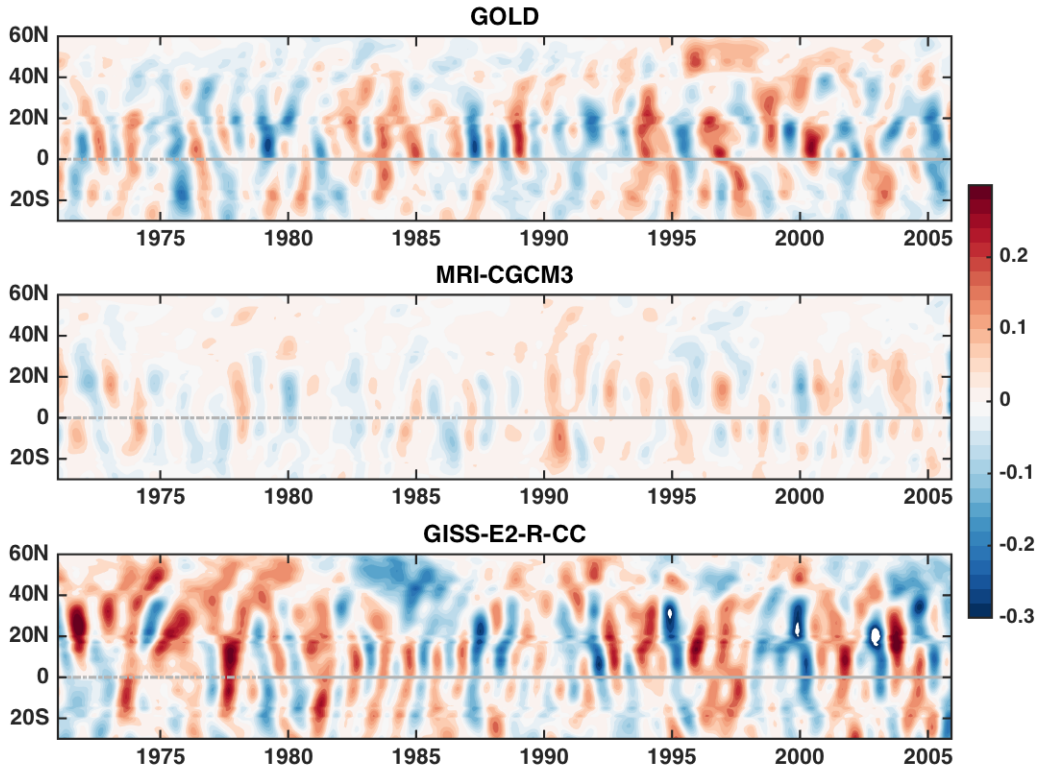

Figure 4.1 The 1-year lowpassed MHT anomaly in the Atlantic Ocean from 1971–2005 in (a) GOLD, (b) MRI-CGCM3 and (c) GISS-E2-R-CC. Units: PW .

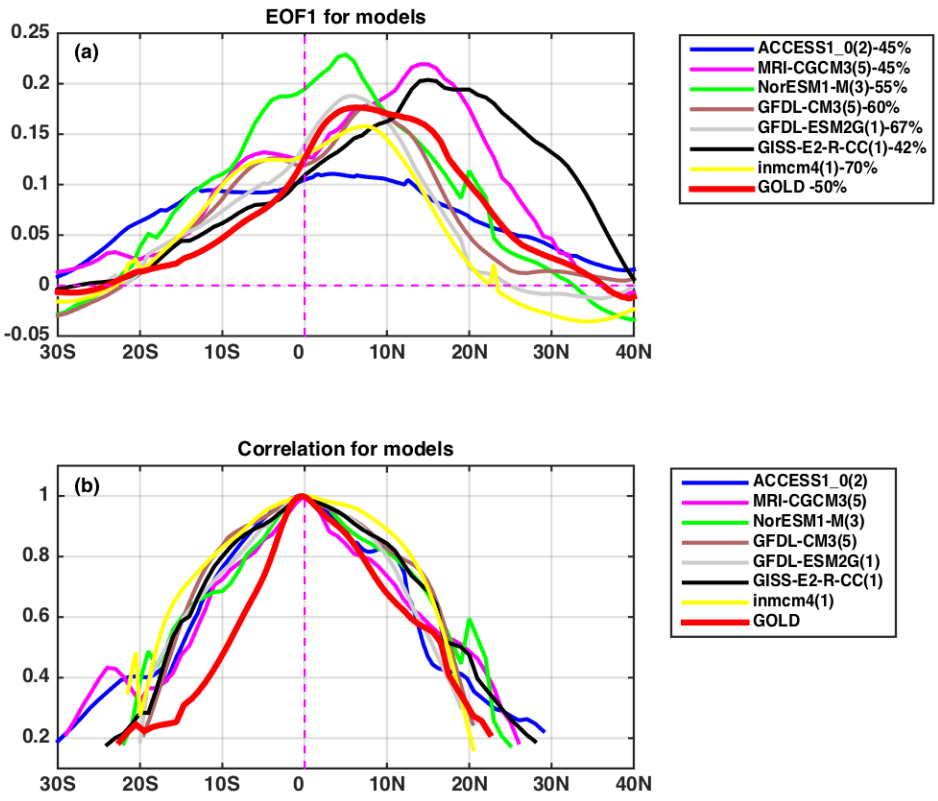

Figure 4.2 (a) EOF1s of 1-year lowpassed MHT and (b) correlations between 1-year lowpassed MHT on the equator and at all latitudes in the Atlantic Ocean for the ensemble-mean from different models. The models are ACCESS1-0 (blue), MRI-CGCM3 (magenta), NorESM1-M (green), GFDL-CM3 (brown), GFDL-ESM2G (grey), GISS-E2-R-CC （black）, INMCM4 (yellow) and GOLD (red). The integers in the parentheses of the legend indicate the number of ensemble members in models. The percentage in (a) represents the fraction of variance explained by the EOF1s. (b) only shows the correlations above 95% significance level.

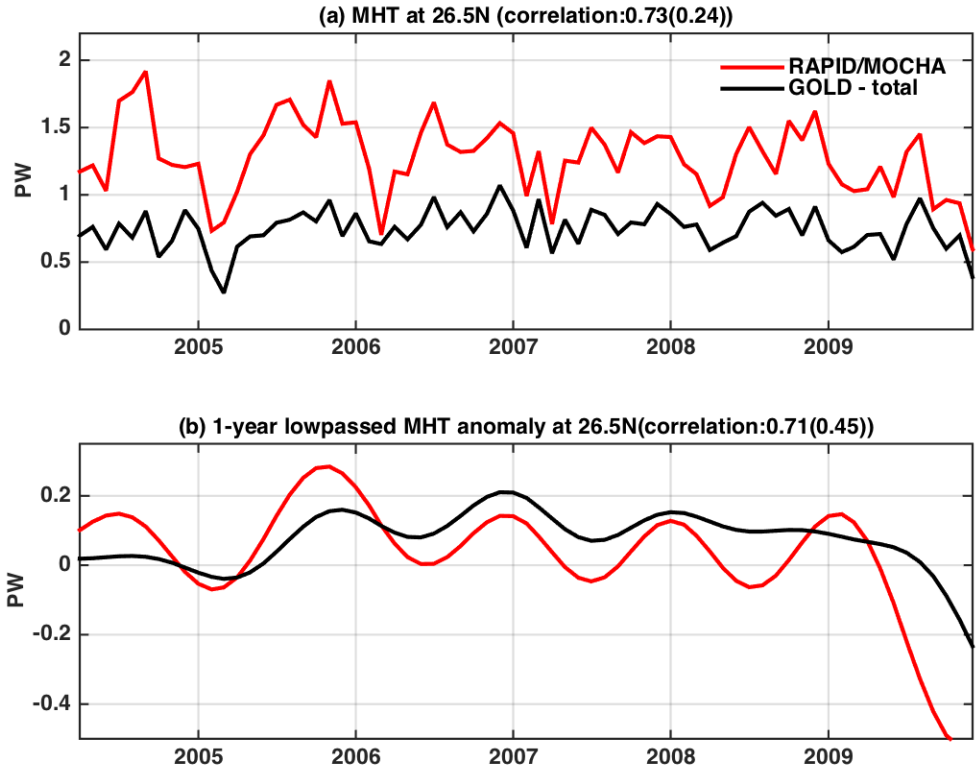

Figure 4.3 Comparison between MHT in GOLD (black) and from RAPID-MOCHA line (red) at 26.5°N. (a) total MHT and (b) 1-year lowpassed MHT.

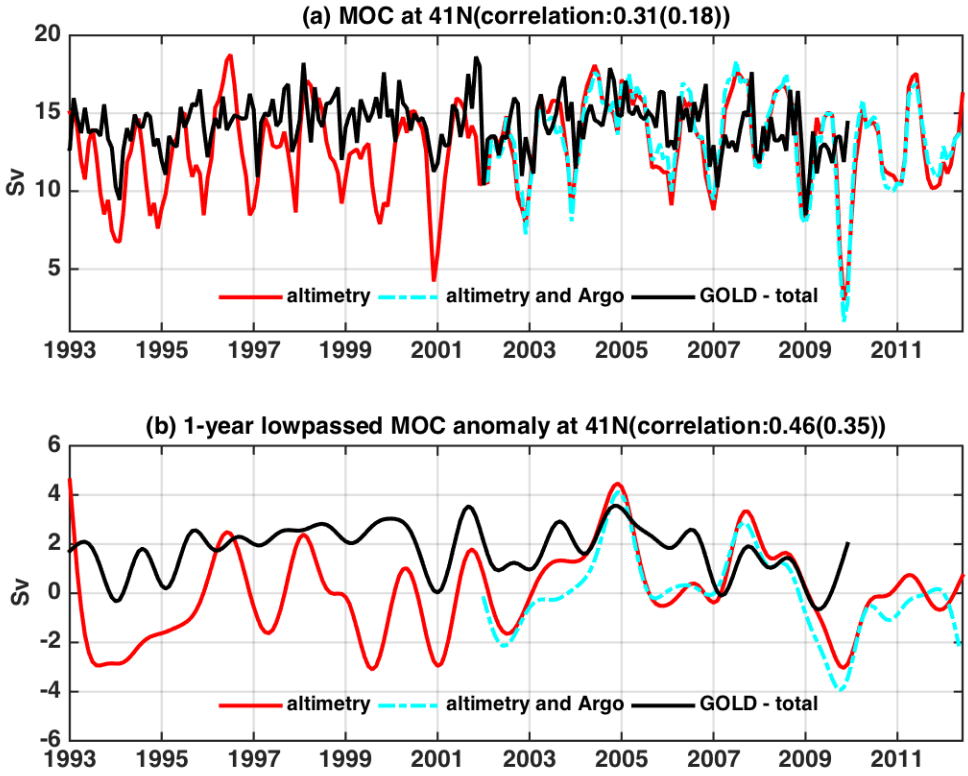

Figure 4.4 Comparison between AMOC in GOLD and SSH/Argo derived AMOC at 41°N. (a) total AMOC and (b) 1-year lowpassed AMOC. Black line is for AMOC in GOLD, redline is for SSH derived AMOC, the dashed cyan line is for SSH and Argo derived AMOC.

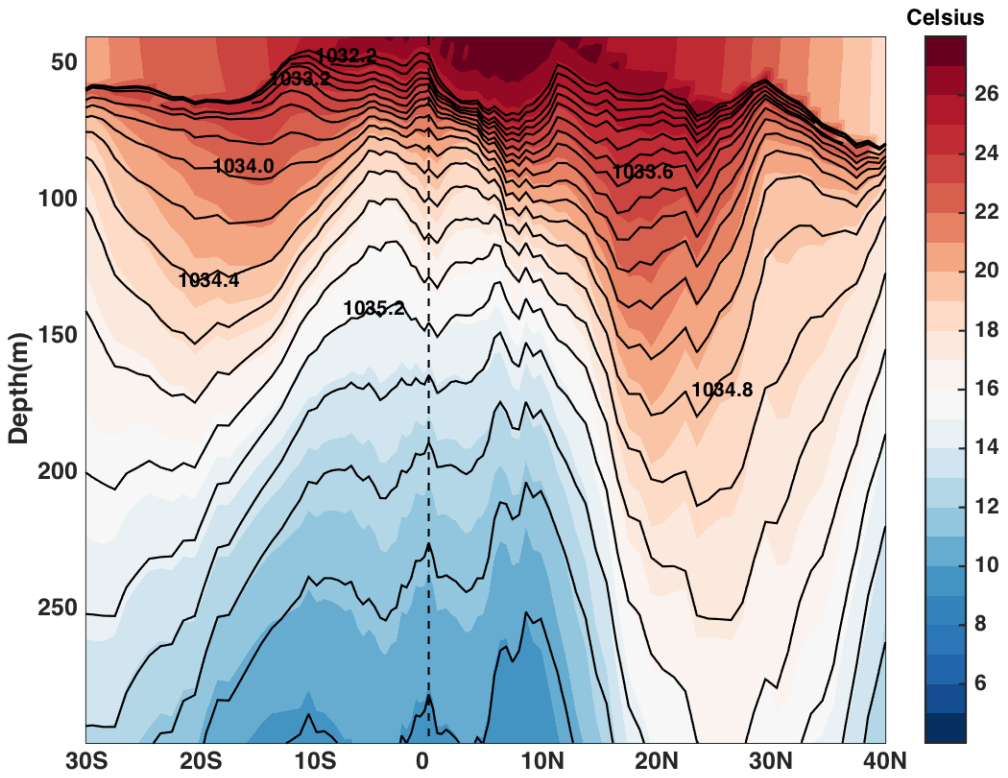

Figure 4.5 Potential temperature (°C, colored shading) and potential density referenced to 2000 m (kg/m^3 , black contours) for the upper 300m. The contour interval for density is 0.2 kg/m^3 .

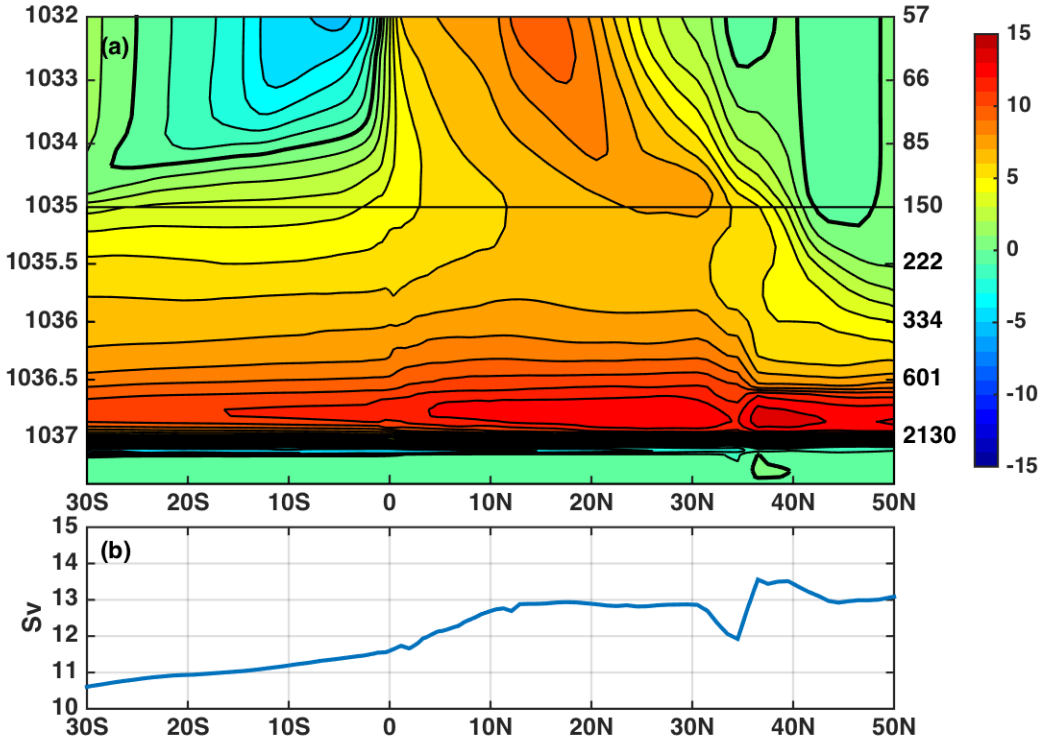

Figure 4.6 (a) Time-mean of zonally integrated and vertically cumulative (from the surface, including mixed and buffer layers) volume transport in the Atlantic Ocean in GOLD hindcast, the isopycnals heavier than $1032 kg/m^3$ are shown. (b) AMOC at all latitudes in the Atlantic Ocean in GOLD hindcast. The left Y-axis label for (a) is isopycnals ($\sigma_2, kg/m^3$) and right label is the corresponding zonally averaged depth (m).

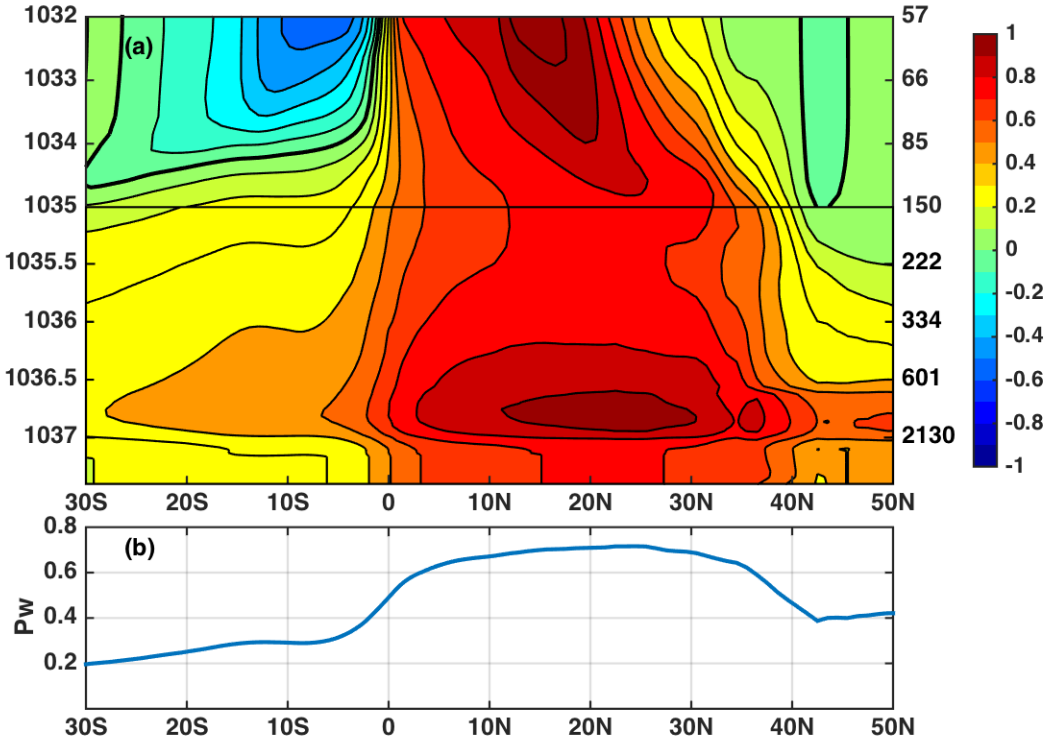

Figure 4.7 (a) Time-mean of zonally integrated and vertically cumulative (from the surface, including mixed and buffer layers) heat transport in the Atlantic Ocean in GOLD hindcast, the isopycnals larger than $1032 kg/m^3$ are shown. (b) MHT at all latitudes in the Atlantic Ocean in GOLD hindcast. The left Y-axis label for (a) is isopycnals ($\sigma_2, kg/m^3$) and right label is the corresponding zonally averaged depth (m).

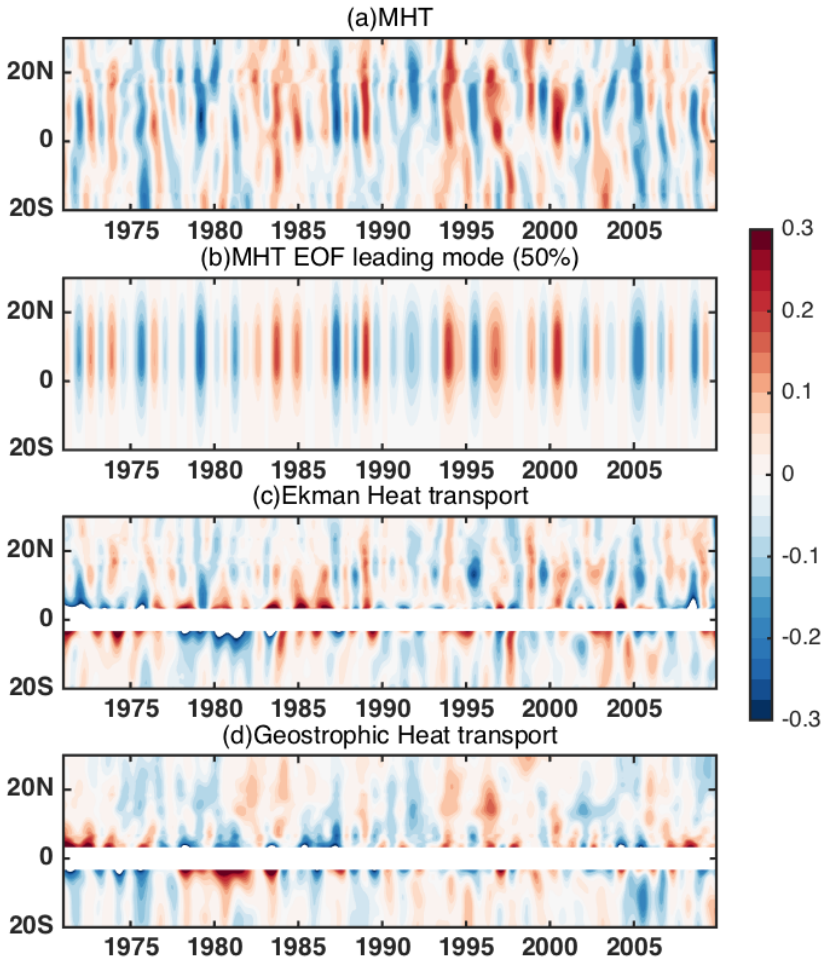

Figure 4.8 Interannual MHT anomaly (a), MHT EOF leading mode (b), Ekman heat transport (c) and geostrophic transport (d) in GOLD.

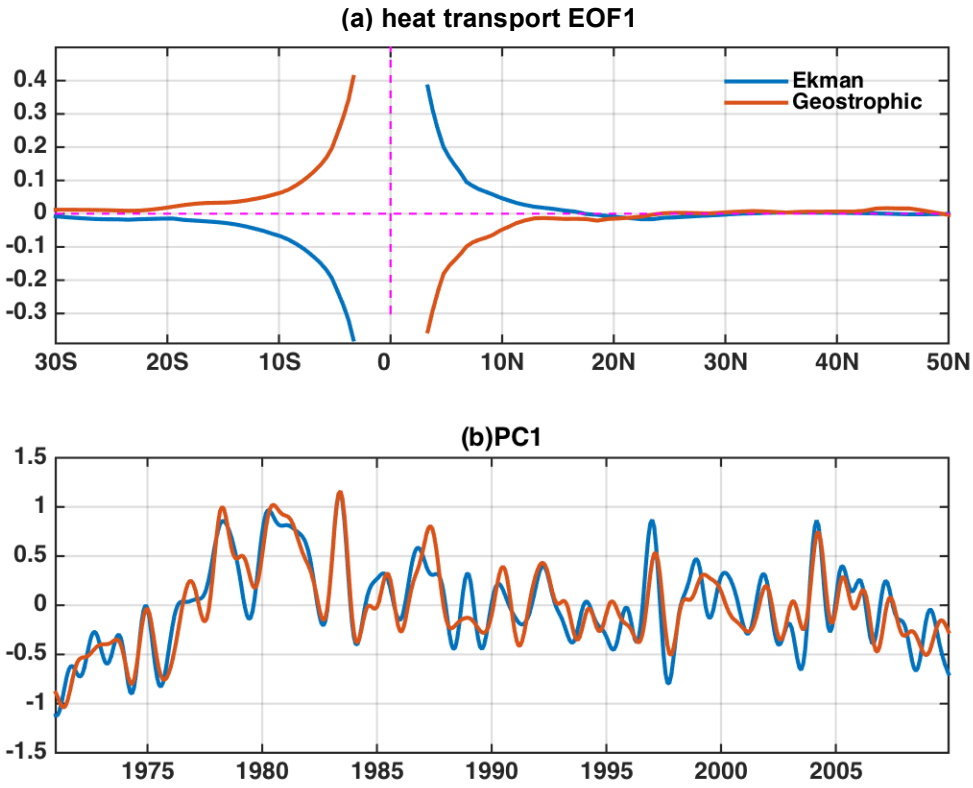

Figure 4.9 (a) EOF1 and (b) PC1 of the 1-year lowpassed Ekman (blue) and geostrophic (red) heat transport. Units in (a): PW.

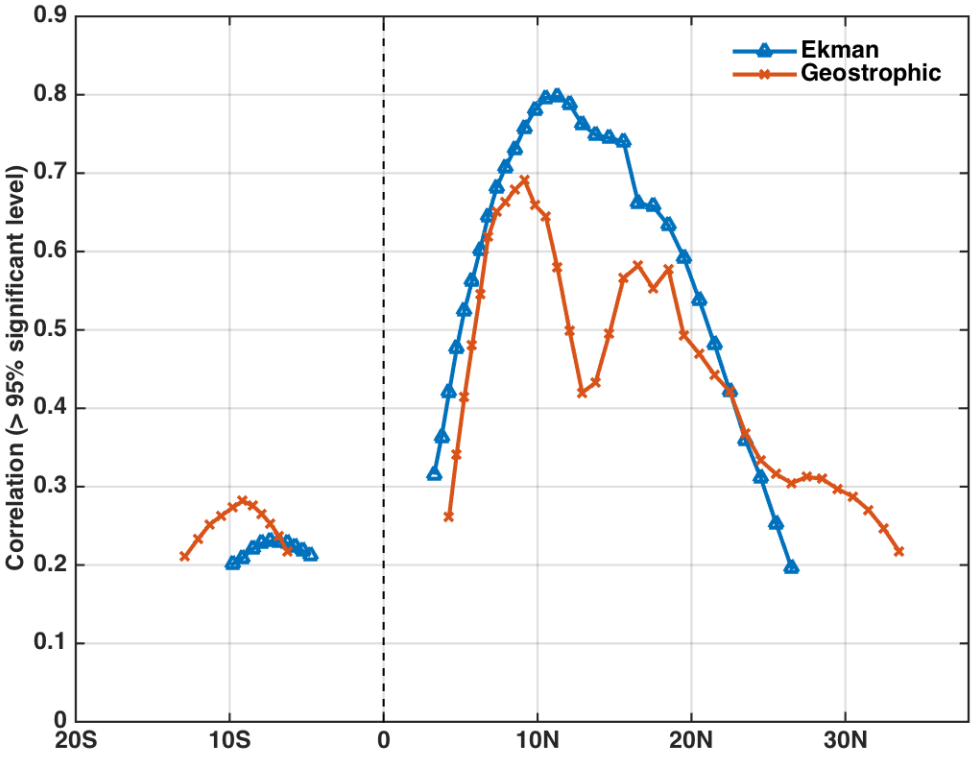

Figure 4.10 Correlation between MHT PC1 and Ekman heat transport (blue triangle line) /geostrophic heat transport (red dot line).

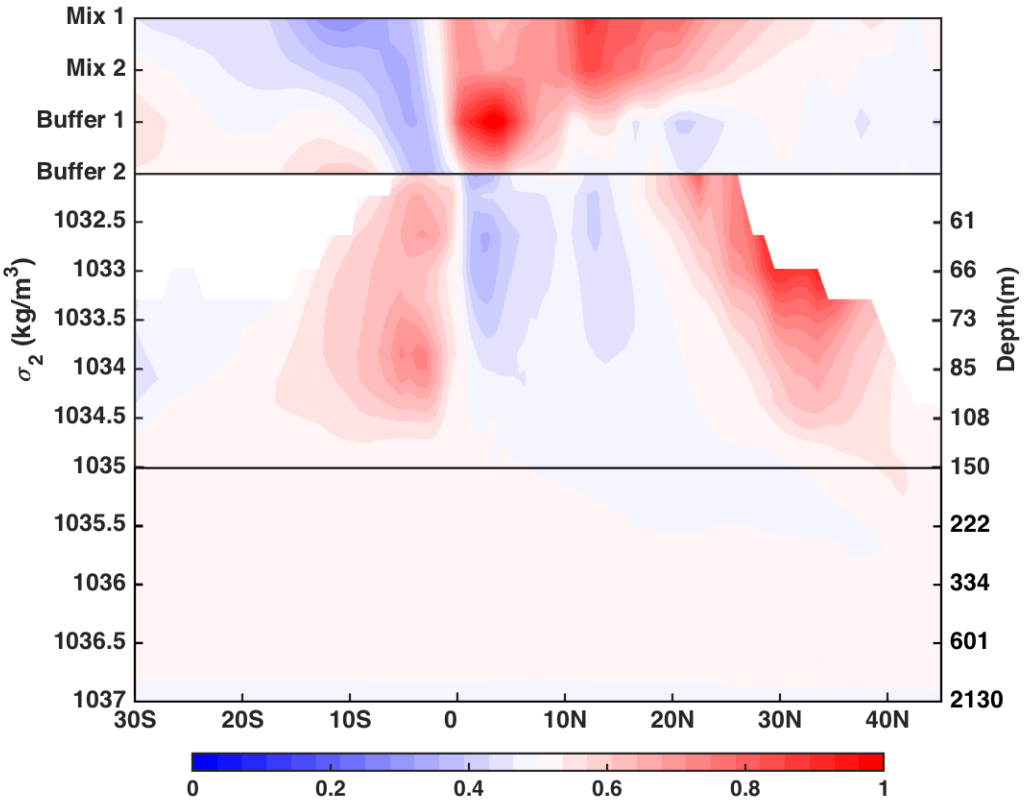

Figure 4.11 Layer temperature transport per unit depth (PW/m), which is calculated by the temperature transport for each isopycnal layer over the mean depth of the layer. The left Y-axis label is isopycnals ($\sigma_2, kg/m^3$) and right label is the corresponding zonally averaged depth (m). The upper four layers are two mix layers and two buffer layers with no fixed isopycnals labeled. The mean isopycnal depth less than 1m is in white blank.

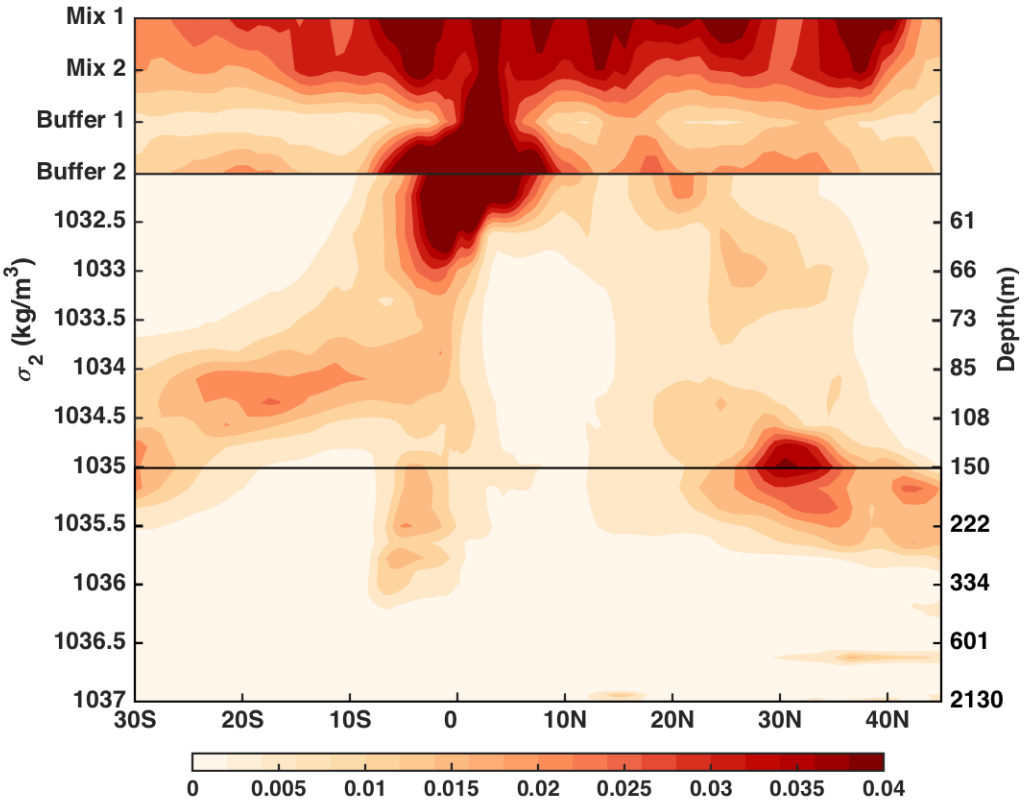

Figure 4.12 Standard deviation of the layer temperature transport (PW). The left Y-axis label is isopycnals ($\sigma_2, kg/m^3$) and right label is the corresponding zonally averaged depth (m).

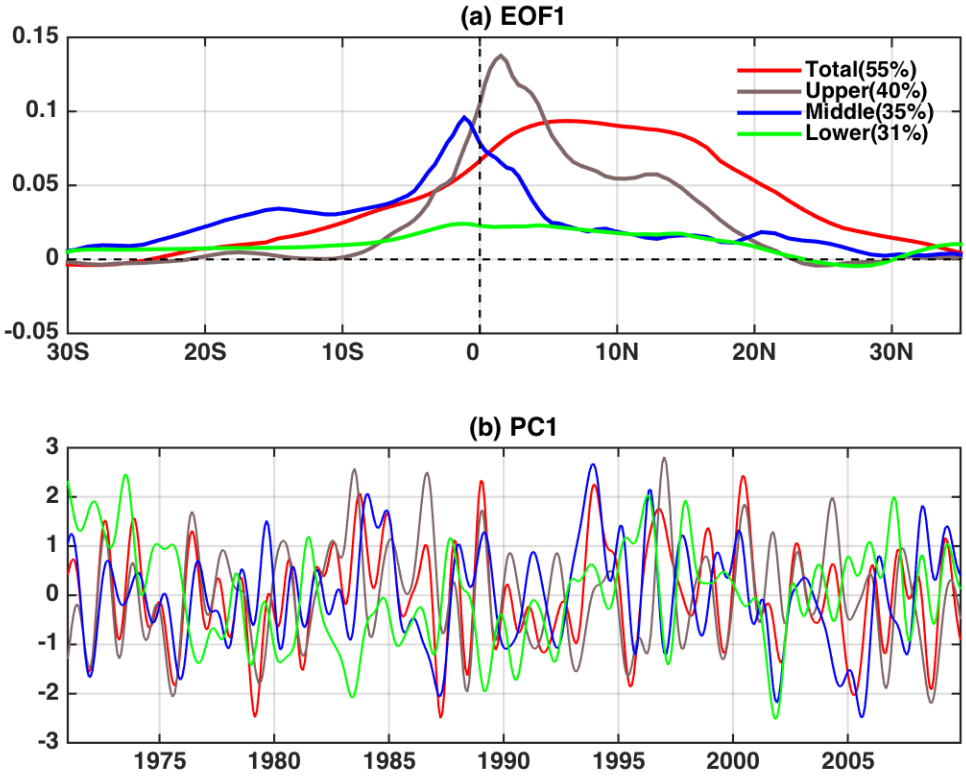

Figure 4.13 The EOF1 (a) and PC1 (b) of the interannual temperature transport for the total ocean from top to bottom (red, same as the interannual MHT leading mode), in the upper ocean above $1030 kg/m^3$ (grey), in the middle ocean between $1031-1035 kg/m^3$ (blue), and in the deep ocean between 1035-1036.5 kg/m^3 (green). The PC1s are normalized. EOF1s show the magnitude differences. Units for (a) are PW .

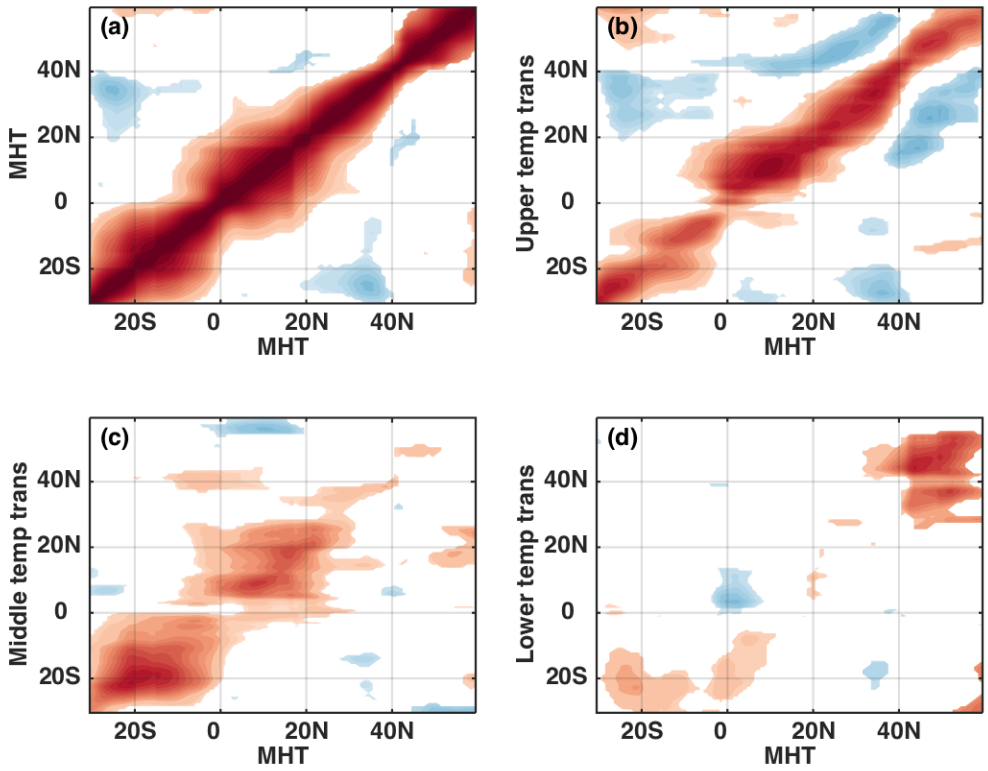

Figure 4.14 Significant correlations between interannual MHT at each latitude (a), between the interannual MHT and temperature transport in the upper/middle/deep ocean (b,c,d). Only correlations above the 95% significance level are shown.

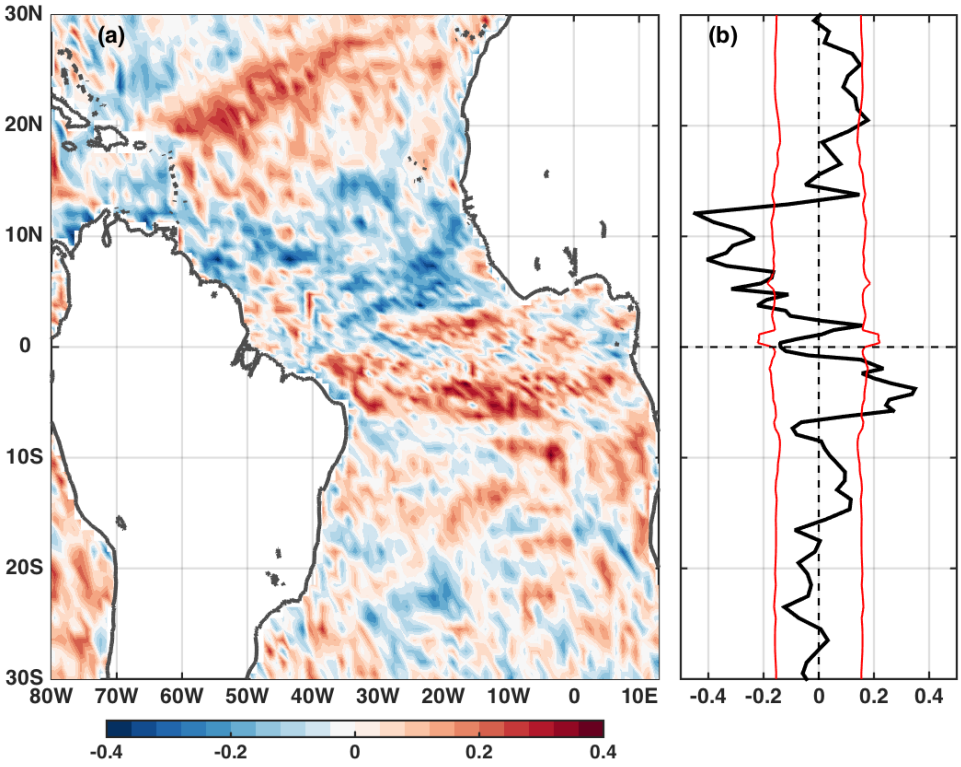

Figure 4.15 (a) Correlations between 1-year lowpassed diapycnal velocity at the base of the second mix layer and MHT PC1, (b) Correlations between 1-year lowpassed zonally averaged diapycnal velocity and MHT PC1. The red lines in (b) represent 95% significance level.

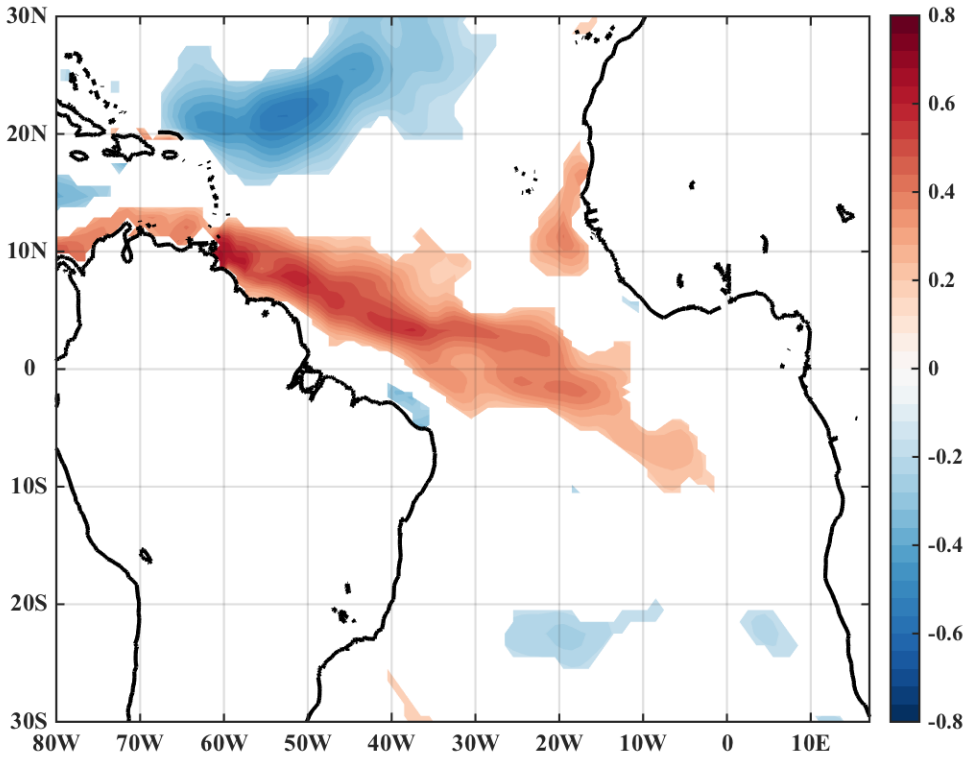

Figure 4.16 Correlations between lowpassed wind stress curl and MHT PC1. The white blank area represents the correlations below 95% significance level.

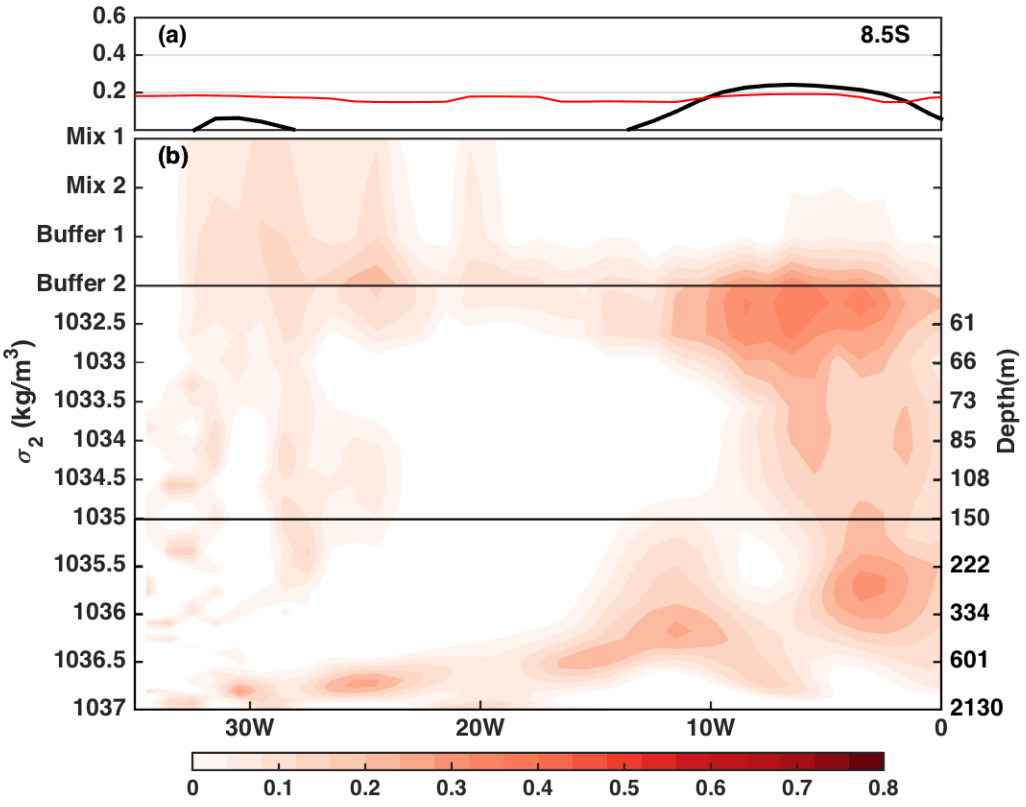

Figure 4.17 (a) Correlations between lowpassed wind stress curl and MHT PC1 at 8.5°S as a function of longitude, (b) correlation between lowpassed meridional velocity and MHT PC1 at 8.5°S as a function of longitude and density. The red line in (a) is the 95% significance level.

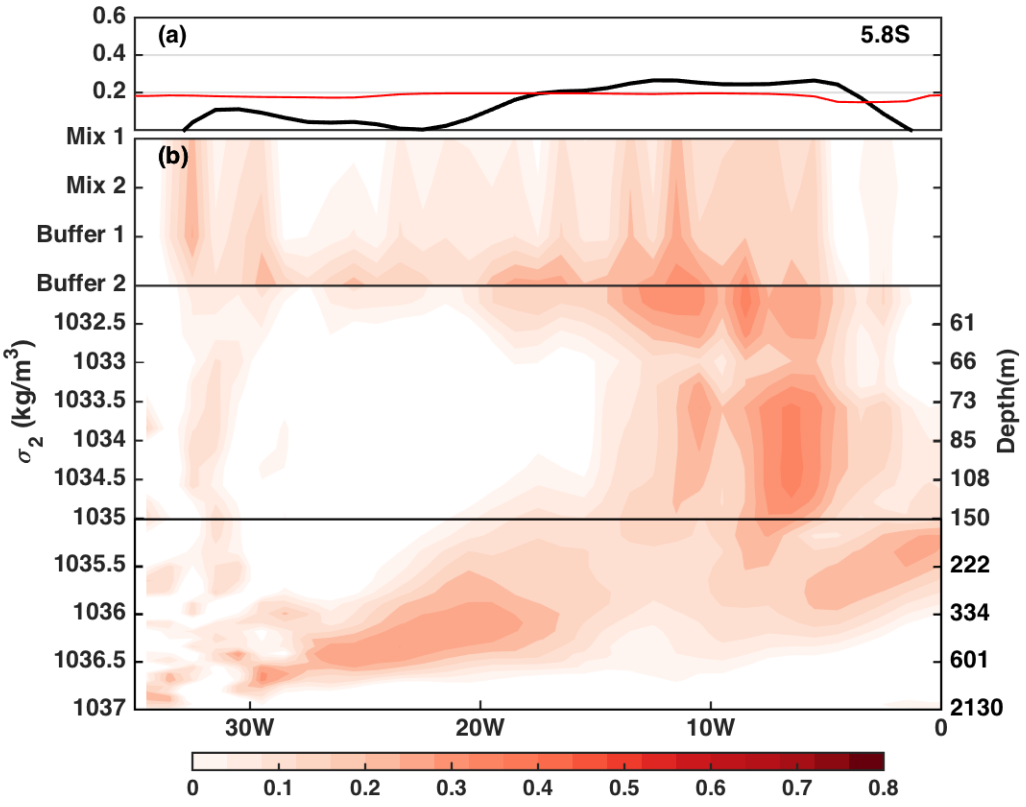

Figure 4.18 Same as Figure 4.17, but at 5.8°S.

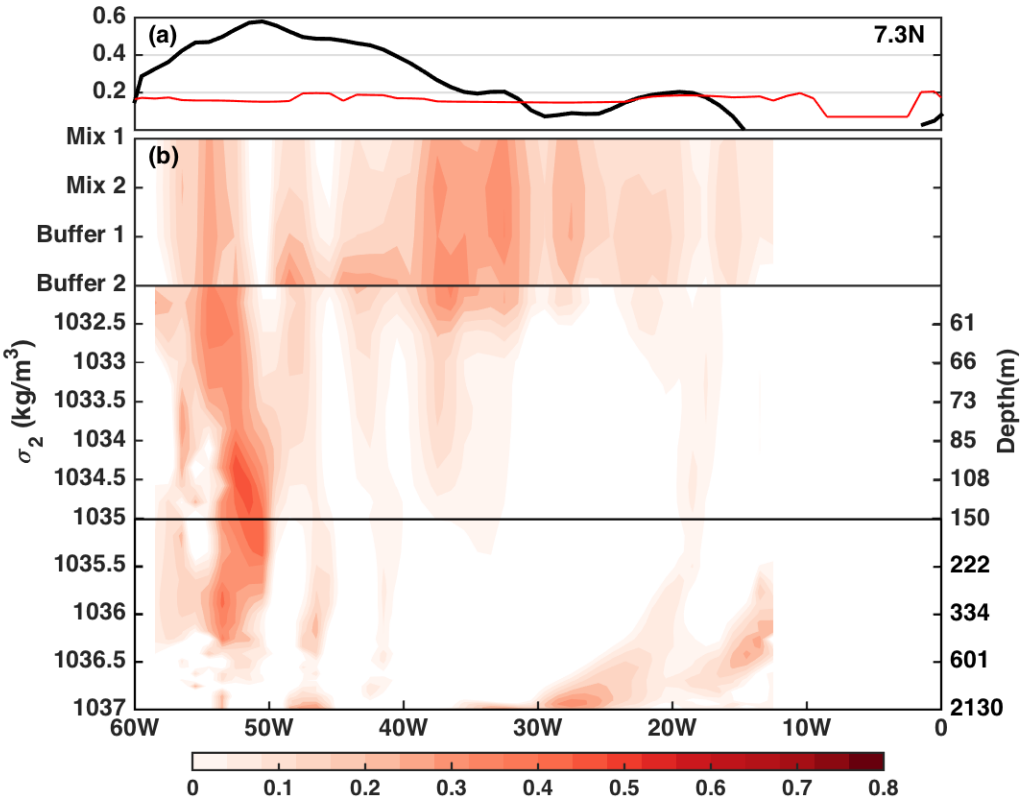

Figure 4.19 Same as Figure 4.17 and 4.18, but at 7.3°N.

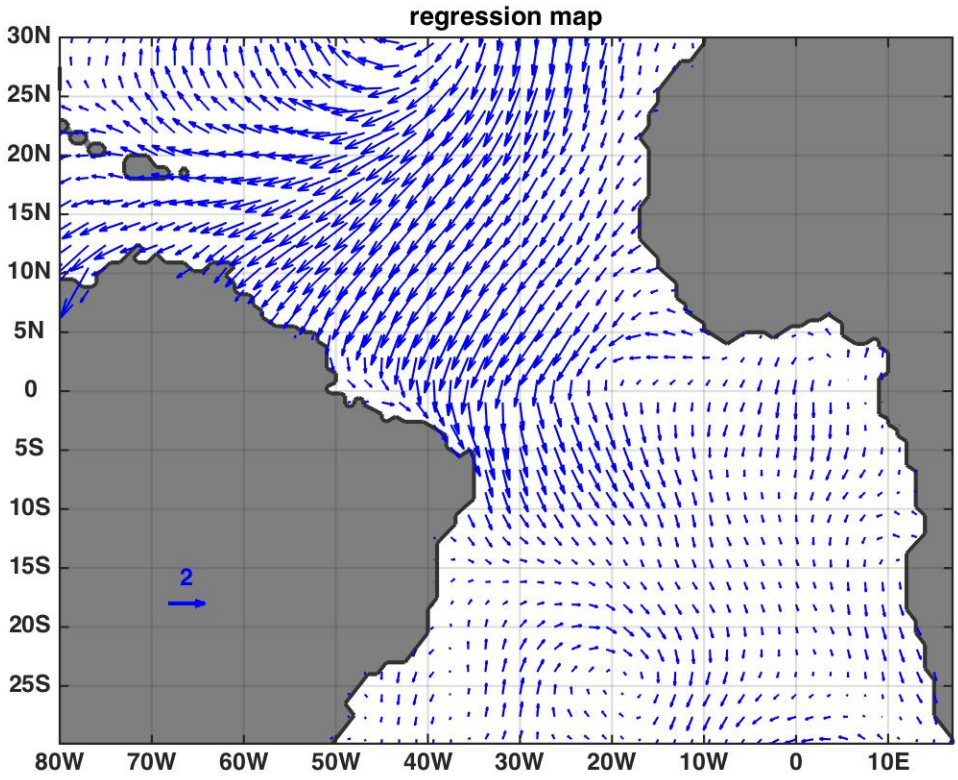

Figure 4.20 Regression map of wind velocity on MHT PC1.

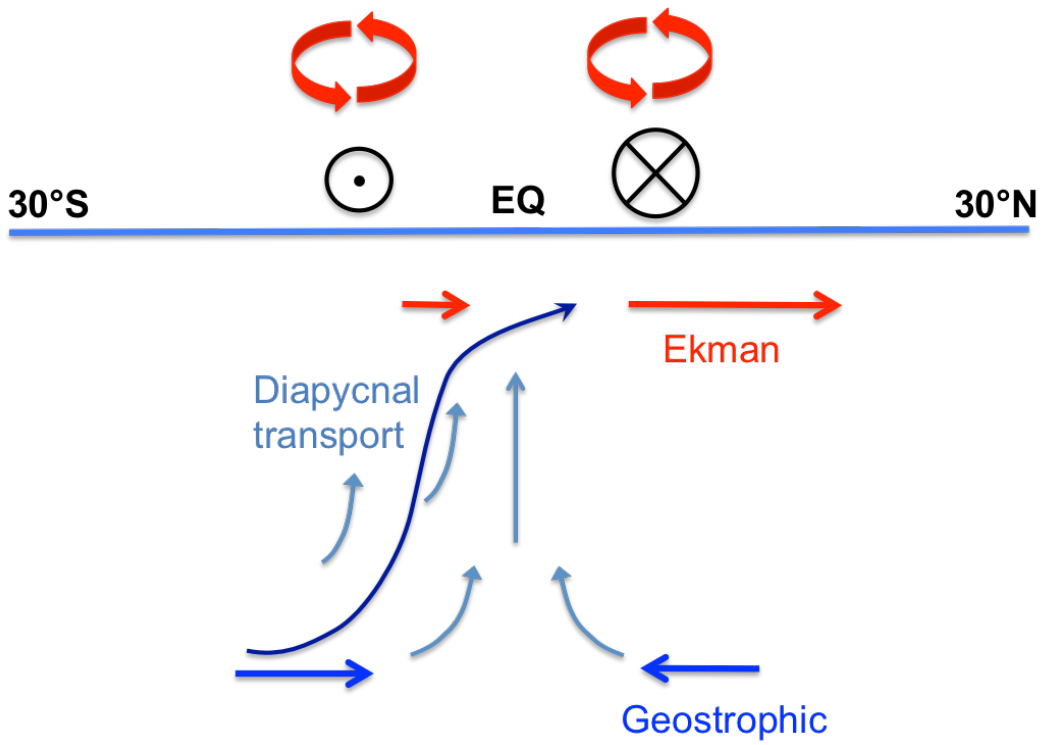

Figure 4.21 Schematic diagram for the MHT coherence structure.

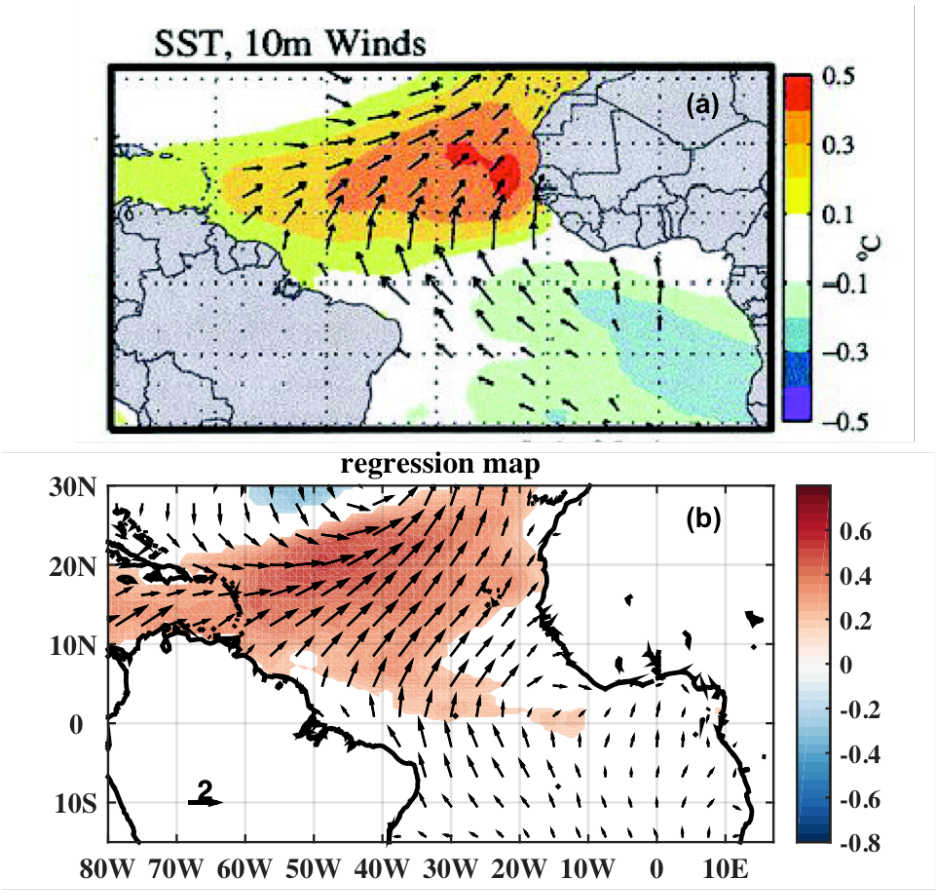

Figure 4.22 (a) Positive Atlantic meridional mode (AMM) with warmer SST in the northern hemisphere, southwest wind anomaly north of the equator and southeast wind anomaly south of the equator (*Chiang and Vimont,* 2004). (b) MHT PC1 related SST and wind velocity. Shading area is the correlation between SST and minus MHT PC1. Arrows represent the regression coefficient of wind velocity on minus MHT PC1.

Chapter 5. CONCLUSIONS

This dissertation focuses on understanding the variability of ocean circulation and meridional heat transport (MHT) in the Atlantic Ocean on different timescales. The main scientific focuses are the characteristics of the variability of the ocean circulation and MHT and what controls the structure of the variability. Satellite and in-situ observations, simplified models, climate coupled models and ocean-only model are used to help quantitatively describe the characteristics and explore the mechanisms that control the variability. This work aims to advance our knowledge of the role of ocean in our dynamic climate system.

Chapter 2 focuses on the seasonal and interannual-to-decadal variations of large-scale altimetric SSH owing to surface heating and wind forcing in the presence of topography using simplified models. On the seasonal timescale locally forced thermosteric height explains most of the SSH variance north of 18°N. First mode linear long baroclinic Rossby wave explains most of the variance between 10°N-15°N and are also important east of Greenland. On interannual-to-decadal timescales, local thermosteric height remains important at several locations in the middle and high latitudes. A topographic Sverdrup response explains interannual-to-decadal SSH between 53°N and 63°N east of Greenland, suggesting the important role of topography in the subpolar region. Farther south, the linear Rossby wave model explain SSH variations on interannual-to-decadal timescales between 30°N and 50°N from mid-basin to the eastern boundary.

In Chapter 3, we use perturbed experiments and 1000-year control simulation of the GFDL coupled model CM2.1 to investigate the evolution of AMOC and its fingerprint on the decadal timescale. The AMOC anomaly associated with changes in the North Atlantic Deep Water (NADW) formation slowly propagates southward due to the existence of the NADW interior

pathway north of 34°N. We show that this slow southward propagation of the AMOC anomaly is crucial for the evolution of the AMOC fingerprint - the leading mode of upper ocean heat content in the extra-tropical North Atlantic. A positive AMOC anomaly in northern high latitudes driven by external buoyancy forcing leads to a convergence/divergence of the Atlantic MHT anomaly in the subpolar/Gulf Stream region, thus warming in the subpolar gyre and cooling in the Gulf Stream region after several years. Recent decadal prediction studies successfully predicted the observed warming in the subpolar region in the mid 1990s. Our results here provide the physical mechanism for this enhanced decadal prediction skills in the subpolar region.

The study presented in Chapter 4 uses seven simulations in the CMIP5 archive as well as a hindcast simulation in the isopycnal ocean model GOLD from 1971 to 2009 to investigate the interannual variability in the Atlantic MHT. The spatial pattern of the leading EOF mode of the interannual MHT anomaly from all of the model simulations peaks near the equator and reaches into the subtropics in both hemispheres. A more detailed examination of the circulation and velocity of GOLD reveals that Ekman heat transport anomalies between 7°S-20°N and the geostrophic transport beneath the Ekman layer from 13°S-27°N (except the equator) contribute to this MHT leading mode, while the contribution of the deep ocean is negligible. The connection between the hemispheres is completed through diapycnal transport of the northward geostrophic transport beneath the Ekman layer in the southern tropics; this water reaches the upper ocean and then the northward Ekman transport takes over. Wind in the tropics is the main external forcing for this MHT coherence structure.

In this dissertation, we identify several mechanisms that control ocean circulation variability and associated MHT. We show the dominance of the wind-driven topographic Sverdrup in interannual-to-decadal SSH observations in the subpolar North Atlantic. We also reveal that slow

advection of perturbations from the deep subpolar North Atlantic into the subtropics can lead to changes of UOHC and may be useful for predicting heat content and upper ocean temperature north of 34°N on decadal timescale. We further reveal that there is a strong wind-driven coherence structure of the interannual MHT in low latitudes; diapycnal transport south of the equator is key to allow interhemispheric heat transport anomalies. These studies are linked to each other. For example, the interannual MHT/AMOC can be explained by the Ekman and geostrophic transport in the northern subtropics, which is highly related to the contributions of Sverdrup models to the interannual SSH changes in the same area; SSH and in-situ observations could be used to infer the AMOC and MHT transport (*Willis,* 2010). Another one is, the topography in the high latitude North Atlantic might affect how the AMOC might respond to wind forcing on decadal time scale.

While this dissertation has studied the variability of ocean circulation, AMOC and MHT on different timescales, many opportunities for extending the scope of this dissertation remain. For instance, the influence of the topography on the ocean circulation in the high latitudes should be further investigated using analysis of a comprehensive ocean model (i.e. GOLD). The impact of slow advection of the AMOC on the heat content north of 34°N should be tested in other climate models. The contribution of the wind forcing on the interannual MHT/AMOC in low latitudes could be compared or linked to the rapid propagation of AMOC signals from the high latitudes via a southward propagating rapid coastal wave. All of these future studies could add advanced insights on the ocean circulation and heat transport variability and deserve further investigations.

BIBLIOGRAPHY

Adcroft, A., and R. Hallberg (2006), On methods for solving the oceanic equations of motion in generalized vertical coordinates. *Ocean Modelling*, *11*(1-2), DOI:10.1016/j.ocemod.2004.12.007.

Ba, J., N. S. Keenlyside, M. Latif, W. Park, H. Ding, K. Lohmann, J. Mignot, M. Menary, O. H. Otterå, B. Wouters, D. S. Melia, A. Oka, A. Bellucci, and E. Volodin. (2014), A multi-model comparison of Atlantic multidecadal variability. *Clim. Dynam., 43*, 2333-2348.

Berrisford, P., D. Dee, P. Poli, R. Brugge, K. Fielding, M. Fuentes, P. Kallberg, S. Kobayashi, S. Uppala, and A. Simmons (2011), *The ERA-Interim archive, version 2.0.* ERA report series. 1. Technical Report. ECMWF pp23.

Bingham, R. J., C. W. Hughes, V. Roussenov, and R. G. Williams (2007), Meridional coherence of the North Atlantic meridional overturning circulation, *Geophys. Res. Lett., 34*, L23606, doi:10.1029/2007GL031731.

Boccaletti, G., R. Ferrari, A. Adcroft, D. Ferreira, and J. Marshall (2005), The vertical structure of ocean heat transport. *Geophys. Res. Lett., 32*, L10603, doi: 10.1029/2005GL022474.

Böning, C. W., M. Scheinert, J. Dengg, A. Biastoch, and A. Funk (2006), Decadal variability of subpolar gyre transport and its reverberation in the North Atlantic overturning, *Geophys. Res. Lett.*, *33*, L21S01, doi:10.1029/2006GL026906.

Bower, A. S., M. S. Lozier, S. F. Gary, and C. W. Böning (2009), Interior pathways of the North Atlantic meridional overturning circulation, *Nature, 459*, 243–248, doi:10.1038/nature07979.

Brennan, C. E., R. J. Matear, and K. Keller (2008), Measuring oxygen concentrations to improve the detection capabilities of an ocean circulation observation array, *J. Geophys. Res., 113*,

C02019, doi:10.1029/2007JC004113.

Broecker, W. S. (1991), The great ocean conveyor. *Oceanography, 4*, 79-89.

Cabanes, C., T. Huck and A. C. D. Verdière (2006), Contributions of Wind Forcing and Surface Heating to Interannual Sea Level Variations in the Atlantic Ocean, *J. Phys. Oceanogr.*, *36*, 1739–1750.

Chambers, D. P., B. D. Tapley, and R. H. Stewart (1997), Long-period ocean heat storage rates and basin-scale heat fluxes from TOPEX, *J. Geophys. Res.*, *102*(C5), 10525–10533, doi:10.1029/96JC03644.

Chelton, D. B. and M. G. Schlax (1996), Global observation of oceanic Rossby waves, *Science, 272*, 234–238.

Chelton, D. B., M. G. Schlax, and R. M. Samelson (2011), Global observations of nonlinear mesoscale eddies, *Prog. Oceanogr., 91*, 167-216.

Chiang, J. C. H., and D. J. Vimont (2004), Analagous meridional modes of atmosphere-ocean variability in the tropical Pacific and tropical Atlantic, *J. Climate,17*(21), 4143-4158.

Cohen-Solal, E., and H. Le Treut (1997), Role of the oceanic heat transport in climate dynamics: A sensitivity study with an atmospheric general circulation model, *Tellus, 49*A, 371-387.

Cromwell, D. (2006), Temporal and spatial characteristics of sea surface height variability in the North Atlantic Ocean, *Ocean Sci., 2*, 147-159, doi:10.5194/os-2-147-2006.

Cummins, P. F. (1991), The barotropic response of the subpolar North Pacific to stochastic wind forcing, *J. Geophys. Res., 96(*C5), 8869–8880, doi:10.1029/91JC00487.

Cunningham, S. A., T. Kanzow, D. Rayner, M. O. Baringer, W. E. Johns, J. Marotzke, H. R. Longworth, E. M. Grant, J. J.-M. Hirschi, L. M. Beal, C. S. Meinen, and H. L. Bryden

(2007), Temporal Variability of the Atlantic Meridional Overturning Circulation at 26.5°N, *Science, 317*, 935-938.

Delworth, T. L., and Coauthors (2006), GFDL's CM2 Global Coupled Climate Models. Part I: Formulation and Simulation Characteristics, *J. Climate*, *19*, 643–674, doi: http://dx.doi.org/10.1175/JCLI3629.1.

Dong, B.-W., and R. T. Sutton (2002), Adjustment of the coupled ocean-atmosphere system to a sudden change in the thermohaline circulation, *Geophys. Res. Lett., 29*(15), 1728, doi: 10.1029/2002GL015229.

Dong, S., S. Garzoli, M. Baringer, C. Meinen, and G. Goni (2009), Interannual variations in the Atlantic meridional overturning circulation and its relationship with the net northward heat transport in the South Atlantic, *Geophys. Res. Lett., 36*, L20606, doi:10.1029/2009GL039356.

Dong, S., S. Garzoli, M. Baringer (2011), The Role of Interocean Exchanges on Decadal Variations of the Meridional Heat Transport in the South Atlantic, *J. Phys. Oceanogr., 41*, 1498–1511.

Ducet, N., P. Y. Le Traon, and G. Reverdin (2000), Global high-resolution mapping of ocean circulation from TOPEX/Poseidon and ERS-1 and -2, *J. Geophys. Res.*, *105*(C8), 19477–19498, doi:10.1029/2000JC900063.

Eden, C. and J. Willebrand (2001), Mechanism of Interannual to Decadal Variability of the North Atlantic Circulation. *J. Climate, 14*, 2266–2280.

Esselborn, S., and C. Eden (2001), Sea surface height changes in the North Atlantic Ocean related to the North Atlantic Oscillation, *Geophys. Res. Lett., 28*, 3473–3476, doi:10.1029/2001GL012863.

Ferry, N., G. Reverdin, and A. Oschlies (2000), Seasonal sea surface height variability in the North Atlantic Ocean, *J. Geophys. Res., 105*(C3), 6307–6326, doi:10.1029/1999JC900296.

Frierson, D. M. W., Y.-T. Hwang, N. S. Fuckar, R. Seager, S. M. Kang, A. Donohoe, E. A. Maroon, X. Liu, and D. S. Battisti (2013), Contribution of ocean overturning circulation to tropical rainfall peak in the Northern Hemisphere, *Nat. Geosci., 6*, 940-944, doi: 10.1038/ngeo1987.

Gary, S. F., M. S. Lozier, C. W. Böning, and A. Biastoch (2011), Deciphering the pathways for the deep limb of the Meridional Overturning Circulation, *Deep-Sea Res., Part II, 58*, 1781–1797, doi:10.1016/j.dsr2.2010.10.059.

Ghirardelli, J. E., M. M. Rienecker, and D. Adamec (1995), Meridional Ekman Heat Transport: Estimates from Satellite Data, *J. Phys. Oceanogr., 25*, 2741–2755. doi: http://dx.doi.org/10.1175/1520-0485(1995)025<2741:MEHTEF>2.0.CO;2

Gill, A. E., and P. P. Niller (1973), The theory of the seasonal variability in the ocean, *Deep Sea Res., 20,* 141–177.

Goldenberg, S. B., C. W. Landsea, A. M. Mestas-Nun˜ez, and W. M. Gray (2001), The recent increase in Atlantic hurricane activity: Causes and implications, *Science, 293*, 474–479.

Gray, A. R., and S. C. Riser (2014), A Global Analysis of Sverdrup Balance Using Absolute Geostrophic Velocities from Argo, *J. Phys. Oceanogr., 44*, 1213–1229. doi: http://dx.doi.org/10.1175/JPO-D-12-0206.1.

Haines, K., K. L. Hermanson, C. L. Liu, D. Putt, R. T. Sutton, A. Iwi and D. Smith (2009), Decadal climate prediction (project GCEP), *Philosophical Transactions of the Royal Society*

A: Mathematical, Physical and Engineering Sciences, 367, 925-937, doi: 10.1098/rsta.2008.0178.

Häkkinen, S. (2001), Variability in sea surface height: A qualitative measure for the meridional overturning in the North Atlantic, *J. Geophys. Res.*, *106*, 13837–13848.

Häkkinen, S., and P. B. Rhines (2004), *Decline of Subpolar North Atlantic Circulation* During the 1990s, *Science, 304,* 555–559.

Häkkinen, S., and P. B. Rhines (2009), Shifting surface currents in the northern North Atlantic Ocean, *J. Geophys. Res., 114,* C04005, doi:10.1029/2008JC004883.

Hall, M. M., and H. L. Bryden (1982), Direct estimates and mechanisms of ocean heat transport, *Deep-Sea Res., 29*, 339-359.

Hartmann, D. L. (1994), The ocean general circulation and climate. *Global Physical Climatology*, Academic Press, International Geophysics Series, Vol. 56, 171-203.

Hastenrath, S. (1982), On Meridional Heat Transports in the World Ocean, *J. Phys. Oceanogr., 12*, 922–927.

Hautala, S. L., D. H. Roemmich, and W. J. Schmilz Jr. (1994), Is the North Pacific in Sverdrup balance along 24°N?, *J. Geophys. Res., 99*(C8), 16041–16052, doi:10.1029/94JC01084.

Hermanson, L., and R. T. Sutton (2009), Climate predictability in the second year, *Philosophical Transactions of the Royal Society A: Mathematical, Physical and Engineering Sciences*, *367*, 913-916, doi: 10.1098/rsta.2008.0181.

Higuchi, K., J. Huang, and A. Shabbar (1999), A wavelet characterization of the North Atlantic oscillation variation and its relationship to the North Atlantic sea surface temperature, *Int. J. Climatol., 19*, 1119–1129.

Hobbs, W. R., and J. K. Willis (2012), Midlatitude North Atlantic heat transport: A time series based on satellite and drifter data, *J. Geophys. Res., 117*, C01008, doi:10.1029/2011JC007039.

Hodson, D. L. R., J. I. Robson, and R. T. Sutton (2014), An Anatomy of the Cooling of the North Atlantic Ocean in the 1960s and 1970s, *J. Climate, 27*, 8229–8243.

Hsiung, J. (1985), Estimates of Global Oceanic Meridional Heat Transport, *J. Phys. Oceanogr., 15,* 1405–1413.

Hurrell, J. W. (1995), Decadal Trends in the North Atlantic Oscillation Regional Temperatures and Precipitation, *Science 269*, 676–679.

Hurrell, J. W., and H. van Loon (1997), Decadal variations in climate associated with the North Atlantic Oscillation, *Clim. Change, 36*, 301-326.

Ivchenko, V. O., S. Danilov, D. Sidorenko, J. Schröter, M. Wenzel, and D. L. Aleynik (2008), Steric height variability in the Northern Atlantic on seasonal and interannual scales, *J. Geophys. Res., 113*, C11007, doi:10.1029/2008JC004836.

Ivchenko, V. O., D. Sidorenko, S. Danilov, M. Losch, and J. Schröter (2011), Can sea surface height be used to estimate oceanic transport variability? *Geophys. Res. Lett., 38*, L11601, doi:10.1029/2011GL047387.

Jayne, S. R., and J. Marotzke (2001), The dynamics of ocean heat transport variability, *Rev. Geophys., 39*, 385-412.

Johns, W. E., M. O. Baringer, L. M. Beal, S. A. Cunningham, T. Kanzow, H. L. Bryden, J. J.-M. Hirschi, J. Marotzke, C. S. Meinen, B. Shaw, and R. Curry (2011), Continuous, Array-Based Estimates of Atlantic Ocean Heat Transport at 26.5°N, *J. Climate, 24,* 2429–2449.

Johnson, H. L. and D. P. Marshall (2002), A Theory for the Surface Atlantic Response to Thermohaline Variability, *J. Phys. Oceanogr., 32*, 1121–1132, doi: http://dx.doi.org/10.1175/1520-0485(2002)032<1121:ATFTSA>2.0.CO;2.

Kang, S. M., I. M. Held, D. M. W. Frierson, and M. Zhao (2008), The response of the ITCZ to extratropical thermal forcing: Idealized slab-ocean experiments with a GCM, *J. Climate, 21*, 3521–3532.

Kanzow, T., S. A. Cunningham, D. Rayner, J. J.-M. Hirschi, W. E. Johns, M. O. Baringer, H. L. Bryden, L. M. Beal, C. S. Meinen, and J. Marotzke (2007), Observed flow compensation associated with the MOC at 26.5°N in the Atlantic, *Science, 317,* 938–941, doi: 10.1126/science.1141293.

Kanzow, T., J. J.-M. Hirschi, H. L. Bryden, D. Rayner, S. A. Cunningham, M. O. Baringer, C. Meinen, J. Marotzke, W. E. Johns, and L. M. Beal (2008), A prototype system of observing the Atlantic meridional overturning circulation—Scientific basis, measurement and risk mitigation strategies, and first results, *J. Oper. Oceanogr., 1,* 19–28.

Kato, S., N. G. Loeb, F. G. Rose, D. R. Doelling, D. A. Rutan, T. E. Caldwell, L. Yu, and R. A. Weller (2013), Surface irradiances consistent with CERES-derived top-of- atmosphere shortwave and longwave irradiances, *J. Climate, 26* (9), 2719–2740, doi: 10.1175/JCLI-D-12-00436.1.

Kawase, M. (1987), Establishment of Deep Ocean Circulation Driven by Deep-Water Production, *J. Phys. Oceanogr., 17*, 2294–2317. doi: http://dx.doi.org/10.1175/1520-0485(1987)017<2294:EODOCD>2.0.CO;2.

Kelly, K. A., and L. A. Thompson (2002), Scatterometer winds explain damped Rossby waves, *Geophys. Res. Lett.*, *29*(20), 1991, doi:10.1029/2002GL015595.

Kelly, K. A., L. Thompson, and J. Lyman (2014), The Coherence and Impact of Meridional Heat Transport Anomalies in the Atlantic Ocean Inferred from Observations, *J. Climate, 27*, 1469–1487. doi: http://dx.doi.org/10.1175/JCLI-D-12-00131.1

Knight, J. R., C. K. Folland, and A. A. Scaife (2006), Climate impacts of the Atlantic Multidecadal Oscillation, *Geophys. Res. Lett., 33*, L17706, doi:10.1029/2006GL026242.

Knight, J. R., R. J. Allan, C. K. Folland, M. Vellinga, and M. E. Mann (2005), A signature of persistent natural thermohaline circulation cycles in observed climate, *Geophys. Res. Lett., 32*, L20708, doi:10.1029/2005GL024233.

Koblinsky, C. J. (1990), The global distribution of *f*/*H* and the barotropic response of the ocean, *J. Geophys. Res., 95*(C3), 3213–3218, doi:10.1029/JC095iC03p03213.

Kuhlbrodt, T., A. Griesel, M. Montoya, A. Levermann, M. Hofmann, and S. Rahmstorf (2007), On the driving processes of the Atlantic meridional overturning circulation, *Rev. Geophys., 45*, RG2001, doi:10.1029/2004RG000166.

Large, W., and S. Yeager (2009), The global climatology of an interannually varying air-sea flux data set, *Clim. Dynam., 33*, 341-364.

Latif, M., E. Roeckner, M. Botzet, M. Esch, H. Haak, S. Hagemann, J. Jungclaus, S. Legutke, S. Marsland, U. Mikolajewicz, and J. Mitchell (2004), Reconstructing, Monitoring, and Predicting Multidecadal-Scale Changes in the North Atlantic Thermohaline Circulation with Sea Surface Temperature, *J. Climate, 17*, 1605–1614.

Leetmaa, A., P. Niiler, H. Stommel (1977), Does the Sverdrup relation account for the mid-Atlantic circulation?, *J. Mar. Res., 35*, 1–10.

Levitus, S. (1987), Meridional Ekman Heat Fluxes for the World Ocean and Individual Ocean Basins, *J. Phys. Oceanogr., 17*, 1484–1492. doi: http://dx.doi.org/10.1175/1520-0485(1987)017<1484:MEHFFT>2.0.CO;2

Levitus, S., R. Burgett, and T. Boyer (1994), World Ocean Atlas 1994, vol.3, Salinity, NOAA Atlas NESDIS, vol. 3, 111pp., NOAA, Silver Spring, Md.

Li, F., Y.-H. Jo, W. T. Liu, and X.-H. Yan (2012), A dipole pattern of the sea surface height anomaly in the North Atlantic: 1990s–2000s, *Geophys. Res. Lett., 39*, L15604, doi:10.1029/2012GL052556.

Lohmann, K., H. Drange, and M. Bentsen (2009), A possible mechanism for the strong weakening of the North Atlantic subpolar gyre in the mid-1990s, *Geophys. Res. Lett.*, *36*, L15602, doi:10.1029/2009GL039166.

Lorbacher, K., J. Dengg, C. W. Boning, and A. Biastoch (2010), Regional patterns of sea level change related to interannual variability and multidecadal trends in the Atlantic meridional overturning circulation, *J. Climate, 23*, 4243–4254, doi:10.1175/2010JCLI3341.1.

Lumpkin, R. and K. Speer (2007), Global Ocean Meridional Overturning, *J. Phys. Oceanogr., 37* (10), 2550-2562.

Mahajan, S., R. Saravanan, and P. Chang (2011), The Role of the Wind–Evaporation–Sea Surface Temperature (WES) Feedback as a Thermodynamic Pathway for the Equatorward Propagation of High-Latitude Sea Ice–Induced Cold Anomalies, *J. Climate, 24*, 1350–1361.

Mahajan, S., R. Zhang, and T. L. Delworth (2011), Impact of the Atlantic Meridional Overturning Circulation (AMOC) on Arctic Surface Air Temperature and Sea Ice Variability, *J. Climate, 24*, 6573–6581.

Marshall, D. (1995), Influence of Topography on the Large-Scale Ocean Circulation, *J. Phys. Oceanogr., 25*, 1622–1635.

Meyers, G. (1979), On the Annual Rossby Wave in the Tropical North Pacific Ocean, *J. Phys. Oceanogr., 9*, 663–674.

Msadek, R., K. W. Dixon, T. L. Delworth, and W. Hurlin (2010), Assessing the predictability of the Atlantic meridional overturning circulation and associated fingerprints, *Geophys. Res. Lett., 37*, L19608, doi:10.1029/2010GL044517.

Msadek, R., W. E. Johns, S. G. Yeager, G. Danabasoglu, T. L. Delworth, and A. Rosati (2013), The Atlantic Meridional Heat Transport at 26.5°N and Its Relationship with the MOC in the RAPID Array and the GFDL and NCAR Coupled Models, *J. Climate, 26*, 4335–4356. doi: http://dx.doi.org/10.1175/JCLI-D-12-00081.1

Msadek, R., T. L. Delworth, A. Rosati, W. Anderson, G. Vecchi, Y.-S. Chang, K. Dixon, R. G. Gudgel, W. Stern, A. Wittenberg, X. Yang, F. Zeng, R. Zhang, and S. Zhang (2014), Predicting a Decadal Shift in North Atlantic Climate Variability Using the GFDL Forecast System, *J. Climate, 27*, 6472–6496.

Nobre, P., and J. Shukla (1996), Variations of sea surface temperature, wind stress and rainfall over the tropical Atlantic and South America, *J. Clim., 9,* 2464 – 2479.

Omrani, N. E., N. S. Keenlyside, J. Bader, and E. Manzini (2014), Stratosphere key for wintertime atmospheric response to warm Atlantic decadal conditions, *Clim. Dynam., 42*(3-4), 649–663, doi:10.1007/s00382-013-1860-3.

Perez, R. C., S. L. Garzoli, C. S. Meinen, and R. P. Matano (2011), Geostrophic Velocity Measurement Techniques for the Meridional Overturning Circulation and Meridional Heat

Transport in the South Atlantic, *J. Atmos. Oceanic Technol., 28*, 1504–1521. doi: http://dx.doi.org/10.1175/JTECH-D-11-00058.1

Persechino, A., J. Mignot, D. Swingedouw, S. Labetoulle, E. Guilyardi (2013), Decadal predictability of the Atlantic meridional overturning circulation and climate in the IPSL-CM5A-LR model, *Clim. Dyn., 40*, 9-10, 2359-2380, doi: 10.1007/s00382-012-1466-1.

Qiu, B. (2002), Large-Scale Variability in the Midlatitude Subtropical and Subpolar North Pacific Ocean: Observations and Causes, *J. Phys. Oceanogr., 32*, 353–375.

Rahmstorf, S. (2002), Ocean circulation and climate during the past 120,000 years, *Nature, 419*, 207-214.

Rhines, P. B., and W. R. Young (1982), A theory for the wind-driven circulation. I. Mid-ocean gyres, *J. Mar. Res.*, *40* (Supplement), 559-596.

Richter, I, S. Xie, S. K. Behera, T. Doi, Y. Masumoto (2013), Equatorial Atlantic variability and its relation to mean state biases in CMIP5, *Clim Dyn, 42*, 171–188

Rind, D., and M. Chandler (1991), Increased ocean heat transports and warmer climate, *J. Geophys. Res., 96*, 7437-7461.

Robson, J., R. Sutton, and D. Smith (2012), Initialized decadal predictions of the rapid warming of the North Atlantic Ocean in the mid 1990s, *Geophys. Res. Lett., 39*, L19713, doi:10.1029/2012GL053370.

Robson, J., R. Sutton, D. Smith (2014), Decadal predictions of the cooling and freshening of the North Atlantic in the 1960s and the role of ocean circulation, *Clim. Dynam., 42*(9-10), 2353-2365.

Roemmich, D. (1983), The Balance of Geostrophic and Ekman Transports in the Tropical Atlantic Ocean, *J. Phys. Oceanogr., 13*, 1534–1539. doi: http://dx.doi.org/10.1175/1520-0485(1983)013<1534:TBOGAE>2.0.CO;2

Schmitz, W. J., J. D. Thompson, and J. R. Luyten (1992), The Sverdrup circulation for the Atlantic along 24°N, *J. Geophys. Res., 97*(C5), 7251–7256, doi:10.1029/92JC00417.

Schneider, N., A. J. Miller, and D. W. Pierce (2002), Anatomy of North Pacific Decadal Variability, *J. Climate*, *15*, 586–605. doi: http://dx.doi.org/10.1175/1520-0442(2002)015<0586:AONPDV>2.0.CO;2

Schott, F. A., J. P. Mccreary, and G. C. Johnson (2004), Shallow Overturning Circulations of the Tropical-Subtropical Oceans, in *Earth Climate: The Ocean-Atmosphere Interaction* (eds C. Wang, S.P. Xie and J.A. Carton), American Geophysical Union, Washington, D. C.. doi: 10.1029/147GM15

Seager, R., Y. Kushnir, P. Chang, N. Naik, J. Miller, W. Hazeleger (2001), Looking for the role of the ocean in tropical Atlantic decadal climate variability, *J. Clim., 14*, 638–655.

Smethie, W. M. (1993), Tracing the spreading of North Atlantic Deep Water in the western North Atlantic deep western boundary current using chlorofluorocarbons F-11 and F-12, *Prog. Oceanogr., 31*, 51-99.

Smith, W. H. F., and D. T. Sandwell (1997), Global seafloor topography from satellite altimetry and ship depth soundings, *Science, 277,* 1956–1962.

Sutton, R. T. and D. L. R. Hodson (2005), Atlantic Ocean forcing of North American and European summer climate, *Science, 309* (5731), 115-118.

Sverdrup, H. U. (1947), Wind-driven currents in a baroclinic ocean with application to the equatorial currents of the eastern pacific, *Proc. Natl. Acad. Sci.*, *USA, 33*, 318-326.

Talley, L. D. (2003), Shallow, Intermediate, and Deep Overturning Components of the Global Heat Budget, *J. Phys. Oceanogr., 33,* 530–560.

Talley, L. D., G. L. Pickard, W. J. Emery, and J. H. Swift (2011), *Descriptive Physical Oceanography: An Introduction*. 6th ed., Academic Press, 560 pp.

Taylor, K. E. (2001), Summarizing multiple aspects of model performance in a single diagram, *J. Geophys. Res., 106*, 7183-7192.

Taylor, K. E., R. J. Stouffer, and G. A. Meehl (2012), An Overview of CMIP5 and the Experiment Design, *Bull. Amer. Meteor. Soc., 93*, 485–498. doi: http://dx.doi.org/10.1175/BAMS-D-11-00094.1

Ting, M., Y. Kushnir, R. Seager, C. Li (2009), Forced and Internal 20th Century SST Trends in the North Atlantic, *J. Climate, 22*, 1469–1481, doi: http://dx.doi.org/10.1175/2008JCLI2561.1

Trenberth, K. E. and A. Solomon (1994), The global heat balance: Heat transports in the atmosphere and ocean, *Climate Dyn., 10*, 107–134.

Trenberth, K. E. and J. M. Caron (2001), Estimates of meridional atmosphere and ocean heat transport, *J. Climate, 14,* 3433-3443

Tulloch, R., and J. Marshall (2012), Exploring Mechanisms of Variability and Predictability of Atlantic Meridional Overturning Circulation in Two Coupled Climate Models, *J. Climate, 25*, 4067–4080, doi: http://dx.doi.org/10.1175/JCLI-D-11-00460.1.

van Sebille, E., M. O. Baringer, W. E. Johns, C. S. Meinen, L. M. Beal, M. F. de Jong, and H. M. van Aken (2011), Propagation pathways of classical Labrador Sea water from its source region to 26°N, *J. Geophys. Res. Oceans, 116*, C12027, doi:10.1029/2011JC007171.

Vivier, F., K. A. Kelly, and L. Thompson (1999), Contributions of wind forcing, waves, and surface heating to sea surface height observations in the Pacific Ocean, *J. Geophys. Res.*, *104*(C9), 20767–20788, doi:10.1029/1999JC900096.

Wang, C. and L. Zhang (2013), Multidecadal Ocean Temperature and Salinity Variability in the Tropical North Atlantic: Linking with the AMO, AMOC, and Subtropical Cell, *J. Climate, 26*, 6137–6162, doi: http://dx.doi.org/10.1175/JCLI-D-12-00721.1.

Wang, C., S. Dong, A. T. Evan, G. R. Foltz, and S.-K. Lee (2012) Multidecadal covariability of North Atlantic sea surface temperature, African dust, Sahel rainfall and Atlantic hurricanes, *J. Climate, 25*, 5404-5415.

Wang, H., S. Legg, and R. W. Hallberg (2015), Representations of the Nordic Seas overflows and their large scale climate impact in coupled models. *Ocean Modelling, 86*, DOI:10.1016/j.ocemod.2014.12.005.

Wang, Z., Y. Lu, F. Dupont, J. W. Loder, C. Hannah, and D. G. Wright (2015), Variability of sea surface height and circulation in the North Atlantic: Forcing mechanisms and linkages, *Prog. Oceanogr., 132*, 273-286, doi:10.1016/ j.pocean.2013.11.004.

Wen, C., P. Chang, and R. Saravanan (2011), Effect of Atlantic Meridional Overturning Circulation on Tropical Atlantic Variability: A Regional Coupled Model Study, *J. Clim., 24*, 3323–3343. doi: http://dx.doi.org/10.1175/2011JCLI3845.1

Willebrand, J., S. G. H. Philander, R. C. Pacanowsky (1980), The oceanic response to large-scale atmospheric disturbances, *J. Phys. Oceanogr., 10*, 411-429.

Willis, J. K. (2010), Can in situ floats and satellite altimeters detect long-term changes in Atlantic Ocean overturning? *Geophys. Res. Lett., 37*, L06602, doi:10.1029/2010GL042372.

Willis, J. K., D. Roemmich, and B. Cornuelle (2004), Interannual variability in upper ocean heat content, temperature, and thermosteric expansion on global scales, *J. Geophys. Res.*, *109*, C12036, doi:10.1029/2003JC002260.

Willis, J. K., and L.-L. Fu (2008), Combining altimeter and subsurface float data to estimate the time-averaged circulation in the upper ocean, *J. Geophys. Res., 113,* C12017, doi:10.1029/2007JC004690

Wunsch, C. (2005), The Total Meridional Heat Flux and Its Oceanic and Atmospheric Partition, *J. Climate, 18*, 4374–4380. doi: http://dx.doi.org/10.1175/JCLI3539.1

Wunsch, C., and D. Roemmich (1985), Is the North Atlantic in Sverdrup Balance? *J. Phys. Oceanogr., 15,* 1876–1880.

Xie, S.-P., and S. Philander (1994), A coupled ocean-atmosphere model of relevance to the ITCZ in the eastern Pacific, *Tellus, 46*A, 340–350.

Yang, X., A. Rosati, S. Zhang, T. L. Delworth, R. G. Gudgel, R. Zhang, G. Vecchi, W. Anderson, Y. Chang, T. DelSole, K. Dixon, R. Msadek, W. F. Stern, A. Wittenberg, and F. Zeng (2013), A Predictable AMO-Like Pattern in the GFDL Fully Coupled Ensemble Initialization and Decadal Forecasting System, *J. Climate, 26*, 650–661, doi: http://dx.doi.org/10.1175/JCLI-D-12-00231.1.

Yeager, S., A. Karspeck, G. Danabasoglu, J. Tribbia, and H. Teng (2012), A Decadal Prediction Case Study: Late Twentieth-Century North Atlantic Ocean Heat Content, *J. Climate, 25,* 5173–5189, doi: http://dx.doi.org/10.1175/JCLI-D-11-00595.1.

Yu, L., X. Jin, and R. A. Weller (2008), Multidecade Global Flux Datasets from the Objectively Analyzed Air-sea Fluxes (OAFlux) Project: Latent and sensible heat fluxes, ocean

evaporation, and related surface meteorological variables, *Rep. OA-2008-1*, 64pp., Woods Hole Oceanogr. Inst., Woods Hole, Mass.

Yukimoto, S., Y. Adachi, M. Hosaka, T. Sakami, H. Yoshimura, M. Hirabara, T. Y. Tanaka, E. Shindo, H. Tsujino, M. Deushi, R. Mizuta, S. Yabu, A. Obata, H. Nakano, T. Koshiro, T. Ose, and A. Kitoh (2012), A new global climate model of the Meteorological Research Institute: MRI-CGCM3-model description and basic performance, J. Meteorol. Soc. Jpn., 90A, 23–64

Zhai, X and C. Wunsch (2013), On the Variability of Wind Power Input to the Oceans with a Focus on the Subpolar North Atlantic. *J. Climate, 26*, 3892–3903. doi: http://dx.doi.org/10.1175/JCLI-D-12-00472.1.

Zhang, D., M. J. McPhaden, W. E. Johns (2003), Observational evidence for flow between the Subtropical and Tropical Atlantic: the Atlantic Subtropical Cells, *J. Phys. Oceanogr., 33*, 1783–1797.

Zhang, H., and L. Wu (2010), Predicting North Atlantic sea surface temperature variability on the basis of the first-mode baroclinic Rossby wave model, *J. Geophys. Res., 115*, C09030, doi:10.1029/2009JC006017.

Zhang, J. and R. Zhang, On the Evolution of Atlantic Meridional Overturning Circulation (AMOC) Fingerprint and Implications for Decadal Predictability in the North Atlantic, *resubmitted to Geophys. Res. Lett.*

Zhang, L., and C. Wang (2013), Multidecadal North Atlantic sea surface temperature and Atlantic meridional overturning circulation variability in CMIP5 historical simulations, *J. Geophys. Res. Oceans, 118*, 5772–5791, doi:10.1002/jgrc.20390.

Zhang, R. (2007), Anticorrelated multidecadal variations between surface and subsurface tropical North Atlantic, *Geophys. Res. Lett., 34*, L12713, doi:10.1029/2007GL030225.

Zhang, R. (2008), Coherent surface-subsurface fingerprint of the Atlantic meridional overturning circulation, *Geophys. Res. Lett., 35*, L20705, doi:10.1029/2008GL035463.

Zhang, R. (2010), Latitudinal dependence of Atlantic meridional overturning circulation (AMOC) variations, Geophys. Res. Lett*., 37*, L16703, doi:10.1029/2010GL044474.

Zhang, R., and T. L. Delworth (2005), Simulated Tropical Response to a Substantial Weakening of the Atlantic Thermohaline Circulation. *J. Climate, 18*, 1853–1860, doi: http://dx.doi.org/10.1175/JCLI3460.1.

Zhang, R., and T. L. Delworth (2006), Impact of Atlantic multidecadal oscillations on India/Sahel rainfall and Atlantic hurricanes, *Geophys. Res. Lett., 33*, L17712, doi:10.1029/2006GL026267.

Zhang, R., S. M. Kang, and I. M. Held (2010), Sensitivity of Climate Change Induced by the Weakening of the Atlantic Meridional Overturning Circulation to Cloud Feedback, *J. Climate, 23,* 378–389, doi: http://dx.doi.org/10.1175/2009JCLI3118.1.

Zhang, R., T. L. Delworth, A. Rosati, W. G. Anderson, K. W. Dixon, H. Lee, and F. Zeng (2011), Sensitivity of the North Atlantic Ocean circulation to an abrupt change in the Nordic Sea overflow in a high resolution global coupled climate model, *J. Geophys. Res. Oceans*, *116*, C12024, DOI:10.1029/2011JC007240.

Zhang, T., P. W. Stackhouse Jr, S.K. Gupta, S. J. Cox, J. C. Mikovitz (2015), The Validation of the GEWEX SRB surface longwave flux data products using BSRN measurements, *J. Quant. Spectrosc. Radiat. Transf., 150,* 134–147.

Zheng, Y. and B. Giese (2009), Ocean heat transport in Simple Ocean Data Assimilation: Structure and mechanisms, *J. Geophys. Res. Oceans, 114,* C11009. doi:10.1029/2008JC005190

VITA

Jinting Zhang is a Ph.D. candidate in School of Oceanography at University of Washington. She graduated with Bachelor of Science from Ocean University of China and came to University of Washington pursuing the Ph.D. degree in physical oceanography, under the supervision of Professor LuAnne Thompson and Professor Kathryn A. Kelly. Jinting Zhang also has a Master degree in Applied Mathematic at University of Washington.